NMR Studies of MRI Contrast Agents and Cementitous Materials

by

Zihui Peng

A Dissertation Presented in Partial Fulfillment
of the Requirements for the Degree
Doctor of Philosophy

Approved November 2013 by the
Graduate Supervisory Committee:

Robert Marzke, Chair
Sandwip Dey
Narayanan Neithalath
Ralph Chamberlin
Martha McCartney

ARIZONA STATE UNIVERSITY

December 2013

ABSTRACT

Nuclear magnetic resonance (NMR) is an important phenomenon involving nuclear magnetic moments in magnetic field, which can provide much information about a wide range of materials, including their chemical composition, chemical environments and nuclear spin interactions. The NMR spectrometer has been extensively developed and used in many areas of research. In this thesis, studies in two different areas using NMR are presented. First, a new kind of nanoparticle, Gd(DTPA) intercalated layered double hydroxide (LDH), has been successfully synthesized in the laboratory of Prof. Dey in SEMTE at ASU. In Chapter II, the NMR relaxation studies of two types of LDH (Mg, Al-LDH and Zn, Al-LDH) are presented and the results show that when they are intercalated with Gd(DTPA) they have a higher relaxivity than current commercial magnetic resonance imaging (MRI) contrast agents, such as DTPA in water solution. So this material may be useful as an MRI contrast agent. Several conditions were examined, such as nanoparticle size, pH and intercalation percentage, to determine the optimal relaxivity of this nanoparticle. Further NMR studies and simulations were conducted to provide an explanation for the high relaxivity. Second, fly ash is a kind of cementitious material, which has been of great interest because, when activated by an alkaline solution, it exhibits the capability for replacing ordinary Portland cement as a concrete binder. However, the reaction of activated fly ash is not fully understood. In chapter III, pore structure and NMR studies of activated fly ash using different activators, including NaOH and KOH (4M and 8M) and Na/K silicate, are presented. The pore structure, degree of order and proportion of different components in the reaction product were obtained, which reveal much about the reaction and makeup of the final product.

DEDICATION

To my parents and wife

ACKNOWLEDGMENTS

I would like to first thank my supervisors, Dr. Robert F. Marzke for his guidance and patience during my Ph.D. study at ASU. The research in this thesis could not be done without his invaluable knowledge and encouragement.

I would like also to thank the assistance from all the faculty members who have served as my committee: Dr. Sandwip K. Dey, Dr. Neithalath Narayanan, Dr. Ralph V. Chamberlin and Dr. Martha R. McCartney.

Thanks to Naoki Ito and Mohammed Abdullah who taught me about NMR and the spectrometer the first day I joined this group. I have been lucky to cooperate with several outstanding graduate students: Xiaodi Sun, Aishwarya Ramachandran, Kirk Vance and Akash Dakhane, who made significant contributions to studies related to this thesis.

Finally, I would like to thank all the staff working for Physics Department, who have always been supportive, and who make the experience of study great at the Physics Department of ASU.

TABLE OF CONTENTS

CHAPTER

CHAPTER PAGE

LIST OF TABLES

LIST OF FIGURES

Figure Page

CHAPTER 1

INTRODUCTION

1.1 Nuclear Magnetic Resonance (NMR)

Nuclear Magnetic Resonance (NMR) was first observed in molecular beams by Isidor Rabi(1938) in 1938. In 1946, Purcell's group and Bloch's group separately observed NMR in solid(PURCELL, TORREY, and POUND 1946) and liquid samples(BLOCH, HANSEN, and PACKARD; BLOCH 1946). In 1952, Bloch and Purcell were awarded the Nobel Prize in physics for the work on NMR. In a very short time, NMR became an important technique in many fields such as chemistry, biology and so on. Two Nobel Prizes in Chemistry were separately awarded to Richard Ernst in 1991 for his contributions to the further development of NMR spectroscopy, and to Kurt Wüthrich in 2002 for his application of NMR to biological research. The important visualization technique magnetic resonance imaging (MRI) was also developed based on NMR, around 1971. Paul C. Lauterbur(1973, 1974)and Peter Mansfield(1977; Mansfield and Pykett 1978) were awarded the Nobel Prize in Physiology or Medicine in 2003 for their contribution to MRI.

1.1.1 Classic Description of NMR

We consider a single nucleus in an ambient magnetic field(Abragam 1961; Goldman 1990; Slichter 1989; Stejskal and Memory 1994):

$$\boldsymbol{H}_0 = H_0\boldsymbol{k}. \tag{1.1}$$

Assume the magnetic moment of nucleus is given by(Pake 1950, 1950)

$$\boldsymbol{\mu} = \gamma \boldsymbol{I}. \tag{1.2}$$

γ is constant; $\boldsymbol{I}$ is the nuclear spin (intrinsic angular momentum).

If the moment is not aligned with the ambient field $\boldsymbol{H}_0$, the nucleus would experience a torque

$$\boldsymbol{\tau} = \boldsymbol{\mu} \times \boldsymbol{H}_0. \tag{1.3}$$

The torque exerted by $\boldsymbol{H}_0$ *on* $\boldsymbol{I}$ is equal to the time derivative of the angular momentum:

$$\boldsymbol{\tau} = \frac{\mathrm{d}\boldsymbol{I}}{\mathrm{dt}} \tag{1.4}$$

So we have

$$\frac{\mathrm{d}\boldsymbol{I}}{\mathrm{dt}} = \boldsymbol{\mu} \times \boldsymbol{H}_0 \tag{1.5}$$

Therefore

$$\frac{\mathrm{d}\boldsymbol{\mu}}{\mathrm{dt}} = \gamma \boldsymbol{\mu} \times \boldsymbol{H}_0. \tag{1.6}$$

The solution of this equation is

$$\mu_x(t) = \mu_x(0)\cos\omega t + \mu_y(0)\sin\omega t \tag{1.7}$$

$$\mu_y(t) = \mu_y(0)\cos\omega t - \mu_x(0)\sin\omega t \tag{1.8}$$

$$\mu_z(t) = constant \tag{1.9}$$

The equation of motion represents nuclear moment precession around the ambient magnetic field with frequency

$$\omega_0 = -\gamma H_0. \tag{1.10}$$

This frequency is called the Larmor frequency and denoted as ω_0. The ratio of moment to momentum γ is called gyromagnetic ratio. The rotating magnetic moment in the x-y plane is observable and produces the nuclear magnetic resonance (NMR) signal.

The thermal equilibrium state of the magnetic moment in the magnetic field is aligned with the ambient field by basic statistical mechanics. To observe NMR, we need apply a small magnetic field oscillating along x axis

$$\boldsymbol{H}_1 = 2H_1\boldsymbol{i}\bullet\cos\omega t \tag{1.11}$$

This oscillating magnetic field can be considered as two counter-rotating components with opposite frequency.

$$\boldsymbol{H}_1 = H_1(\boldsymbol{i}\bullet\cos\omega t + \boldsymbol{j}\bullet\sin\omega t) + H_1(\boldsymbol{i}\bullet\cos\omega t - \boldsymbol{j}\bullet\sin\omega t) \tag{1.11}$$

Choose the rotating frame with frequency $\boldsymbol{\omega}_0$:

$$\left(\frac{d\boldsymbol{\mu}}{dt}\right)_{rot} = \left(\frac{d\boldsymbol{\mu}}{dt}\right)_{lab} + \boldsymbol{\mu}\times\boldsymbol{\omega} = \gamma\boldsymbol{\mu}\times(\boldsymbol{H}_0 + \boldsymbol{H}_1)_{rot} + \boldsymbol{\mu}\times\boldsymbol{\omega}_0 \tag{1.12}$$

Since $\omega_0 = -\gamma H_0$. We have

$$\left(\frac{d\boldsymbol{\mu}}{dt}\right)_{rot} = \gamma\boldsymbol{\mu}\times(\boldsymbol{H}_1)_{rot} - \boldsymbol{\mu}\times\boldsymbol{\omega}_0 + \boldsymbol{\mu}\times\boldsymbol{\omega}_0 = \gamma\boldsymbol{\mu}\times(\boldsymbol{H}_1)_{rot} \tag{1.13}$$

The rotation matrix is

$$R = \left\{\begin{matrix} \cos\omega_0 t & -\sin\omega_0 t & 0 \\ \sin\omega_0 t & \cos\omega_0 t & 0 \\ 0 & 0 & 1 \end{matrix}\right\} \tag{1.14}$$

The applied field $\boldsymbol{H}_1$ become

$$(\boldsymbol{H}_1)_{rot} = R(\boldsymbol{H}_1)_{lab} = 2H_1(\boldsymbol{i}\bullet\cos\omega_0 t\bullet\cos\omega t + \boldsymbol{j}\bullet\sin\omega_0 t\bullet\cos\omega t) \tag{1.15}$$

This is the effective field exerted on magnetic moment in the rotating frame.

If we choose an applied r.f. pulse with the Larmor frequency ω_0, we will have

$$(\boldsymbol{H}_1)_{rot} = H_1\boldsymbol{i} + H_1(\boldsymbol{i}\cdot\cos 2\omega t + \boldsymbol{j}\cdot\sin 2\omega t) \tag{1.16}$$

The first term is constant in the rotating frame and has the effect of rotating the magnetic moment around the x axis with frequency

$$\omega_1 = -\gamma H_1 \tag{1.17}$$

The second term rotates around z axis with frequency 2ω and its general effect on magnetic moment can be shown to be very small.

The flip angle depends on how long the field $\boldsymbol{H}_1$ is applied. The commonly used flip angles are 90° and 180°. The applied field is called radio frequency field (r.f field)

1.1.2 Bloch Equation

If there is energy exchange between the nuclei and the environment, such as a lattice or detection coil, the nuclei tend to move toward a thermal equilibrium state, in which the magnetic moments align with the ambient magnetic field. Felix Bloch assumed the motion of nuclear toward equilibrium was exponential, with two time constants: T_1 for the longitudinal component and T_2 for the transverse components; he then obtained the Bloch equations(BLOCH 1946):

$$\frac{d\boldsymbol{\mu}}{dt} = \gamma\boldsymbol{\mu} \times \boldsymbol{H} - \frac{1}{T_1}(\mu_z - \mu_0)\boldsymbol{k} - \frac{1}{T_2}(\mu_x\boldsymbol{i} + \mu_y\boldsymbol{j}) \tag{1.18}$$

In the rotating frame with frequency $-\gamma H_0$, the Bloch equations become:

$$\frac{d\mu_z}{dt} = -\frac{1}{T_1}(\mu_z - \mu_0) \qquad (1.19)$$

$$\frac{d\mu_{xy}}{dt} = -\frac{1}{T_2}\mu_{x,y} \qquad (1.20)$$

1.1.3 Quantum Description of NMR

Assume a nucleus with spin ½ in an ambient magnetic field

$$\boldsymbol{H} = H_0\boldsymbol{k}. \qquad (1.21)$$

The nuclear spin Hamiltonian is

$$\mathbf{H} = -\boldsymbol{\mu}\bullet\boldsymbol{H} = -\gamma I_z H_0 \qquad (1.22)$$

The two split energy levels are $E_{-1/2}$= $1/2\hbar\gamma H_0$(spin down) and $E_{1/2}$= $-1/2\hbar\gamma H_0$(spin up). When the state of the nuclear spin changes between two energy levels, there is emission or absorption of radiation with energy of magnitude

$$\Delta E = \hbar\gamma H_0. \qquad (1.23)$$

From eq. 1.10 the angular frequency is

$$\omega = -\gamma H_0. \qquad (1.24)$$

The negative sign in frequency means that only radiation of the proper circular polarization can be absorbed or emitted.

For an assembly of a large number (n) of identical spins, the energy distribution of states follows the Boltzmann distribution.

$$P_n \propto \exp(-E_n / k_B T) \qquad (1.25)$$

P_n is the possibility of finding a spin in energy level E_n; k is Boltzmann constant; T is theabsolute temperature.

So the total amounts of spins up and spins down are separately:

$$N_+ \propto e^{x} \tag{1.26}$$

$$N_- \propto e^{-x} \tag{1.27}$$

Where $x = \frac{1}{2}\frac{\hbar\gamma H_0}{kT}$;

With the condition $N_+ + N_- = n$, we will have:

$$N_+ = \frac{ne^{x}}{e^{x} + e^{-x}} \tag{1.28}$$

In the high temperature limit ($x \ll 1$), which is always valid in NMR.

$$N_+ \approx \frac{n(1+x)}{2} \tag{1.29}$$

$$N_- \approx \frac{n(1-x)}{2} \tag{1.30}$$

In the two state system mentioned above, the magnetization ***M*** is equal to difference of total spin up moment and spin down moment.

$$M = \frac{1}{2}\gamma\hbar(N_+ - N_-) = \frac{1}{4}\frac{n\gamma^2\hbar^2 H_0}{kT} \tag{1.31}$$

This is Curie's law with the spin 1/2 spin system at temperature T. In general with nuclear spin I we have:

$$M = \frac{n\gamma^2\hbar^2 I(I+1)H_0}{3k_B T} \tag{1.33}$$

In a quantum statistical ensemble, the average value of an operator is determined by the density matrix(Farrar 1990, 1990, Bloch 1956, Refield 1957). The same result can be obtained with a classical description i.e. the magnetization will precess around ambient field with frequency $-\gamma H_0$.

1.1.4 Free Induction Decay (FID)

After applying an r.f. pulse, there is a component of magnetization **M** in x-y plane precessing around the ambient field. This Larmor precession will lead to an induced emf in a detection coil (in the x-y plane). The spin polarization will dissipate because of both spin-spin relaxation and inhomogeneity of the magnetic field. The decreasing signal is called free induction decay (FID) (Figure 1.1 (a)). The NMR spectrum is the Fourier transform of the FID (Figure 1.1 (b)), and it can provide information about nuclei, such as their Larmor precession frequency and relative numbers of nuclear spins in a sample.

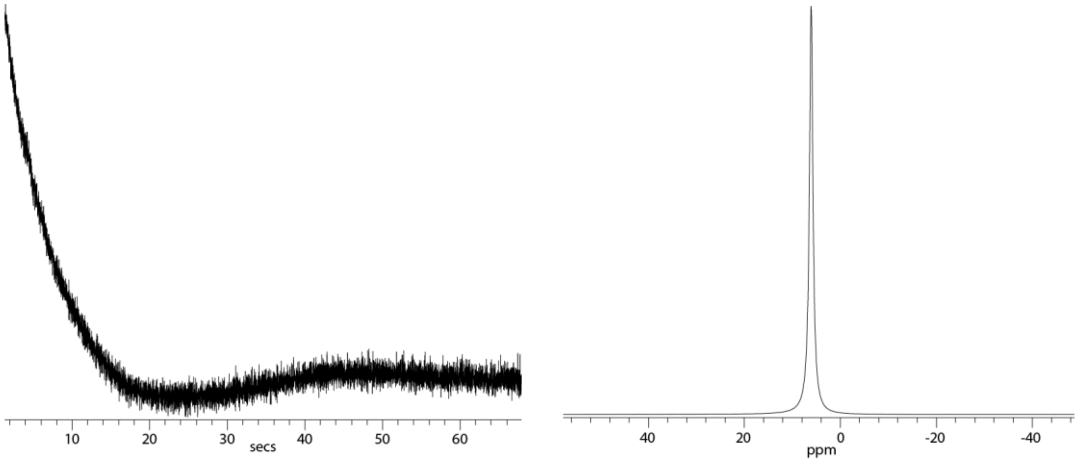

Figure 1.1 (a) On-resonance free Induction Decay (FID) (b) NMR spectrum (Fourier Transform of FID)

1.1.5 Chemical Shift

The actual magnetic field sensed by the nucleus is always different from the applied field because of the magnetic field induced by electrons in the atom (both orbital motion and spin). So the chemical bonding of atom can be identified based on the resonance frequency, because the chemical bonding will affect the electrons' distribution, therefore causing a different change in resonance frequency. For each non-equivalent chemical environment that the nucleus is in, for example, in a given position in the molecule CH_3OH is an example. Three protons in the methyl CH_3 group are equivalent, but the OH proton is not. So CH_3OH gives a two-line spectrum, the CH_3 proton line being three times as intense as the OH line, at positions differing in NMR frequency. The concept of chemical shift is introduced to define the difference between resonance frequency of a nucleus and the frequency of a standard.

$$\delta = \frac{f - f_{ref}}{f_{ref}} \times 10^6 \tag{1.33}$$

For protons this standard is the highly stable molecule TMS (tetramethylsilane).

The chemical shift (δ) is usually expressed in part per million (ppm). An advantage of chemical shift compared with frequency is that chemical shift is the independent of the ambient field.

1.2 Relaxation

The process of nuclear magnetization returning to thermal equilibrium is known as relaxation. The characteristic time of this process is the relaxation time(Bloch 1946, Abragam 1961).

Two types of relaxation times, as mentioned previously, longitudinal relaxation times T_1 and transverse relaxation times T_2, are both important properties of nuclei because they involve the interaction between nuclear spins and the energy exchange between nuclear spins and lattice. A large magnetic field inhomogeneity leas to a fast decay of the FID, but this can be partly avoided by the use of spin echoes. Unavoidable transverse relaxation will still remain, however, owing to spin-spin interactions. All pulse sequences must take account of these fundamental relaxation processes of nuclear spins, as we discuss now.

1.2.1 Longitudinal Relaxation Time

The longitudinal relaxation time (T_1) represents the recovery rate of the magnetization along the z axis. This type of relaxation is attributed to the energy exchange between nuclear spins and lattice, so longitudinal relaxation time is also called spin-lattice relaxation time. The method of inversion recovery (IR) is used to measure longitudinal relaxation time. The IR sequence is usually composed of a 180^o pulse followed by a 90^o pulse, with a variable time interval τ between the two pulses (Figure 1.2 (a)). First, the 180^o inverts the magnetization. During the subsequent time interval the magnetization experiences longitudinal relaxation recovering towards its value prior to the 180^o pulse, but in this

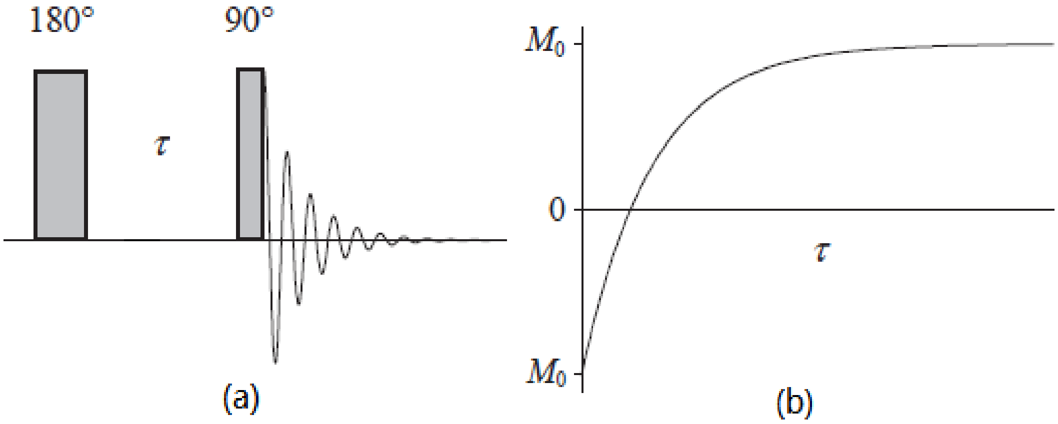

Figure 1.2 (a) Pulse Sequence of Inversion Recovery; (b) the evolution of magnetization with variable time interval τ.

recovery no signal can be detected because there is no magnetization component in the x-y plane. The 90° pulse then rotates magnetization into the x-y plane, which produces an NMR signal. The intensity of signal depends on the time interval between 180° pulse and 90° pulse (Figure 1.2 (b)), according to the equation

$$M(\tau) = M_0[1 - 2\exp(-\tau / T_1)] \tag{1.34}$$

1.2.2 Transverse Relaxation Time

The transverse relaxation time (T_2) in the plane transverse to the large static field $\mathbf{H_0}$ represents the decay rate of the magnetization component in this plane, which gives rise to the observed NMR signal induced. The signal always decays with time, hence its name as free induction decay (FID). The decay time of the FID represented as T_2^* can be attributed in part to magnetic field inhomogeneity. Because of this inhomogeneity of field, the resonance frequencies of nuclei differ with position in a sample, which means that each spin will precess with a slightly different frequency from $\omega_0 = \gamma H_0$. In this case, spins fanning out following a strong (non-selective) 90° pulse, eventually lead to zero magnetization in x-y plane. But transverse spins could still be far away from full relaxation. The transverse relaxation, without the field inhomogeneity effect, is attributed to spin-spin interactions, so this relaxation time is also called the spin-spin relaxation time. To get rid of the inhomogeneity effect, spin echo method is used and it can also measure the homogeneous field transverse relaxation time (T_2)(Hahn 1950).

The spin echo sequence is composed of a 90° pulse and a 180° pulse, the time interval τ between 90° pulse and 180° pulse determining how long to wait after the 180° pulse for the spins to rephase, when the NMR signal can be observed(Figure 1.3(a)). The operation of the spin echo sequence is as follows. First, the 90° pulse rotates the magnetization into the x-y plane (Figure 1.4). Because of inhomogeneity of the field, spins with different precession speeds will fan out. This is called dephasing. Applying a 180° pulse after a time

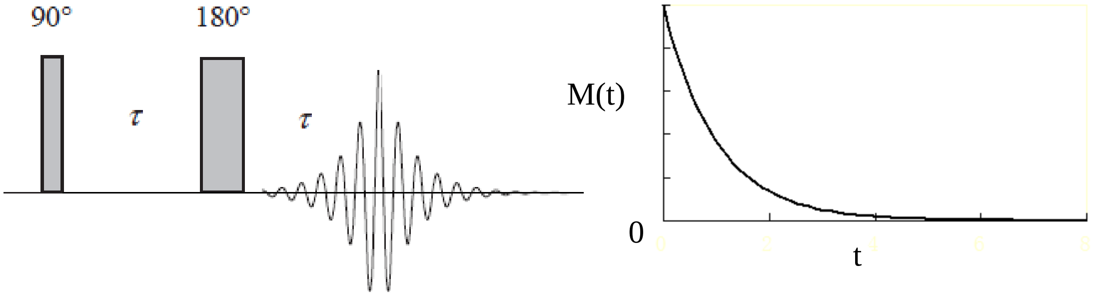

(a)

(b)

Figure 1.3 (a) Pulse sequence of spin echo; (b) the evolution of magnetization of spin echo interval τ causes all the spins to suddenly reverse phase, so the fast spins are then behind the slow spins. After the same time interval τ, the fast spins catch up with the slow spins and a spin "echo" can be detected. The intensity of the spin echo is clearly related to time interval between two pulses (Figure 1.3 (b)) according to the equation:

$$M(\tau) = M_0 \exp(-2\tau / T_2) \tag{1.35}$$

Where M_0 is equilibrium initial magnetization along the large static magnetic field $\mathbf{H_0}$.

By varying the 90^o-180^o delay time τ and observing the intensity of the spin echo signal, the spin-spin relaxation time T_2 can be measured.

The longitudinal relaxation time directly controls how long a 90^o rotated initial magnetization **M** will take to return to it thermal equilibrium value along the field $\mathbf{H_0}$ in

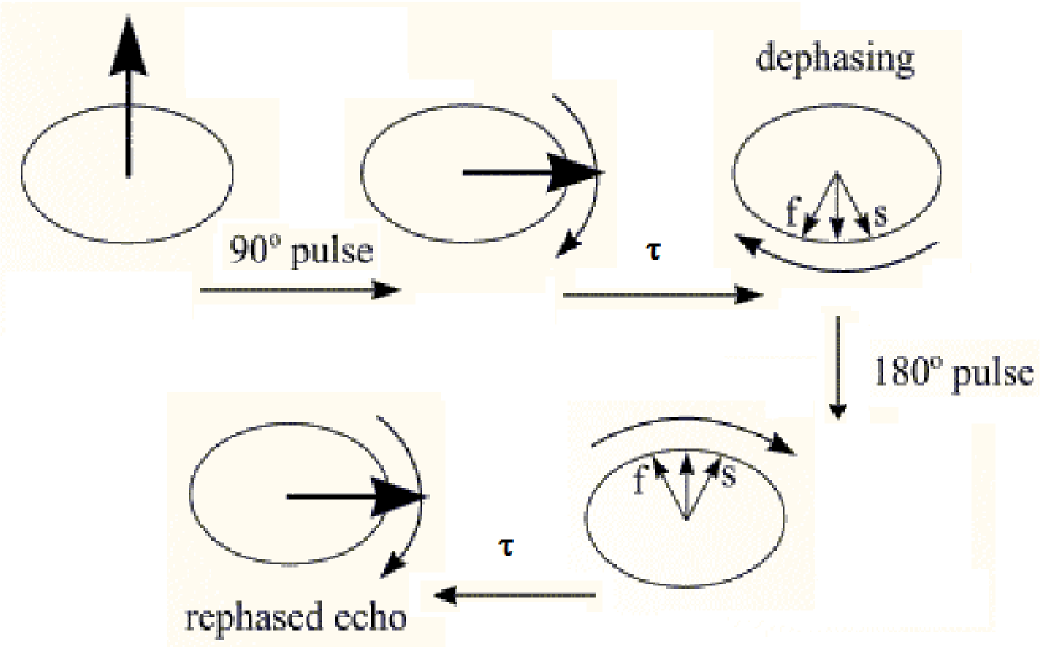

Figure 1.4 Building-up of a spin echo

each NMR measurement. Multiple signal accumulation is used in NMR to get a high signal noise ratio(S/N). The time between each accumulations is called the pulse delay, which depends on the longitudinal relaxation time. The optimal pulse delay for full recovery has been shown to be five times the longitudinal relaxation time. This condition must be met for correct measurements of relaxation time in NMR.

1.2.3 Relaxation Mechanisms

The static ambient field only leads to precession of magnetization, but the fluctuations of field which nuclei experience during and after a pulse sequence affect the relaxation of the

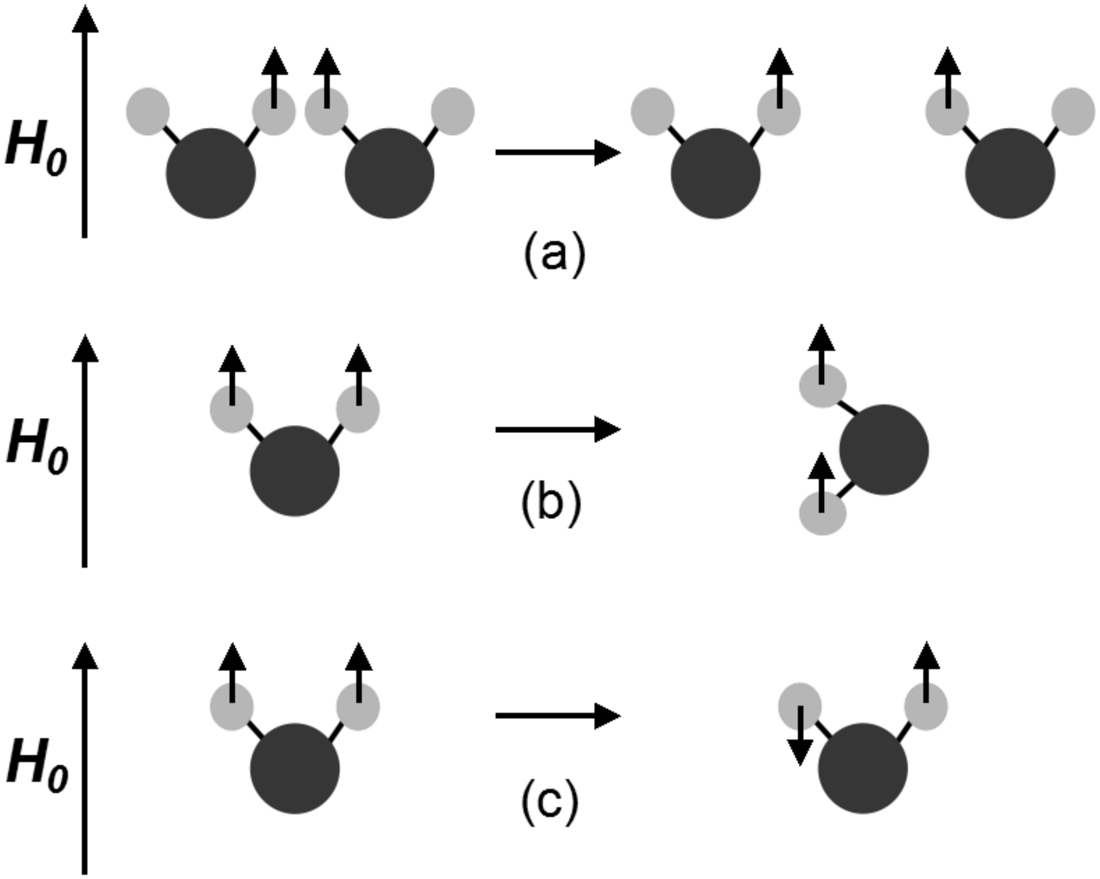

Figure 1.5 dipolar relaxation caused by (a) molecule motion; (b) molecule rotation; (c) dipole flip.

magnetization. There are several spin-spins interactions that give rise to fluctuating magnetic fields which relax spins, such as dipolar interactions and scalar interactions.

Taking dipolar interaction as an example, the local field of a nuclear spin can be influenced by a neighboring dipole. Three situations induce fluctuations of local fields in dipolar interactions. First, the fluctuation of field can arise from molecular translation motion (Figure 1.5 (a)). The rapid changes of distance between dipoles will affect the local magnetic field exerted by another magnetic dipole. This relaxation depends on translation diffusion or chemical exchange. Second, with the molecule rotation, the relative orientation of two dipoles would change (Figure 1.5 (b)), which also causes fluctuation of the lotal magnetic field. Third, if the spin state of one dipole changes (flips) independently of the one under observation, the induced field on the observed dipole also changes (Figure 1.5 (c)). The spin tends to stay at its lowest energy level (aligned in the ambient field), but it is still possible for spin to transition to another state. When the transition happens, the local field would change. This type of relaxation is also known as Curie relaxation. It is important when one of the dipoles is electronic because the rate of spin flips is much higher for the electron than for the nucleus.

To calculate a relaxation time, these microscopic motions must be described, so correlation functions and spectral densities were introduced. Consider a free 1/2 spin system of n spins.

The state of a spin can be characterized by the index m(1/2 or -1/2), which is a stochastic variable. The definition of a correlation function is

$$G(\tau) = \frac{1}{n}\sum_i [m_i(0) \cdot m_i(\tau)] \tag{1.36}$$

Here the $m_i(t)$ represent the state of *i*th particle at time t.

Apparently, correlation function has a maximum at *t=0* and then decreases with time. Assuming it is an exponential decay, the correlation function becomes

$$G(\tau) = \frac{1}{4}\exp(-\frac{\tau}{\tau_c}) \tag{1.37}$$

The characteristic time is correlation time τ_c. So the correlation time characterizes how fast the state of system changes.

Now if the fluctuating local field is $H_1(t)$, its correlation function can be written as:

$$G(\tau) = \overline{H_1(t)H_1(t+\tau)} = \overline{H_1^2} e^{-|\tau|/\tau_0} \tag{1.38}$$

The bar above means average; $\overline{H_1^2}$ is mean square value of fluctuating field.

The spectral density if the Fourier transform of correlation function(Abragam 1961, TC 1987)

$$J(\omega) = \int_{-\infty}^{+\infty} G(\tau) e^{-i\omega\tau} d\tau \tag{1.39}$$

$$= 2\overline{H_1^2} \frac{\tau_0}{1+\omega^2\tau_0^2} \tag{1.40}$$

From the Bloch-Wangsness-Redfield Theory(Bloch 1956; Wangsness and Bloch 1953; Redfield 1957), we have

$$\frac{1}{T_1} = 2\overline{H_1^2}\gamma^2 \frac{\tau_0}{1+\omega_0^2\tau_0^2} \tag{1.41}$$

$$\frac{1}{T_2} = \overline{H_1^2}\gamma^2 (\tau_0 + \frac{\tau_0}{1+\omega_0^2\tau_0^2}) \tag{1.42}$$

These results are obtained with the assumption that fluctuation of the field is isotropic. This assumption is always valid in a liquid, but orientation might need to be considered in a solid.

From these results we can see that T_1 and T_2 are close with a small τ_0 (Figure 1.6), which is the case in a liquid. T_1 has a minimum when $\omega_0\tau_0=1$. With a long τ_0, T_1 increases with τ_0 while T_2 decreases, which is common in solids.

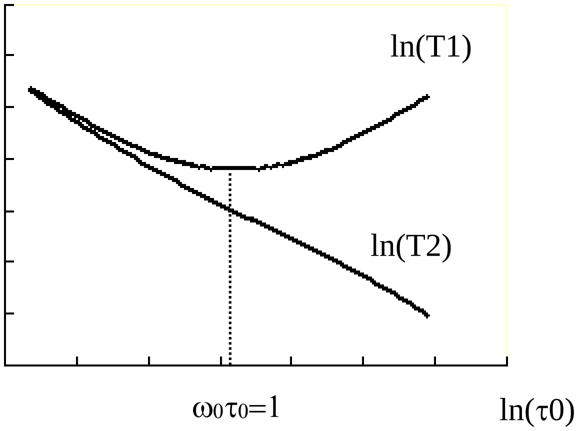

Figure 1.6 Relaxation time variation trend with correlation

1.3 Solid State NMR

NMR spectra provide information about chemical shifts and the relative intensities of different species. Various interactions, as mentioned, will affect the local magnetic field, leading to different resonance frequencies for same species of nuclei(Maciel 1984; Oldfield and Kirkpatrick 1985). These interactions will broaden line width in the NMR spectrum, leading to lower resolution. This won't be a problem in a liquid, because the rapid and isotropic motion of atoms will average out the broadening effects. So the line width of liquid NMR is very small and is only limited by the spin-lattice relaxation time(Lyerla, McIntyre, and Torchia 1974) and the magnetic field inhomogeneity.

However, in solid samples, all these interaction will broaden line widths in a spectra and make it hard to analyze the NMR result. Therefore some methods were used for solid state NMR to get high resolution(Mackenzie and Smith 2002). The commonest method is magic angle spinning (MAS)(Andrew 1971).

1.3.1 Magic Angle Spinning (MAS)

The MAS method consists of spinning the sample rapidly at an angle 54.74^{o} to the axis of the ambient field(Andrew 1981) (Figure 1.7). The MAS can reduce the broadening of line that comes from dipole-dipole interaction, chemical shift anisotropy (CSA) and first order observed in the NMR spectrum (Figure 1.8 asterisk marked line). The spinning sidebands come from the time dependent term in those interactions listed above(Maricq and Waugh

1979). Peaks of the central resonance and each spinning sideband are separated in frequency by the spin rate, but the central line will stay stationary when the spin rate changes. So the central line can be distinguished from a sideband by varying the sample spin rate

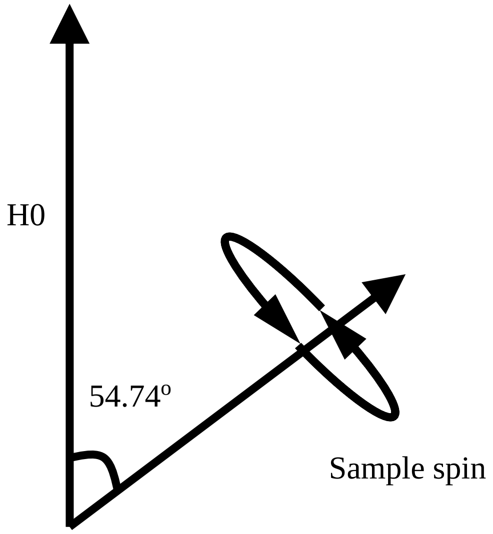

Figure 1.7 Magic Angle Spinning (MAS)

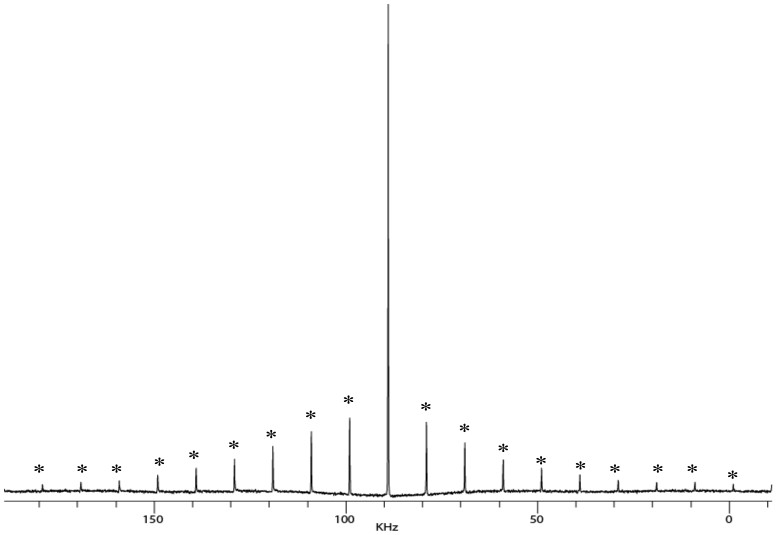

Figure 1.8 MAS NMR spectrum with spin sideband (with asterisk mark);
spin rate 10kHz

1.3.2 Cross-Polarization MAS

Although, MAS can decrease the broadening effect of internuclear dipole-dipole interaction to a great extent, MAS solid state NMR still has a broader central line than the extremely narrow ones observed in liquid NMR, because of inhomogeneities in isotropic chemical shift in solids. Besides, some nuclei have low natural abundance, such as ^{13}C and ^{29}Si, and therefore it is hard to get a spectrum of these nuclei with good signal noise(S/N) ratio. From the equation (1.41), we can also see longitudinal relaxation time is inversely proportional to the gyromagnetic ratio (γ) squared. Many nuclei, such as ^{13}C, have a γ only one fourth of that the proton's, and therefore have a long longitudinal relaxation time in solid state, which in addition to low natural abundance makes it intensively time consuming to improve S/N by multiple accumulation. So another technique is commonly used in solid state NMR, which is cross polarization (CP)(Pines, Gibby, and Waugh 1973). The requirements of CP are that there must be rapidly relaxing magnetization of an

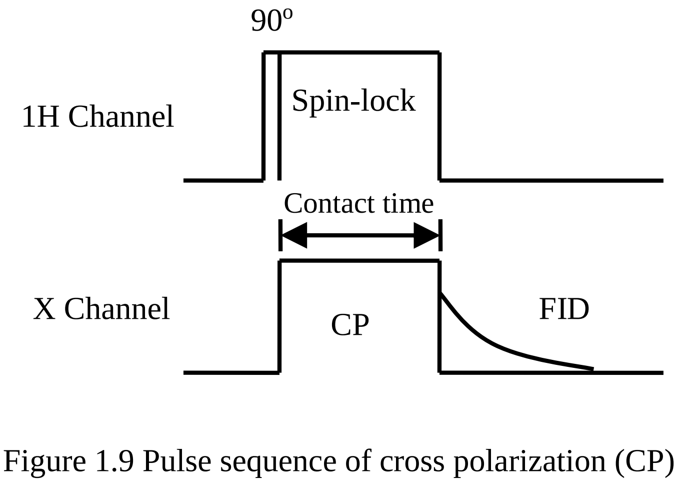

Figure 1.9 Pulse sequence of cross polarization (CP)

abundant nuclear spin species, such as protons in an organic sample and that a coupling usually dipolar, exists between the abundant species (^{1}H) and the targeted element(X), ^{13}C for example. The pulse sequence of CP is shown as in Figure 1.9. In the ^{1}H channel, the magnetization is first rotated into the x-y plane by a 90^o pulse, then the spin is locked by a change of the phase of the applied field(H_1) field by $+90^o$, so H_1 is aligned with the magnetization. In this case, the magnetization would not dephase and would only experience decay with a "rotating frame" relaxation time $T_{1\rho}$. $T_{1\rho}$ usually has approximately the same magnitude as T_1, so the spin lock provides enough time to build up polarization in ^{13}C nuclei. At the same time, with spin lock in the ^{1}H channel, another radio frequency pulse is also applied in the X channel at the resonance frequency of ^{13}C nuclei. The pulse in the X channel allows rapid thermal contact between ^{13}C and ^{1}H for the buildup of ^{13}C polarization. The intensities of applied r.f. field in two channels must obey the follow relation:

$$\gamma_H B_H = \gamma_X B_X \tag{1.43}$$

Where γ_H and γ_X are separately the gyromagnetic ratio of ^{1}H and ^{13}C; $\boldsymbol{B_H}$ and B_X are separately the radio frequency magnetic fields applied to them.

This condition is known as the Hartmann-Hahn condition(Hartmann and Hahn 1962). When this condition is fulfilled, the spin energies of the two species of nuclear are the same， and this makes possible the energy exchange between them. Initially the spins of ^{1}H are locked in the x-y plane and the spins of ^{13}C are disordered. This means that the ^{1}H spins have a low temperature and ^{13}C spins have a high temperature. The spin temperature of coupled H-^{13}C system in the thermal contact is cooled down because of large number of ^{1}H spins. As shown in Figure 1.10, the ^{13}C spin signal intensity increases with contact time at first. This increase of intensity results from ^{13}C spins being cooled down after contact, i.e. polarized along H_1 in its rotating frame, and therefore magnetization of ^{13}C is observed in the x-y plane. After the spins reach the maximum contact, spins of ^{1}H and X have the same spin temperature, and then the intensity decreases with contact time and thereafter, as the spins relax to the small r.f. Magnetic field in the rotating frame. This relaxation is governed by the rotating frame relaxation time $T_{1\rho}$, for the coupled ^{1}H-^{13}C. So using the cross polarization, the magnetization of X in x-y plane can be built up no matter what the original room temperature magnetization of ^{13}C is. That means that ^{13}C spins don't need to be fully relaxed, which will hugely shorten the measurement time. Besides, the polarization

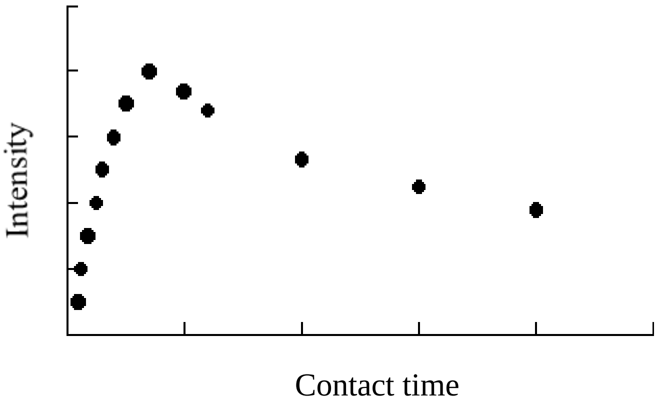

Figure 1.10 A schematic of relation between intensity of CPMAS and contact time.

is only transferred if there is coupling (e.g. dipolar) between ^{1}H and X nuclei, so CPMAS can also be used to tell if there is coupling between ^{1}H and X nuclei and also how strong the coupling is.

1.4 Instruments

Most of the experiments in this thesis were conducted with a Varian CMX300 NMR spectrometer. The spectrometer contains four parts: magnet, probe, console and computer.

1.4.1 Magnet

The magnet is made with a superconducting coil composed of a niobium alloy. The superconducting coil must be kept at a temperature lower than 10K to maintain the superconducting state. So liquid He is used to maintain the low temperature. To conserve the liquid He as long as possible, the container of liquid He is surrounded by liquid N_2. From Stefan-Boltzmann Law, the radiation power into liquid He is proportional to T^4 where T is about 300K if there is no liquid N_2 surrounding the liquid He. With liquid N_2, the surrounding temperature will be lowered to about 75K, so the radiation power into liquid He is decreased hugely. With this setup, 60L liquid He will last 4-6month. As shown in Figure 1.11, the NMR probe is lifted up into the magnet from the bottom. The heating gas flows in from the top via the tube inserted into the magnets room-temperature bore (89mm diameter). There is a thermocouple is placed in the bottom of stack used to monitor the temperature of sample. The Figure 1.12 is a photo of the magnet in our laboratory. The magnetic field is ~7 tesla. The NMR magnetic field strength is proportional to the proton NMR frequency, and thus the spectrometer is called a 300MHz NMR spectrometer.

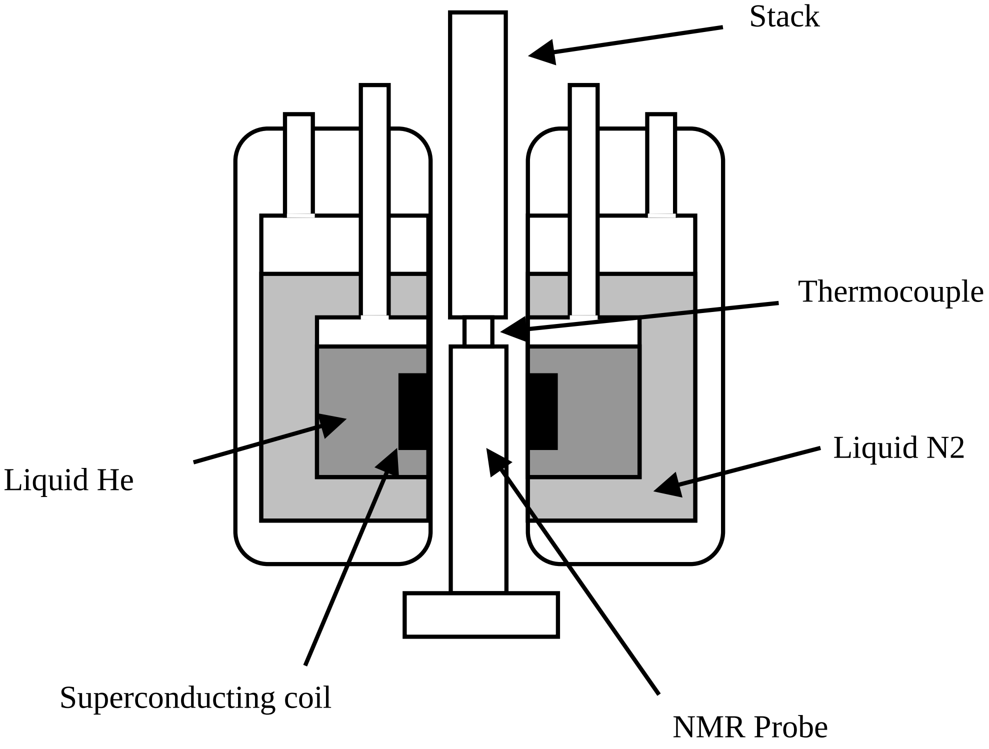

Figure 1.11 Sketch of magnet

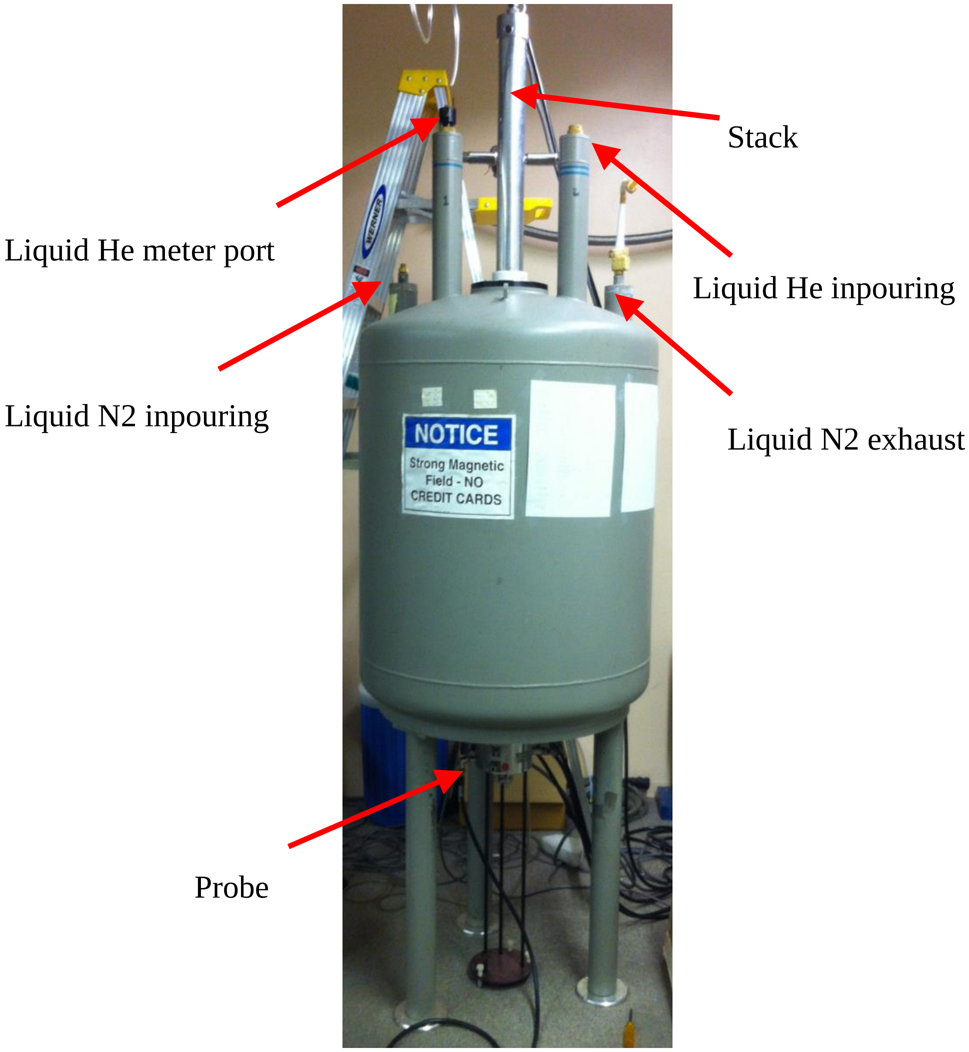

Figure 1.12 Photo of 7T magnet

1.4.2 NMR Probe

The element for basic signal acquisition of an NMR probe is an LC circuit (Figure 1.13), which is composed of two variable capacitors, one inductor and an r.f. coil. The r.f. coil (Figure 15(right)) is used to apply radio frequency pulses. The coil alone would have a huge impedance at high frequency, so we use an LC circuit tuned to the resonance frequency of the observed nuclei and matched to the impedance of whole circuit. The resonance frequency of the LC circuit can be adjusted using the total of the two variable capacitors, while the impedance match is achieved by careful adjustment of their ratio. The resonance frequency of the LC circuit must be adjusted to a value close to the NMR frequency at the beginning of measurement, every time.

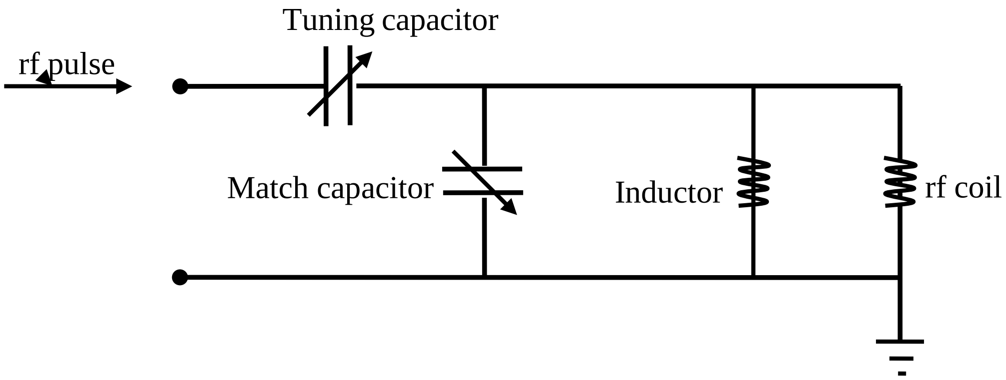

Figure 1.13 LC circuit of NMR probe

Two commonly used probes are a diffusion probe equalized with gradient coil and MAS probe. The former is mainly used for liquid samples and the latter for solid samples. The diffusion probe has a gradient coil (Figure 1.14 (left)) that can apply substantial magnetic field gradients, allowing diffusivity measurements. Two gradient coils (top and down) have

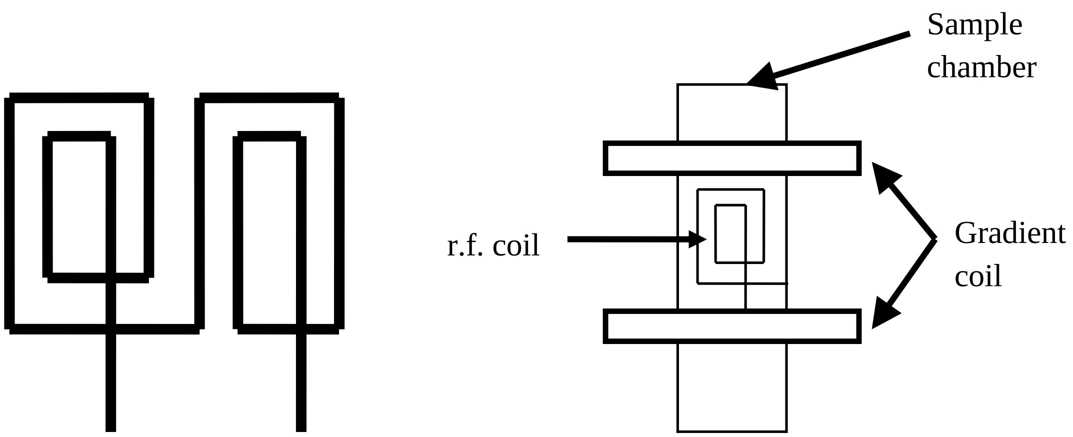

Figure 1.14 r.f. coil (left) and gradient coil (right) of diffusion probe

opposite directions of current, when the magnetic field gradient is applied. So the magnetic field due to coils in zero, but the gradient can be varied by control of the driving current. An MAS probe has a stator (Figure 1.15), which is used for magic angle spinning of a

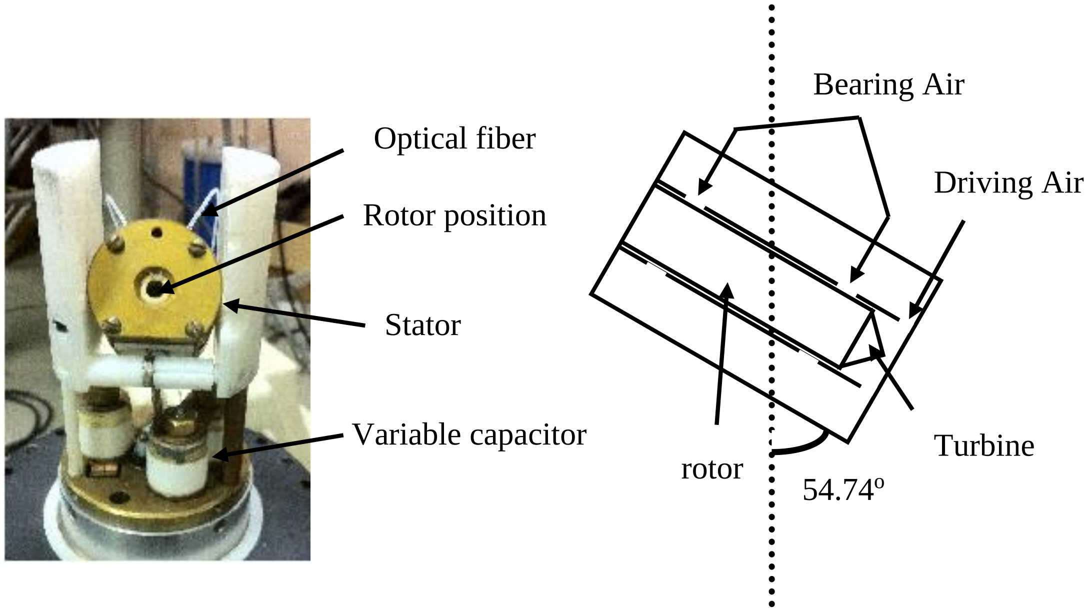

Figure 1.15. Stator of MAS NMR probe

sample in a tubular-shaped rotor. The main axis of stator is adjusted to an angle of 54.74^o with the ambient magnetic field. A solid sample is packed in the rotor and set inside of the stator. Two air flows are applied: bearing and driving at pressure to 40psi. The former flowsaround the rotor, therefore stabilizing the rotor and eliminating the friction between rotor and stator; the latter flows in a specific direction and drive the rotor's turbine, producing the spin. The optical fibers and diode laser are used to monitor the spin rate, via optical detection of the light reflected from alternating light and dark sections of the illuminated rotor as it spin. The spin rate can reach as high as 12 kHz.

1.4.3 Console

The console is composed of several electronic modules (Figure 1.16). Part A is used to apply gradient magnetic fields. Part B is used to generate radio frequencies. Part C is a single board computer (SBC) that is controlled by the spectrometer's Sun Blade work station, and thereby controls all other electronic devices. Part D is the receiver, used to receive induction signal of FID from preamplifier and deliver signals to the SBC. Part E is the transmitter, used to produce low power r.f. pulses. Part F is a two stage high frequency (H-power) amplifier, used to amplify r.f. power output at frequencies higher than 180MHz (for proton and fluorine nuclei). Part G is a low frequency power amplifier, used to amplify r.f. output at frequencies lower than 180MHz. Part H is the shim control, which is used to shim the ambient magnetic field, making it homogeneous to +/-0.1ppm

The computer is used to set all the parameters for NMR measurement and process the signal to get the NMR spectrum.

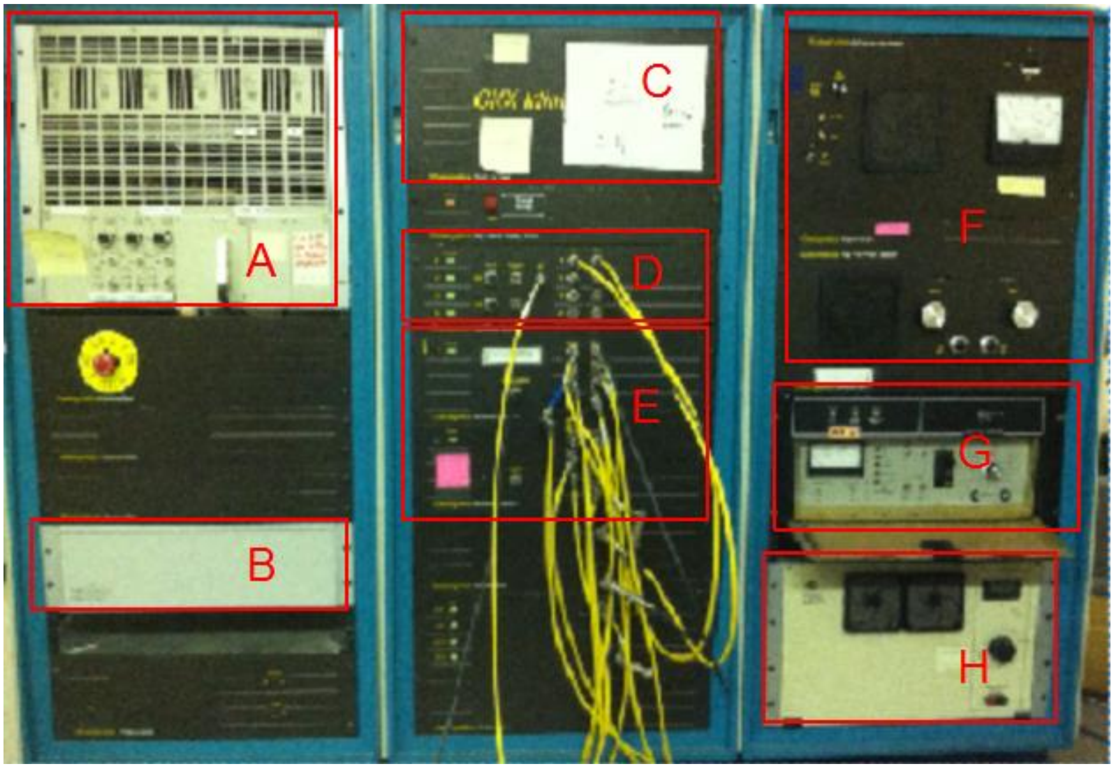

Figure 1.16 Console of NMR spectrometer

References

Abragam, A. 1961. *Principles of Nuclear Magnetism*. Oxford: Clarendon Press.

Andrew, E. R. 1981. MAGIC ANGLE SPINNING IN SOLID-STATE NMR-SPECTROSCOPY. *Philosophical Transactions of the Royal Society a-Mathematical Physical and Engineering Sciences* 299 (1452):505-520.

Andrew, ER. 1971. The narrowing of NMR spectra of solids by high-speed specimen rotation and the resolution of chemical shift and spin multiplet structures for solids *Progress in Nuclear Magnetic Resonance Spectroscopy* 8 (1):1-39.

BLOCH, F. 1946. NUCLEAR INDUCTION. *Physical Review* 70 (7-8):460-474.

BLOCH, F, WW HANSEN, and M PACKARD. 1946. THE NUCLEAR INDUCTION EXPERIMENT. *Physical Review* 70 (7-8):474-485.

Bloch, F. 1956. DYNAMICAL THEORY OF NUCLEAR INDUCTION .2. *Physical Review* 102 (1):104-135.

Farrar, Thomas. 1990. Density Matrices in NMR Spectroscopy: Part I. *Concepts in Magnetic Resonance* 2 (1):1-12.

Repeated Author. 1990. Density Matrices in NMR Spectroscopy: Part II. *Concepts in Magnetic Resonance* 2 (2):55-61.

Goldman, Maurice. 1990. *Quantum Description of High-Resolution NMR in Liquids*. Oxford: Oxford University Press.

Hahn, E. L. 1950. SPIN ECHOES. *Physical Review* 77 (5):746-746.

Hartmann, S. R., and E. L. Hahn. 1962. NUCLEAR DOUBLE RESONANCE IN ROTATING FRAME. *Physical Review* 128 (5):2042-&.

Lauterbur, P. C. 1973. IMAGE FORMATION BY INDUCED LOCAL INTERACTIONS - EXAMPLES EMPLOYING NUCLEAR MAGNETIC-RESONANCE. *Nature*

242 (5394):190-191.

Repeated Author. 1974. MAGNETIC-RESONANCE ZEUGMATOGRAPHY. *Pure and Applied Chemistry* 40 (1-2):149-157.

Lyerla, J. R., H. M. McIntyre, and D. A. Torchia. 1974. C-13 NUCLEAR MAGNETIC-RESONANCE STUDY OF ALKANE MOTION. *Macromolecules* 7 (1):11-14.

Maciel, G. E. 1984. HIGH-RESOLUTION NUCLEAR MAGNETIC-RESONANCE OF SOLIDS. *Science* 226 (4672):282-288.

Mackenzie, Kenneth J.D., and Mark E. Smith. 2002. *Multinuclear Solid-State NMR of Inorganic Materials*. Edited by R. W. Cahn, *Pefgamon Materials Series*. Oxford: Pergamon.

Mansfield, P. 1977. MULTI-PLANAR IMAGE-FORMATION USING NMR SPIN ECHOES. *Journal of Physics C-Solid State Physics* 10 (3):L55-L58.

Mansfield, P., and I. L. Pykett. 1978. BIOLOGICAL AND MEDICAL IMAGING BY NMR. *Journal of Magnetic Resonance* 29 (2):355-373.

Maricq, M. M., and J. S. Waugh. 1979. NMR IN ROTATING SOLIDS. *Journal of Chemical Physics* 70 (7):3300-3316.

Oldfield, E., and R. J. Kirkpatrick. 1985. HIGH-RESOLUTION NUCLEAR MAGNETIC-RESONANCE OF INORGANIC SOLIDS. *Science* 227 (4694):1537-1544.

Pake, G. E. 1950. FUNDAMENTALS OF NUCLEAR MAGNETIC RESONANCE ABSORPTION .1. *American Journal of Physics* 18 (7):438-452.

Repeated Author. 1950. FUNDAMENTALS OF NUCLEAR MAGNETIC RESONANCE ABSORPTION .2. *American Journal of Physics* 18 (8):473-486.

Pines, A., M. G. Gibby, and J. S. Waugh. 1973. PROTON-ENHANCED NMR OF DILUTE SPINS IN SOLIDS. *Journal of Chemical Physics* 59 (2):569-590.

PURCELL, EM, HC TORREY, and RV POUND. 1946. RESONANCE ABSORPTION

BY NUCLEAR MAGNETIC MOMENTS IN A SOLID. *Physical Review* 69 (1-2):37-38.

Rabi, II, JR Zacharias, S Millman, and P Kusch. 1938. A new method of measuring nuclear magnetic moment. *Physical Review* 53 (4):318-318.

Redfield, A. G. 1957. ON THE THEORY OF RELAXATION PROCESSES. *Ibm Journal of Research and Development* 1 (1):19-31.

Slichter, C. P. 1989. *Principles of Magnetic Resonance*. 3rd Ed ed. Berlin: Springer-Verlag.

Stejskal, E. O., and J. D. Memory. 1994. *High Resolution NMR in the Solid State*. Oxford: Oxford University Press.

TC, Farrar. 1987. *An introduction to pulse NMR spectroscopy*. Madison: The Farragut Press.

Wangsness, R. K., and F. Bloch. 1953. THE DYNAMICAL THEORY OF NUCLEAR INDUCTION. *Physical Review* 89 (4):728-739.

CHAPTER 2

NMR STUDY OF MRI CONTRAST AGENT

2.1 Introduction

2.1.1 Magnetic Resonance Imaging (MRI)

Magnetic resonance imaging (MRI) is a medical imaging technique based on acquisition of nuclear magnetic resonance signals. It has been widely used, because it can visualize internal structures of human body with high resolution and has almost no side effects. MRI was developed in 1970’s(Damadian 1971; Lauterbur 1973; Hinshaw, Bottomley, and Holland 1977) and put into broad medical use in 1980’s(Sijbers et al. 1996). At present, an improvement of magnet strength from 1.5T to 3T is underway worldwide, to improve the resolution of MRI.

Because of the high content of ^{1}H in the human body and the excellent sensitivity of ^{1}H for magnetic resonance, MRI signals are acquired from ^{1}H in body tissue . The basic idea is that ^{1}H will have different chemical properties in different types of body tissue. The differences are reflected in the NMR signals acquired in MRI, leading to contrast in the images. The most commonly used NMR properties for contrast control are relaxation times, especially the longitudinal relaxation time T_1(Morgan and Hendee 1984). The corresponding type of MRI image is said to be T_1-weighted. There are also different kinds of radio frequency and field gradient pulse sequences used in MRI. Here we use spin echo as an example(Bydder et al. 1983). A spin echo sequence in MRI is similar to those used in NMR, which also contain a 90^o pulse after with 180^o pulse. Besides that, MRI uses slice

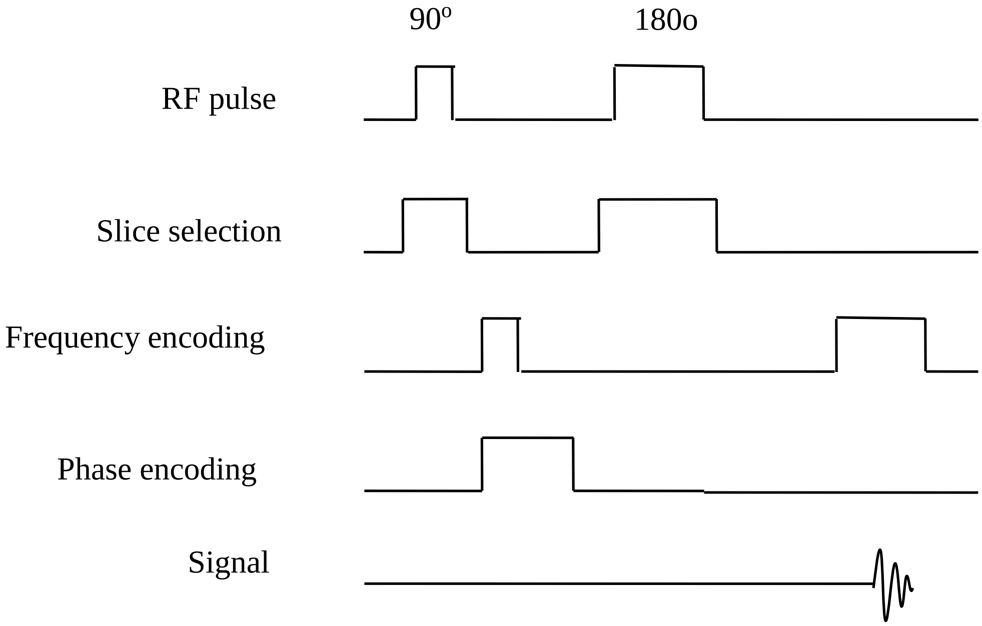

Figure 2.1 Pulse sequence of MRI

selection, phase encoding and frequency encoding to obtain 2D images. Slice selection uses the application of a magnetic field gradient along the large magnetic field axis when the 90^o r.f. is active. The gradient makes the different slices along the z axis have different nuclear magnetic resonance frequencies, so applying a narrow band r.f. pulse will only affect the selected slices. Therefore the acquired signals used to build up image are only from the selected slice. Phase encoding is the application of a magnetic field gradient with certain time length in one direction of the x-y plane perpendicular to the main field axis after a 90^o pulse. After the pulse, the magnetization will dephase because of this gradient. The phase of each spin at each position is different, and thus the phase labels, i.e. “encodes” the spins in the gradient direction. Frequency encoding is achieved by applying a third gradient when the signal is acquired. Applying all three gradients will cause a different frequency and phase of signal to be associated with each position in a sample. Thus phase and frequency encoding “labels” the position in 2D to get 2D imaging.

The signal intensity in a typical spin echo sequence is(Liang and Lauterbur 2000):

$$M = M_0(1 - \exp(-TR/T_1))\exp(-TE/T_2) \qquad (2.1)$$

Here TR is the repetition time of the pulse sequence, i.e. the time between successive 90^o slice selecting pulses, TE is the time to the formation of spin echo’s peak amplitude after which signal acquisition is initiated, and the M_0 depends on the proton density at a given spatial position.

From this equation we can see the signal intensity depends on the relaxation time (for a T_1-weighted image, a short TE used to make the signal not sensitive to T_2). Thus ^1H in different tissues gives rise to different signal strengths, resulting contrast in MRI.

2.1.2 MRI Contrast Agent

Sometimes the proton relaxation times in different tissues are close, so the contrast in MRI can be weak. In this case, a contrast agent (CA) can to be used to enhance image contrast. A CA is a kind of material that can shorten relaxation times, and therefore improve the visibility(Gore 1985). Besides that, shorter relaxation times can increase the speed of the imaging process.

Form the equation above, we can see that shortening the T_1 will increase the signal intensity, while shortening the T_2 will decrease the signal intensity. Based on this feature of MRI, contrast agents can be divided into two major species: positive and negative agents.

Usually a contrast agent cannot affect T_1 without affecting T_2, and vice versa. But a CA can have a larger effect on one relaxation time than on another. CA materials that mainly shorten longitudinal relaxation times (T_1) therefore increase the signal intensity, which are positive contrast agents, while the materials that mainly shorten transverse relaxation times (T_2) will decrease the signal intensity, and thus are negative contrast agents(Caravan 2006). At present the commercially used negative contrast agents are superparamagnetic iron oxide nanoparticles(Nakamura et al. 2000; Lee et al. 2007). The iron ion in nanoparticles has a large magnetic moment because of strong coupling, ferro- or antiferromagnetic coupling between iron ions. The large magnetic moment will cause large local inhomogeneity of the magnetic field, which will mainly shorten T_2.

Positive contrast agents all consist of gadolinium chelate complexes(Lauffer 1987; Caravan et al. 1999). Gd^{3+} contains 7 unpaired electrons. The electron has a spin magnetic moment much higher than the ^1H spin moment (about 658 times) and a much faster flipping rate. So unpaired electrons in a sample system will cause rapid local magnetic field fluctuation, which leads to shorter proton T_1. Gd^{3+} is the best ion available for shortening the relaxation time, however it cannot be directly used as a CA for the human body because

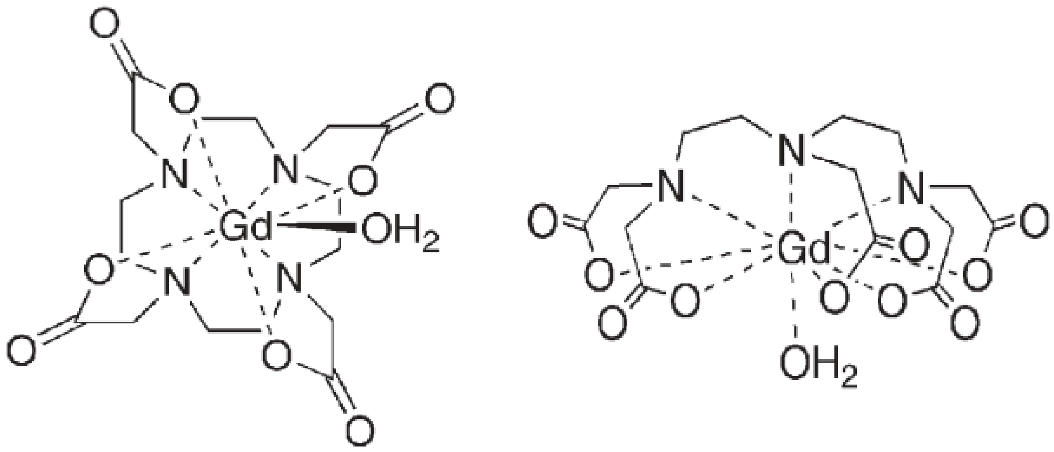

Figure 2.2 Construction of Gd(DOTA)(left) and Gd(DTPA)(right)(Caravan 2006)

of the toxic effect of Gd(Ersoy and Rybicki 2007). So Gd chelate complexes were developed(Carr et al. 1984; Oksendal and Hals 1993). Some Gd^{3+} chelates have been developed that have stable structures in the human body, which can act as a chemical shield against the toxic effect of $Gd^{3+.}$ Among these chelates are Gadopentetate (Gd(DTPA), Gadoterate (Gd(DOTA)). These two are already in wide commercial use, known by their commercial names as Magnevist and Dotarem.

The introduction of CA will shorten the relaxation time (T_1 or T_2) or we can say enhance the relaxation *rates* ($1/T_1$ or $1/T_2$) in proportion to the CA's Gd concentration. The ability of the CA to enhance the relaxation rate per mM of Gd is defined as the relaxivity (r) of the agent:

$$r_i = \frac{\Delta(1/T_i)}{[M]}\text{, i=1,2;} \tag{2.2}$$

Here [M] is the concentration of contrast agent or metal ion and $1/T_i$ is either the spin-lattice or spin-spin relaxation rate.

In order to get a decent contrast, the relaxation rate requires a change due to the CA of $0.5s^{-1}$ at least(Caravan 2006). The current commercial contrast agents have relaxivity about $4mM^{-1}s^{-1}$, so a rather high concentration of at least 0.125mM is needed. To increase the relaxation rate, more concentrated agent is needed or a contrast agent with higher relaxivity. Our research has been dedicated to producing materials with higher relaxivity than the contrast agents in general use at present.

2.1.3 Contrast Agent Relaxation Mechanism

Gd^{3+} has a large electronic magnetic moment and it can relax protons in water molecules nearby. Even with chelated Gd^{3+} ions, these nearby water molecules can exchange with bulk water, thus enhancing the average relaxation rate of all waters in the solution. The relaxed water is treated as residing mainly in three locations: inner-sphere water (one or two molecules), 2nd-sphere water (hydrogen bonded to oxygen in the carboxyl group of the chelate) and outer-sphere water (in the bulk).

Inner-sphere waters are the water molecules whose oxygen is coordinated to the Gd^{3+} ion itself. These waters have fast proton relaxation rates and exchange rapidly with bulk water. The ^1H relaxivity of inner-sphere water can be expressed as(Solomon 1955; Bloembergen and Morgan 1961; Lauffer 1987):

$$r_1^{IS} = \frac{q/[H_2O]}{(T_{1M} + \tau_m)} \qquad (2.3)$$

Where:

$$\frac{1}{T_{1M}} = \frac{2}{15}\left(\frac{\mu_0}{4\pi}\right)^2 \frac{\hbar^2 \gamma_S^2 \gamma_H^2}{r_{GdH}^2} S(S+1)\left[\frac{3\tau_{c1}}{1+\omega_H^2 \tau_{c1}} + \frac{7\tau_{c2}}{1+\omega_S^2 \tau_{c2}}\right] \qquad (2.4)$$

$$\frac{1}{\tau_{ci}} = \frac{1}{\tau_M} + \frac{1}{\tau_R} + \frac{1}{T_{ie}}; i = 1,2 \qquad (2.5)$$

$$\frac{1}{T_{1e}} = \frac{12}{5}\Delta^2 \tau_v \left(\frac{1}{1+\omega_S^2 \tau_v^2} + \frac{4}{1+4\omega_S^2 \tau_v^2}\right) \qquad (2.6)$$

$$\frac{1}{T_{2e}} = \frac{12}{10}\Delta^2 \tau_v \left(3 + \frac{5}{1+\omega_S^2 \tau_v^2} + \frac{2}{1+4\omega_S^2 \tau_v^2}\right) \qquad (2.7)$$

In formular 2.4-2.7 q is the number of inner waters (one or two, for Gd(DTPA) q=1); $[H_2O]$ is the total water concentration in mM; T_{1M} is the longitudinal relaxation time of inner water; γ_S and γ_H are the gyromagnetic ratios of the electron and proton respectively; r_{GdH} is the distance between Gd^{3+} ion and the proton in the inner water; S is electron spin number, which is 7/2 for Gd^{3+}; ω_H and ω_S are the Larmor frequencies of the proton and the electron ($\omega_S=658\omega_H$); τ_M is the mean lifetime of the inner water (the water molecule's exchange correlation time); τ_R is the chelated Gd molecule's rotational correlation time; T_{ie} are electronic relaxation times (longitudinal or transverse relaxation); Δ^2 is the mean value of the transient zero-field splitting caused by random fluctuations in the electronic environment surrounding the Gd^{3+} in the chelate; τ_v is the correlation time of these random fluctuations.

The first equation is valid if $q/[H_2O] \ll 1$ and $T_{1M} > \tau_M$ (Bloembergen and Morgan 1961). Usually, contrast agents have one bonded water because the Gd^{3+} is capable of forming 9 coordination bonds, eight of them being bonds to the chelating agent to form a stable structure, leaving one for water. There are two terms in second equation: called the 3-term and 7-term. The 3-term depends mainly on the proton Larmor frequency and the 7-term depends mainly on the electron Larmor frequency. The electron Larmor frequency is much larger than the proton Larmor frequency ($\omega_S=658\omega_H$). When the frequency increases, the 7-term always decreases first. This decrease is called a "dispersion" of the term with frequency. So the 3 term is dominant at high frequency (>5MHz for Gd(DTPA))(Caravan et al. 1999). The relaxation of inner water protons comes from the dipole-dipole interaction between unpaired electrons in Gd^{3+} and these protons. As mentioned in first chapter, the fluctuation of fields acting on inner water comes from rotation of the Gd(DTPA) molecule with correlation time τ_R, the exchange motion of the water molecule with its correlation time τ_M and the electronic spin's relaxation time T_{ie}, so the total correlation time is determined by three parts, as eq. 2.5. The electronic relaxation times are explained by a theory called zero-field splitting, which applies to the situation of electronic spin S>1/2. The zero-field splitting mainly arises from the interaction of two neighboring electron spins and sometimes is also affected by the spin-orbit coupling(Bloembergen and Morgen 1961; Kowalewski et al. 1981).

The 2nd-sphere water consists of water molecules having a hydrogen bonded to oxygen atoms in the ligands. The relaxivity of 2nd-sphere water can be expressed in a treatment similar to that of inner sphere water, but with different parameters, like the number of hydrogens (q), the distance of hydrogen to Gd^{3+} and molecular exchange lifetime of hydrogen(Aime et al. 1997; Botta 2000). All these parameters are hard to determine, which makes 2nd-sphere water relaxivity ambiguous. It was noticed in the measurement of $Gd(DOTP)^{5-}$ which has a relaxivity similar to $Gd(DTPA)^{2-}$(Caravan et al. 2001). However, the ^{17}O R_{2r} measurement shows there is no inner water in $Gd(DOTP)^{5-}$. And the relaxivity is too high to attribute to outer water only. It turns out that the phosphonate group in DOTP has a strong ability to form hydrogen bonds with water (Aime et al. 1995). Sometimes, the 2nd-sphere water is also categorized as out-sphere water(Bottrill, Nicholas, and Long 2006). However this term is not to be confused the more widely-used term "outer-sphere water", which refers to the external water in a solution or suspension that has no bonding with the complex and whose relaxivity comes from diffusion of water molecules. The Gd(DTPA) and water molecules are treated as hard spheres and this part of the proton relaxivity can be calculated with equations(HWANG and FREED 1975; FREED 1978):

$$r_1^{OS} = \frac{32\pi}{405}\gamma_H^2\gamma_S^2\hbar^2 S(S+1)\frac{N_A}{1000dD}\left[3j(\omega_H)+7j(\omega_S)\right] \tag{2.8}$$

Where:

$$j(\omega) = \mathrm{Re}\left(\frac{1+\frac{z}{4}}{1+z+\frac{4z^2}{9}+\frac{z^3}{9}}\right) \tag{2.9}$$

$$z = \sqrt{i\omega\tau_D + \frac{\tau_D}{T_{1e}}} \tag{2.10}$$

$$\tau_D = \frac{d^2}{D} \tag{2.11}$$

Here D is the diffusion constant of water, τ_D is diffusional correlation time, d is the hopping distance of water molecule, and N_A is Avogadro's number.

We are also interested in the reduced ^{17}O transverse relaxation rate (R_{2r}) because it is possible to measure its temperature dependence and thereby determine the water molecular exchange rate of inner water. The ^{17}O R_{2r} in a Gd(DTPA) solution can be represented by the following equation(Swift and Connick 1962; Swift et al. 1964):

$$R_{2r} = \frac{1}{T_{2r}} = \frac{1}{P_M}\left[\frac{1}{T_2}-\frac{1}{T_{2A}}\right] = \frac{1}{\tau_M}\frac{T_{2M}^{-2}+\tau_M^{-1}T_{2M}^{-1}+\Delta\omega_M^2}{(\tau_M^{-1}+T_{2M}^{-1})^2+\Delta\omega_M^2}+\frac{1}{T_{2OS}} \tag{2.12}$$

where P_M is the mole fraction of bound water; T_2 is the measured transverse relaxation time of ^{17}O; T_{2A} is the reference transverse relaxation time (measured using acidified water with the same pH as the Gd(DTPA) solution); T_{2M} is the transverse relaxation time of bound water; $\Delta\omega_M$ is the chemical shift difference between bound water and bulk water; T_{2OS} is the relaxation rate of our sphere water. The contribution of the outer sphere water is negligible in R_2(Micskei et al. 1993). If the isotropic shift is small (the $\Delta\omega_M$ can be negligible), the equation can be simplified to:

$$\frac{1}{T_{2r}} = \frac{1}{T_{2M} + \tau_M} \tag{2.13}$$

The bound oxygen relaxation is dominated by the scalar relaxation mechanism, and can be calculated by(Micskei et al. 1993):

$$\frac{1}{T_{2M}} = \frac{(A/\hbar)^2}{3} \mathrm{S}(\mathrm{S}+1)\left(\tau_{1S} + \frac{\tau_{2S}}{1+\omega_S^2\tau_{2S}^2}\right) \tag{2.14}$$

$$\frac{1}{\tau_{iS}} = \frac{1}{\tau_M} + \frac{1}{T_{ie}}; i = 1,2 \tag{2.15}$$

The exchange correlation time τ_M decreases with temperature but the transverse relaxation time T_{2M} increases with temperature because of the τ_{1S} term. So at low temperature R_{2r} is dominated by τ_M and increases with temperature (slow exchange regime); at high temperature, and R_{2r} is dominated by T_{2M} and decreases with temperature (fast exchange regime). [S. Aime et. 1999]

2.1.4 Layered Double Hydroxide (LDH)

Layered double hydroxides (LDH) are compounds whose structure consists of alternate metal hydroxide layers and interlayer anions(Cavani, Trifiro, and Vaccari 1991; Rives and Ulibarri 1999). The metal layer has a structure like brucite, $Mg(OH)_2$, where each Mg^{2+} is octahedrally surrounded by six OH^- ions (Figure 2.3). Except for the top and bottom face, each face of the octahedron is shared with other octahedra, thereby forming a metal hydroxide layer. In LDH, a fraction of the Mg^{2+} ions are replaced by trivalent cations, such

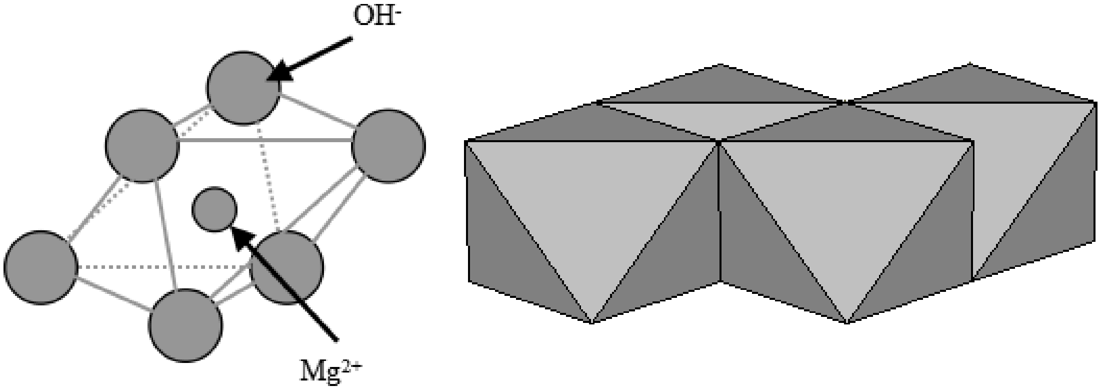

Figure 2.3 Octahedron constituted by six OH^- and one Mg^{2+}(left); Metal layer constituted by multiple octahedrons(right)

as Al^{3+}, but the metal hydroxide layer structure stays the same as brucite. The extra positive charge of the trivalent cation is balanced by anions located between the metal hydroxide layers. The chemical formula of LDH can be expressed as $[M^{2+}_{1-x}M^{3+}_{x}(OH)_2]^{+}(A^{n-})_{x/n}\bullet nH_2O$, where the M is metal ion and A is anion. The bivalent metal could be Mg^{2+}, Zn^{2+}, Ca^{2+}; the trivalent metal could be Al^{3+}, Fe^{3+} and the cation could be CO_3^{2-}, Cl^-, SO_4^{2-}.

LDH compounds are of wide interested to researchers because they are excellent anion-hosting materials. They have already been used as catalysts for chemical reactions, environmental remediation, ceramic precursors etc.(Cavani, Trifiro, and Vaccari 1991; Oh, Biswick, and Choy 2009). Also, LDH is highly biocompatible(Kwak et al. 2002), which makes it popular in biomedical fields. The cytotoxicity and therapeutic efficacy of LDH in vivo tests have been reported(Li et al. 2011; Qin et al. 2010; Silion et al. 2010). Based on these properties of LDH NPs, it can be used as a host for MRI contrast agents, as is reported in this thesis.

2.2 Experimental Section

2.2.1 Gd(DTPA) Intercalated LDH (Gd(DTPA)/LDH)

A new material, Gd(DTPA) intercalated with LDH has been successfully synthesized for the first time by X. Sun, working in Prof. S. K. Dey's laboratory in SEMTE. With thermal treatment of LDH and Gd(DTPA) solutions at certain temperature, interlayer exchange happens and Gd(DTPA)$^{2-}$ can replace an interlayered anion, such as Cl$^-$ or NO$_3^-$, in LDH. From the XRD pattern(Figure 2.4) we can see thta Gd(DTPA)$^{2-}$ replaces NO$_3^-$ anion in the layer between metal ions and the interlayer spacing is expanded from the value 0.753nm, typical of layer spacings of LDH(Brateman, Xu, and Yarberry 2004; Cavani, Trifiro, and

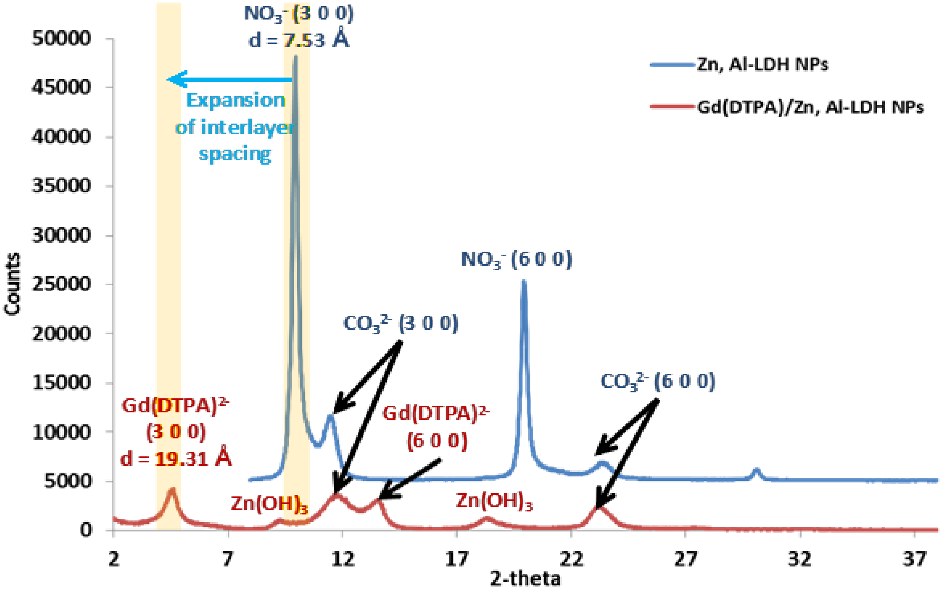

Figure 2.4 XRD pattern of Zn, Al-LDH NPs and Gd(DTPA)/Zn, Al-LDH NPs

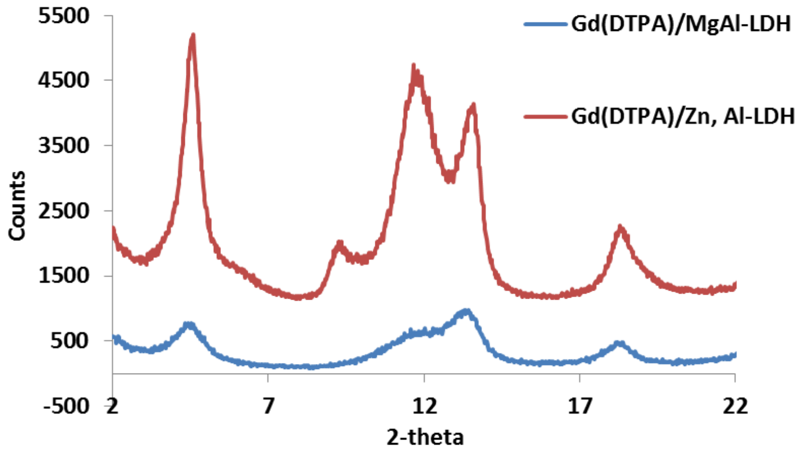

Figure 2.5 XRD pattern of Gd(DTPA)/Mg, Al-LDH and Gd(DTPA)/Zn, Al-LDH

Vaccari 1991), to 1.931nm in Zn,Al-LDH and 2.2nm in Mg,Al-LDH, which is attributed to intercalation of Gd(DTPA) molecules. The interlayer anion CO_3^{2-} anion is more difficult to replace by $Gd(DTPA)^{2-}$. But it's hard to make LDH NPs without CO_3^{2-} because the CO_2 in the air always participates in the synthesis reaction. We have studied two types of LDH with Gd(DTPA) intercalation: Mg, Al-LDH and Zn, Al-LDH. From the XRD patterns of

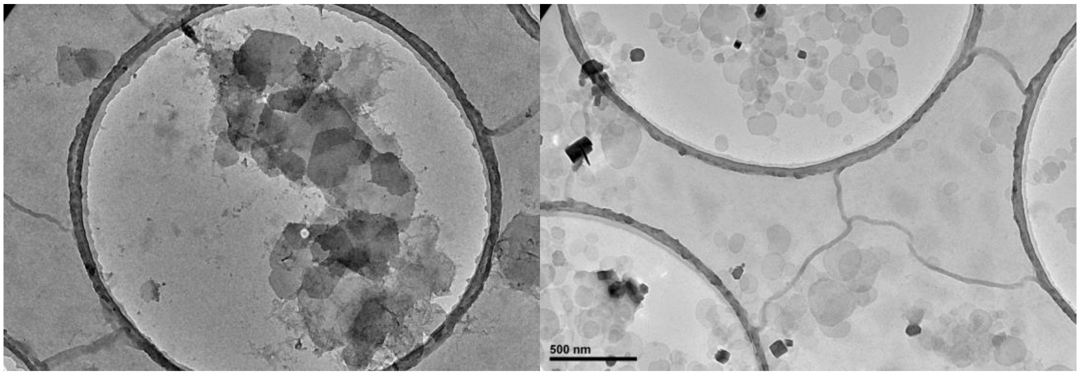

Figure 2.6 TEM of Zn,Al-LDH (left) (DLS: 357.2nm) and Mg,Al-LDH (right) (DLS: 142.0nm)

these two types of intercalated LDH NPs (Figure 2.6), we can see they have similar patterns but Mg, Al-LDH has lower intensity of X-ray lines, which means that Mg,Al-LDH has lower crystallinity than Zn,Al-LDH. Also, the crystallinity of Mg,Al-LDH can vary with the synthesis procedure.. The TEM of two types of NPs are shown in Figure 2.6, in which the LDH nanoparticles can be observed and their average size can be determined

2.2.2 NMR study of Gd(DTPA) intercalated LDH

Relaxation times T_1 and T_2 of water ^{1}H are measured at variable temperature using a Varian CMX300 NMR spectrometer operating at 300MHz NMR frequency. T_1 was measured with the inversion recovery method and T_2 was measured using spin echoes. T_1 of ^{1}H was also measured at several other NMR frequencies including 15.4MHz, 22MHz and 128MHz. The last is the standard frequency of MRI scanners operating at 3T.

^{17}O NMR was observed at natural abundance, and the T_2 of ^{17}O was measured at variable temperature, using the Varian CMX300 NMR spectrometer.

2.3 Results and Discussion

2.3.1 Relaxivity Measurement

From the longitudinal relaxation rate vs. Gd concentration measurement (Figure 2.7) of several different compounds of Gd(III) solution using 15.4MHz NMR, we can see that the relaxation rate of Gd(DTPA)/LDH is proportional to the concentration of Gd, so the relaxivity of Gd(DTPA)/LDH is the slope of a linear fit of relaxation rate vs. concentration of Gd in our nanoparticles (NPs) suspension samples. Relaxivity comparisons are listed in Table 2.1. At 15.4MHz, Gd(DTPA)/LDH NPs have a much higher relaxivity than

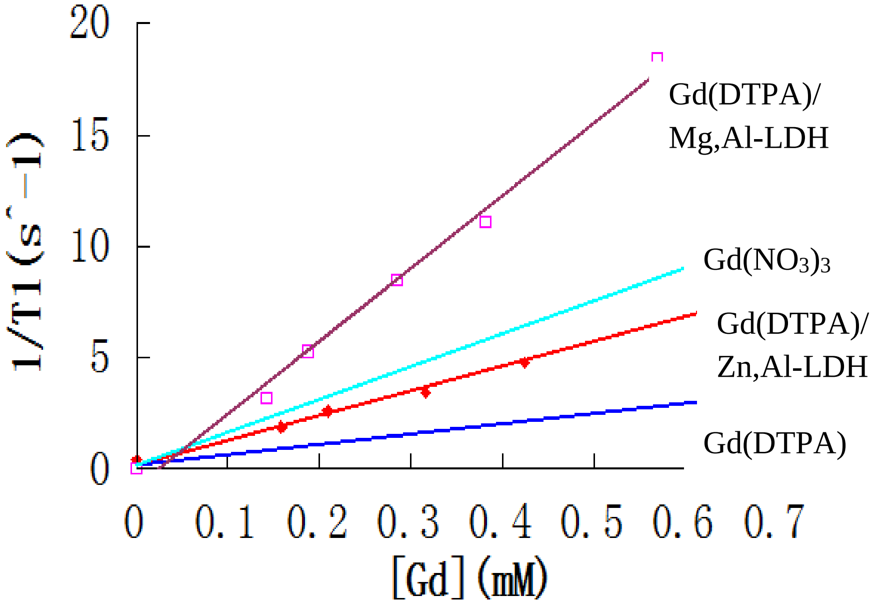

Figure 2.7 longitudinal relaxation rate vs Gd concentration of different Gd(III) solution using 15.4MHz NMR spectrometer (the error of each relaxation rate measurement is smaller than 3%, which is too small to show a clear error bar, so the error bar is not added in this and following figures.)

Table 2.1 relaxivity of several Gd(III) solution at 15MHz

solution	Gd(DTPA)/ Mg, Al-LDH	Gd(DTPA)/ Zn,Al-LDH	$Gd(NO_3)_3$	Gd(DTPA)
Relaxivity ($mM^{-1}s^{-1}$)	32.5	11.1	14.8	4.63

Gd(DTPA) ions in solution. Mg, Al-LDH has even higher relaxivity (as large as ~$30mM^{-1}s^{-1}$) than Gd^{3+} ion in solution. So Gd(DTPA)/LDH is a promising material for use as a contrast agent.

Figure 2.8 is a comparison of relaxivities at two different intercalation percentages, obtained at two different Larmor frequencies. Two Gd(DTPA)/Mg,Al-LDH NPs were made with similar sizes but different intercalation percentages (ratios of $2[Gd(DTPA)^{2-}]$

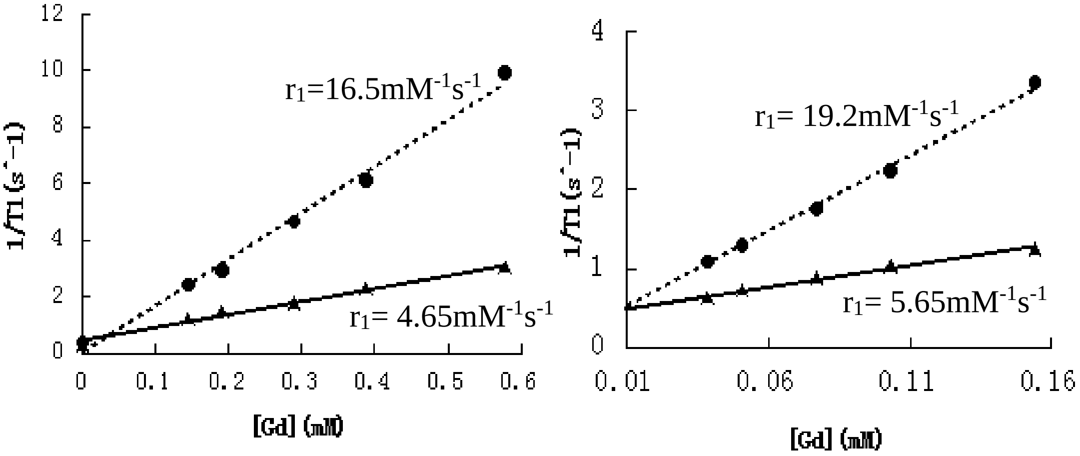

Figure 2.8 Relaxivity measurement (dashed line:15MHz; solide line:300MHz)of Gd(DTPA)/LDH with different percentage of intercalation: (a) 2Gd(DTPA)$^{2-}$:Al^{3+}=0.3107:1(size:359.7nm); (b) 2Gd(DTPA)$^{2-}$:Al=0.1054:1(315.3nm);

and [Al^{3+}]) (each Al^{3+} in LDH contribute only one extra positive charge to the metal layer, which mainly has Mg^{2+}. So it takes two Al^{3+} ions in the metal layer to balance out the two negative charge in Gd(DTPA)$^{2-}$. In another word, the 2[Gd(DTPA)$^{2-}$]:[Al^{3+}]=1:1 with 100% intercalation). As the Larmor frequency increases from 15.4MHz to 300MHz, the relaxivity decrease to about one third. This behaviour, decreasing relaxivity with frequency, is similar to that of Gd(DTPA) in solution. Also, a higher intercalation percentage is observed to have a negative effect on relaxivity when the NPs in suspension have similar particle size.

Figure 2.9 shows the Zn/Al-LDH NPs size dependence of longitudinal relaxivity at two Larmor frequencies, 15.4MHz and 22MHz. The details of these five Zn/Al-LDH NPs, including size and intercalation percentage, are listed in Table 2.2. These samples have

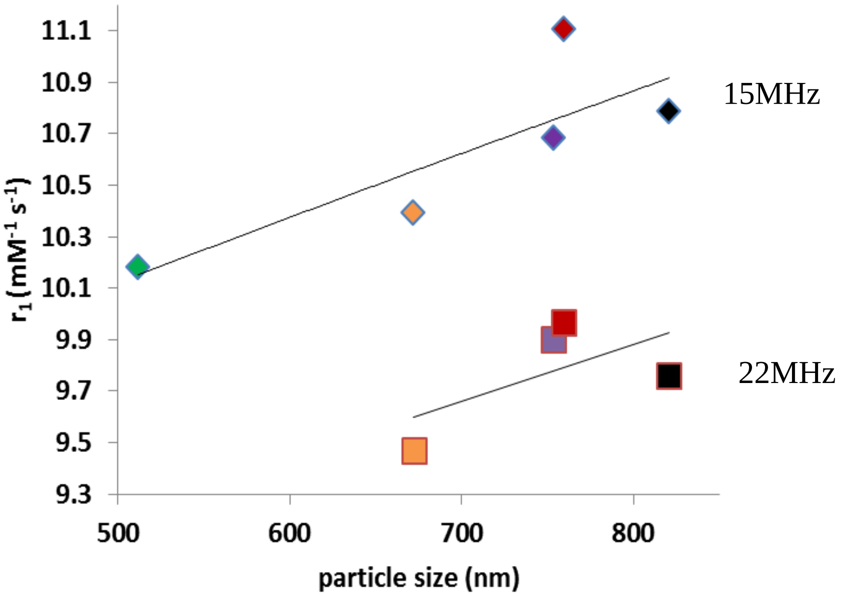

Figure 2.9 Longitudinal relaxivity of Gd(DTPA)/Zn,Al-LDH with different NPs size. (intercalation percentage 2Gd(DTPA)$^{2-}$:Al^{3+}≈0.5:1) (The straight lines are only trend indicators, not linear fits. Individual relaxivity errors are of order 2%)

Table 2.2: Relaxivity of five different Zn,Al-LDH NPs

Particle Size (nm)	2 Gd(DTPA):Al	Relaxivity(mM^-1·s^-1)	
		15MHz	22MHz
511.5	0.5391:1	10.18	
672.1	0.4459:1	10.39	9.47
753.7	0.5231:1	10.68	9.9
759.4	0.5094:1	11.11	9.97
820.3	0.5663:1	10.79	9.76

quite high intercalation percentage, around half-maximum intercalation ($[2Gd(DTPA)^{2-}]:[Al^{3+}] = 0.5:1$). The relaxivity is lower at 22MHz than at 15.4MHz and slightly increases with NP size.

Figure 2.10 is the relaxation rate dependence on pH, which shows that the relaxation rate decreases with pH. During the measurements, the initial pH 5.4 of a Gd(DTPA)/Zn,Al-LDH was increased by adding concentrated LiOH into the sample. In the process of varying pH, the concentration of Gd(DTPA) varied less than 10%. At pH=9.49, agglomeration can be clearly observed. This is because the OH^- will absorb on the surface of LDH NPs and neutralize the residual positive surface charge, leading to agglomeration of the NPs.

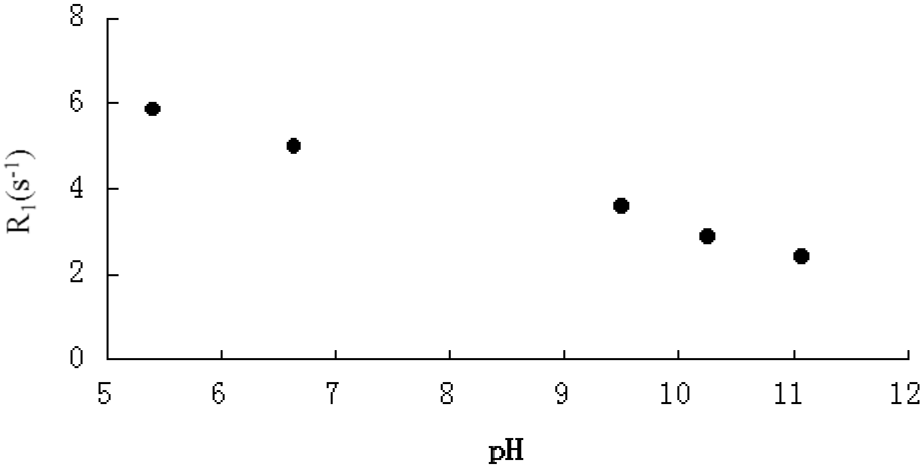

Figure 2.10 Longitudinal relaxation rate of Gd(DTPA)/Zn,Al-LDH dependence on pH

Figure 2.11 shows results of r_1 measurement at several different ^1H Larmor frequencies (15.4MHz, 22MHz, 128MHz and 300MHz). Both Gd(DTPA)/Mg,Al-LDH and Gd(DTPA)/Zn,Al-LDH were measured, except for Gd(DTPA)/Mg,Al-LDH at 22MHz. It is seen that Gd(DTPA)/Mg,Al-LDH has higher relaxivity than Gd(DTPA)/Zn,Al-LDH at each frequency. Again, r_1 decreases with frequency increase. As noted above, 128MHz is the medical clinically used frequency. At this frequency, the relaxivity of Gd(DTPA)/Mg,Al-LDH is $6.5 mM^{-1}s^{-1}$ which is about 50% higher than Gd(DTPA). The higher relaxivity of Gd(DTPA)/Mg,Al-LDH than Gd(DTPA)/Zn,Al-LDH can be attributed to outer sphere water(or 2nd-sphere water). The Gd(DTPA)/Mg,Al-LDH has lower crystallinity than Gd(DTPA)/Zn,Al-LDH, So the outer sphere water(or 2nd-sphere water) may have a higher exchange rate.

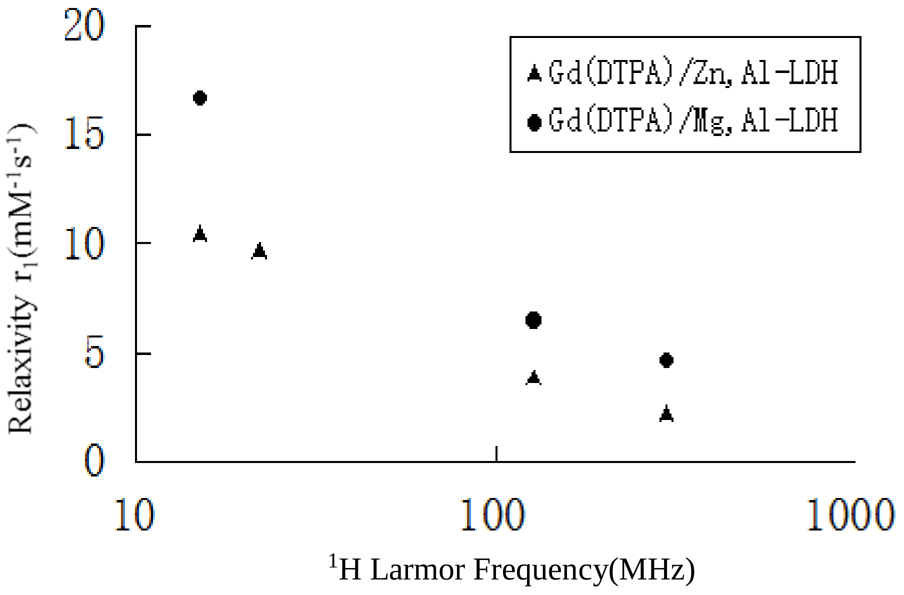

Figure 2.11 relaxivity r_1 of two types of NPs measured at several different ^1H Larmor frequency.

Figure 2.12 shows a theoretical calculation of Gd(DTPA)/Zn,Al-LDH's relaxivity over the frequency range of 1-300 MHz. The simulation uses the inner water relaxivity only. The simulation results are: values for the exchange correlation time τ_m (1.58ms), for the correlation time for the modulation of zero-field splitting τ_v (0.16ps) and mean square amplitude of the transient zero-field splitting Δ^2 (~$11*19^{19}s^{-2}$). Using inner water relaxivity only for simulation is a good approximation for Zn,Al-LDH suspensions because outer water relaxivity arises from diffusion of water molecules around Gd(DTPA) molecules, and in LDH suspensions, these waters form a constricted interlayer with much slower diffusion than in bulk water (the diffusion correlation time in LDH layers is approximate 10^5 times longer than pure water (the estimation using correlation time of LDH NPs(Dupuis et al. 1990) without intercalation, although Gd(DTPA)/LDH might have shorter correlation time because of spacing expansion)). So the outer water contribution is negligible. However, a similar calculation for Gd(DTPA)/Mg,Al-LDH can't be fitted to

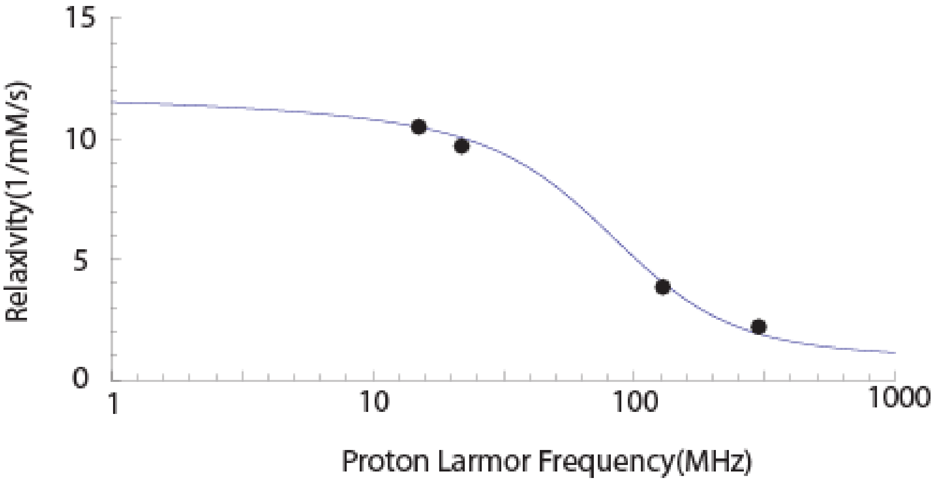

Figure 2.12 Simulation of Gd(DTPA)/Zn,Al-LDH's relaxivity

experiment using only inner water relaxivity, which means there is another relaxivity mechanism present besides inner sphere water. Considering that Gd(DTPA)/Mg,Al-LDH has lower crystallinity, the outer sphere(2nd-sphere) water may make an important contribution at high frequency. In these NP suspensions, this contribution has proved difficult to calculate.

Figure 2.13 shows the ^{17}O transverse relaxation rate (R_2) of Gd(DTPA)/Zn,Al-LDH dependence on temperature. The relative relaxation rate ($1/T_2$-$1/T_{2,ref}$) of Gd(DTPA)/Zn,Al-LDH uses a suspension of unintercalated LDH NPs as a reference, so the result eliminates the effect of oxygen quadrupolar relaxation and other possible effects arising from LDH. The relative relaxation rate of Gd(DTPA) uses pure water as reference. R_2 of ^{17}O increases with temperature, which means that water is in a slow exchange regime

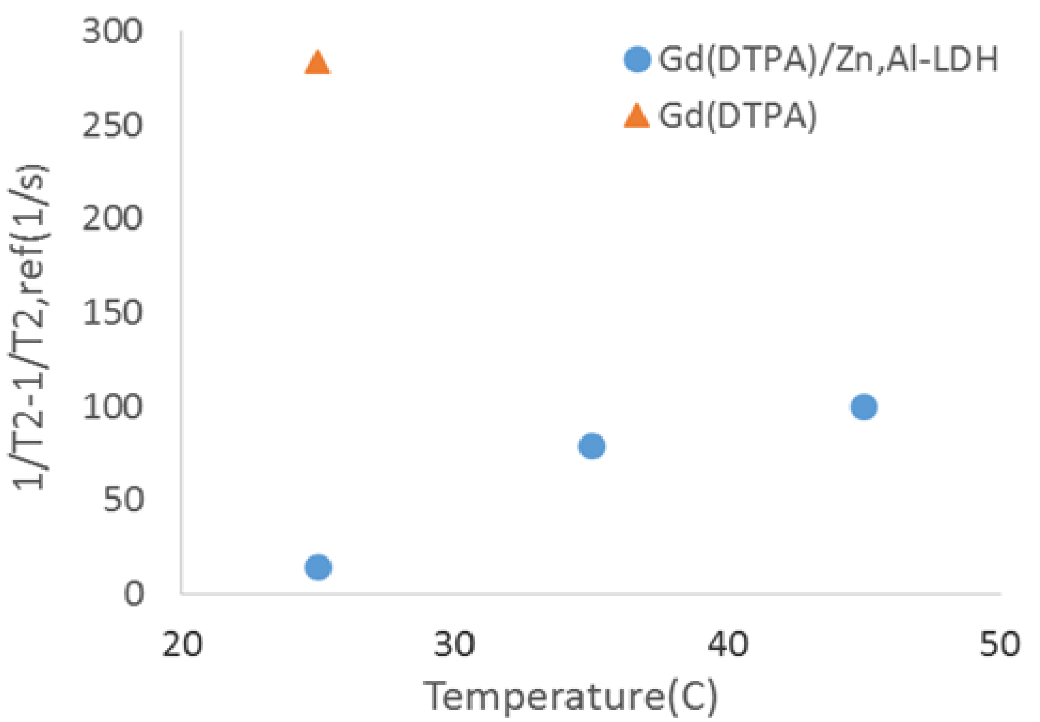

Figure 2.13 ^{17}O transverse relaxation rate of Gd(DTPA)/Zn,Al-LDH dependence on temperature

(longer mean inner water residence time relative to the inner water-coordinated intrinsic ^{17}O spin relaxation time T_2). Also, the R_2 of Gd(DTPA)/Zn,Al-LDH is much smaller than Gd(DTPA). This could also be explained by slow exchange of water molecule. With slow water exchange, the Gd^{3+} relaxation of ^{17}O would become small in Gd(DTPA)/Zn,Al-LDH, and is dominated by the huge quadrupolar relaxation of ^{17}O, so the effect upon ^{17}O relaxation from Gd^{3+} in the suspension sample itself becomes very small. However, these ^{17}O NMR results to date are obtained at the natural abundance concentration of ^{17}O, not from enriched samples, so the ^{17}O-^{17}O spin-spin interaction contribution to the measured T_2^{-1} relaxation rates are negligible, making both the measurements of T_2 and their interpretation difficult.

2.3.2 Mechanism of Relaxivity Enhancement

With intercalation of Gd(DTPA), the clearest change is the dramatic increase of the rotation correlation time(τ_R). This correlation time can be estimated from the Debye-Stokes equation:

$$\tau_R = \frac{4\pi r^3 \eta}{3k_B T} \tag{2.16}$$

Here r is radius of particle; η is the viscosity of solution; k_B is the Boltzmann constant.

In Gd(DTPA) solution, τ_R is 58ps(Powell et al. 1996), and is the dominant term in the total water proton T_1 relaxation's correlation time. T_{1e} increases from 0.07ns to 2ms when the frequency increases from 0.01MHz to 1000MHz. So at low frequency the T_{1e} term is also dominant but it's not at higher frequencies (>3MHz). As mentioned before, the 7-term, in equation 2.4, dispersed at frequencies higher than 5MHz, and the 3-term in equation 2.4, has a maximum around 2.6GHz ($\omega\tau=1$) which is much higher than medical clinic MRI frequency (128MHz). With intercalation the size of particle increases dramatically. Assuming a particle with size 100nm, the τ_R would have to be of order of 0.1ms, so the $1/\tau_R$ term is much smaller than $1/\tau_M$ and $1/T_{1e}$. Thus the $1/\tau_R$ term in equation II.5 makes a negligible contribution to the total correlation time, and τ_{c1} would increase. Therefore the maximum frequency would be lower and would enhance the relaxivity at the required frequency range. The positive effect on relaxivity of increasing τ_R has been proved by simulation(Caravan et al. 1999). So the vanishing of $1/\tau_R$ term coupled with increase of the electronic $1/T_{1e}$ term are the main reasons of enhancement for relaxivity in Gd(DTPA)/LDH nanoparticle suspensions.

Also, with intercalation, the bonded water on Gd^{3+}, instead of directly exchanging with bulk water, can only exchange with interlayer water of LDH. In this case, we can expect that the water exchange correlation time (τ_m) is longer than in Gd(DTPA). Both the simulation result (Figure 2.11) and R_2 measurement of ^{17}O (Figure 2.12) are consistent with this expectation. The simulated τ_m is 1.58μs which is much longer than 0.32μs in Gd(DTPA)(Powell et al. 1996). This length of τ_m is of the same order as T_{1M}, which has a negative effect on relaxivity. So a long τ_m is a restriction to obtaining higher relaxivity. This can explain why a higher intercalation percentage will lower the relaxivity (Figure 2.8). Because of slow exchange of water, the Gd(DTPA) at the edges of LDH NPs are most effective. The higher intercalation percentage might thus increase the portion of Gd(DTPA) with slower effective inner water exchange.

The sizes of Gd(DTPA)/LDH NPs increase from 500nm to 800nm (Figure 2.9), and τ_R increases from about 2.5 to 6.4ms. Considering that the $1/\tau_R$ term is negligible in equation 2.5, the change of nanoparticle size should not induce a change of relaxivity, which is also validated in the simulation. So the increase of relaxivity probably comes from the distribution of Gd(DTPA).

The electronic relaxation time depends on chemical bonding of molecule and molecular symmetry, so it also should be affected by intercalation, but at present intercalation's effects on this time are not understood.

2.4 Conclusion

In order to develop new MRI contrast agents, Gd(DTPA)-intercalated LDH has been successfully synthesized. The new material has a higher relaxivity than Gd(DTPA) in solution, especially at low frequency. At the clinical MRI frequency 128MHz, Gd(DTPA)/Mg,Al-LDH has a relaxivity of 6.5mM^{-1}s^{-1} which is much higher than the relaxivity of Gd(DTPA). So Gd(DTPA)/Mg,Al-LDH is a candidate for use as MRI contrast agent.

To understand the mechanism of relaxivity in nanoparticles, a series of experiments have been done. It is shown that the relaxivity enhancement of Gd(DTPA)/LDH is closely connected with the strong increase of the rotational relaxation correlation time (especially in the low frequency range (~15MHz)), but can be restricted by decrease of the water molecule exchange correlation time. It is also possible to intercalate other Gd complexes with shorter exchange times (like Gd(EGTA)) into LDH NPs, to improve relaxivity. With high crystallinity of LDH NPs (Zn,Al-LDH), the relaxivity contribution of outer water can be negligible. However, lower crystallinity of LDH (Mg,Al-LDH) has a positive effect on the relaxivity, which probably arise from the contribution of outer water molecules, i.e. those outside of the Gd^{3+} chelate's inner shell. The outer water molecules' contribution could the mainly reason of relaxivity enhancement in high frequency range (300MHz).

References

Aime, S., P. Ascenzi, E. Comoglio, M. Fasano, and S. Paoletti. 1995. MOLECULAR RECOGNITION OF R-STATES AND T-STATES OF HUMAN ADULT HEMOGLOBIN BY A PARAMAGNETIC GD(III) COMPLEX BY MEANS OF THE MEASUREMENT OF SOLVENT WATER PROTON RELAXATION RATE. *Journal of the American Chemical Society* 117 (36):9365-9366.

Aime, S., M. Botta, S. G. Crich, G. B. Giovenzana, R. Pagliarin, M. Piccinini, M. Sisti, and E. Terreno. 1997. Towards MRI contrast agents of improved efficacy. NMR relaxometric investigations of the binding interaction to HSA of a novel heptadentate macrocyclic triphosphonate Gd(III)-complex. *Journal of Biological Inorganic Chemistry* 2 (4):470-479.

Bloembergen, N., and L. O. Morgan. 1961. PROTON RELAXATION TIMES IN PARAMAGNETIC SOLUTIONS EFFECTS OF ELECTRON SPIN RELAXATION. *Journal of Chemical Physics* 34 (3):842-&.

Botta, M. 2000. Second coordination sphere water molecules and relaxivity of gadolinium(III) complexes: Implications for MRI contrast agents. *European Journal of Inorganic Chemistry* (3):399-407.

Bottrill, Melanie, Lilian Kwok Nicholas, and Nicholas J. Long. 2006. Lanthanides in magnetic resonance imaging. *Chemical Society Reviews* 35 (6):557-571.

Brateman, P. S., Z. P. Xu, and F. Yarberry. 2004. *Handbook of Layered Materials*. Edited by S. M. Auerbach, K. A. Carrado and P. K. Dutta. New York: Marcel Dekker Inc.

Bydder, G. M., R. E. Steiner, D. J. Thomas, J. Marshall, D. J. Gilderdale, and I. R. Young. 1983. NUCLEAR MAGNETIC-RESONANCE IMAGING OF THE POSTERIOR-FOSSA - 50 CASES. *Clinical Radiology* 34 (2):173-188.

Caravan, P. 2006. Strategies for increasing the sensitivity of gadolinium based MRI contrast agents. *Chemical Society Reviews* 35 (6):512-523.

Caravan, P., J. J. Ellison, T. J. McMurry, and R. B. Lauffer. 1999. Gadolinium(III) chelates as MRI contrast agents: Structure, dynamics, and applications. *Chemical*

Reviews 99 (9):2293-2352.

Caravan, P., M. T. Greenfield, X. D. Li, and A. D. Sherry. 2001. The Gd3+ complex of a fatty acid analogue of DOTP binds to multiple albumin sites with variable water relaxivities. *Inorganic Chemistry* 40 (26):6580-6587.

Cavani, F., F. Trifiro, and A. Vaccari. 1991. HYDROTALCITE-TYPE ANIONIC CLAYS: PREPARATION, PROPERTIES AND APPLICATIONS. *Catalysis Today* 11 (2):173-301.

Carr, D. H., J. Brown, G. M. Bydder, H. J. Weinmann, U. Speck, D. J. Thomas, and I. R. Young. 1984. INTRAVENOUS CHELATED GADOLINIUM AS A CONTRAST AGENT IN NMR IMAGING OF CEREBRAL-TUMORS. *Lancet* 1 (8375):484-486

Damadian, R. 1971. TUMOR DETECTION BY NUCLEAR MAGNETIC RESONANCE. *Science* 171 (3976):1151-&.

Dupuis, J., J. P. Battut, Z. Fawal, H. Hajjimohamad, A. Deroy, and J. P. Besse. 1990. NUCLEAR-MAGNETIC-RESONANCE ANALYSIS OF PROTONS IN THE HYDROTALCITE TYPE COMPOUND ZN2/3AL1/3(OH)2CL1/3.N(H2O). *Solid State Ionics* 42 (3-4):251-255.

Ersoy, H., and F. J. Rybicki. 2007. Biochemical safety profiles of gadolinium-based extracellular contrast agents and nephrogenic systemic fibrosis. *Journal of Magnetic Resonance Imaging* 26 (5):1190-1197.

FREED, JH. 1978. DYNAMIC EFFECTS OF PAIR CORRELATION-FUNCTIONS ON SPIN RELAXATION BY TRANSLATIONAL DIFFUSION IN LIQUIDS .2. FINITE JUMPS AND INDEPENDENT T1 PROCESSES. *Journal of Chemical Physics* 68 (9):4034-4037.

Gore, J. C. 1985. PHYSICAL FACTORS IN THE DESIGN OF CONTRAST AGENTS FOR MRI. *Ieee Engineering in Medicine and Biology Magazine* 4 (3):39-42.

Hinshaw, W. S., P. A. Bottomley, and G. N. Holland. 1977. RADIOGRAPHIC THIN-SECTION IMAGE OF HUMAN WRIST BY NUCLEAR MAGNETIC-RESONANCE. *Nature* 270 (5639):722-723.

HWANG, LP, and JH FREED. 1975. DYNAMIC EFFECTS OF PAIR CORRELATION-FUNCTIONS ON SPIN RELAXATION BY TRANSLATIONAL DIFFUSION IN LIQUIDS. *Journal of Chemical Physics* 63 (9):4017-4025.

Kwak, S. Y., Y. J. Jeong, J. S. Park, and J. H. Choy. 2002. Bio-LDH nanohybrid for gene therapy. *Solid State Ionics* 151 (1-4):229-234.

Lauffer, R. B. 1987. PARAMAGNETIC METAL-COMPLEXES AS WATER PROTON RELAXATION AGENTS FOR NMR IMAGING - THEORY AND DESIGN. *Chemical Reviews* 87 (5):901-927.

Lauterbur, P. C. 1973. IMAGE FORMATION BY INDUCED LOCAL INTERACTIONS - EXAMPLES EMPLOYING NUCLEAR MAGNETIC-RESONANCE. *Nature* 242 (5394):190-191.

Lee, J. H., Y. M. Huh, Y. Jun, J. Seo, J. Jang, H. T. Song, S. Kim, E. J. Cho, H. G. Yoon, J. S. Suh, and J. Cheon. 2007. Artificially engineered magnetic nanoparticles for ultra-sensitive molecular imaging. *Nature Medicine* 13 (1):95-99.

Li, A., L. L. Qin, W. R. Wang, R. R. Zhu, Y. C. Yu, H. Liu, and S. L. Wang. 2011. The use of layered double hydroxides as DNA vaccine delivery vector for enhancement of anti-melanoma immune response. *Biomaterials* 32 (2):469-477.

Liang, Zhi-Pei, and Paul C. Lauterbur. 2000. *Principles of Magnetic Resonance Imaging*. New York: IEEE Press.

Micskei, K., L. Helm, E. Brucher, and A. E. Merbach. 1993. O-17 NMR-STUDY OF WATER EXCHANGE ON GD(DTPA)(H2O) 2- AND GD(DOTA)(H2O) - RELATED TO NMR IMAGING. *Inorganic Chemistry* 32 (18):3844-3850.

Morgan, Christopher J., and William R. Hendee. 1984. *Introduction to Magnetic Resonance Imaging*. Missouri: Multi-Media Publishing Inc.

Nakamura, H., N. Ito, F. Kotake, Y. Mizokami, and T. Matsuoka. 2000. Tumor-detecting capacity and clinical usefulness of SPIO-MRI in patients with hepatocellular carcinoma. *Journal of Gastroenterology* 35 (11):849-855.

Oh, Jae-Min, Timothy T. Biswick, and Jin-Ho Choy. 2009. Layered nanomaterials for green materials. *Journal of Materials Chemistry* 19 (17):2553-2563.

Oksendal, A. N., and P. A. Hals. 1993. BIODISTRIBUTION AND TOXICITY OF MR IMAGING CONTRAST-MEDIA. *Jmri-Journal of Magnetic Resonance Imaging* 3 (1):157-165.

Powell, D. H., O. M. NiDhubhghaill, D. Pubanz, L. Helm, Y. S. Lebedev, W. Schlaepfer, and A. E. Merbach. 1996. Structural and dynamic parameters obtained from O-17 NMR, EPR, and NMRD studies of monomeric and dimeric Gd3+ complexes of interest in magnetic resonance imaging: An integrated and theoretically self consistent approach. *Journal of the American Chemical Society* 118 (39):9333-9346.

Qin, L. L., M. Xue, W. R. Wang, R. R. Zhu, S. L. Wang, J. Sun, R. Zhang, and X. Y. Sun. 2010. The in vitro and in vivo anti-tumor effect of layered double hydroxides nanoparticles as delivery for podophyllotoxin. *International Journal of Pharmaceutics* 388 (1-2):223-230.

Rives, V., and M. A. Ulibarri. 1999. Layered double hydroxides (LDH) intercalated with metal coordination compounds and oxometalates. *Coordination Chemistry Reviews* 181:61-120.

Sijbers, J., P. Scheunders, N. Bonnet, D. VanDyck, and E. Raman. 1996. Quantification and improvement of the signal-to-noise ratio in a magnetic resonance image acquisition procedure. *Magnetic Resonance Imaging* 14 (10):1157-1163.

Silion, M., D. Hritcu, I. M. Jaba, B. Tamba, D. Ionescu, O. C. Mungiu, and I. M. Popa. 2010. In vitro and in vivo behavior of ketoprofen intercalated into layered double hydroxides. *Journal of Materials Science-Materials in Medicine* 21 (11):3009-3018.

Solomon, I. 1955. RELAXATION PROCESSES IN A SYSTEM OF 2 SPINS. *Physical Review* 99 (2):559-565.

Swift, T. J., G. M. Anderson, R. E. Connick, and M. Yoshimine. 1964. CORRECTION. *Journal of Chemical Physics* 41 (8):2553-&.

Swift, T. J., and R. E. Connick. 1962. NMR-RELAXATION MECHANISMS OF 017 IN AQUEOUS SOLUTIONS OF PARAMAGNETIC CATIONS AND LIFETIME OF WATER MOLECULES IN FIRST COORDINATION SPHERE. *Journal of Chemical Physics* 37 (2):307-&.

CHAPTER 3

NMR STUDY OF CEMENTITIOUS MATERIALS

3.1 Introduction

3.1.1 Cementitious Materials

Ordinary Portland Cement (OPC) is one of the most widely used construction materials in the world. It is an important ingredient of concrete, usually taking up 10-15% of that material(Taylor 1990). Cement has been used for construction for thousands of years and has become more and more important in the development of civilization. The production of cement has already increased to an enormous figure all over the world. 3700 million tons of cement were produced in 2012 worldwide(Hargreaves 2013).

Portland cement is a complicated mixture produced by calcination of blends of limestone and clays. So Portland cement usually has high a content of calcium oxide (~60%) and a moderate amount of silica (~20%). In anhydrous cement, the main components are tricalcium silicate and dicalcium silicate. With hydration, parts of these components are dissolved and form disordered products, like calcium-silicate-hydrate(C-S-H)(Skibsted and Hall 2008).

It takes 5.8 billion Joules to produce one ton of cement. With this huge production, cement becomes the third most energy-intensive consumer industry after steel and aluminum in the world(Price and Worrell 1999). What is more serious is that the cement industry is one of the primary industries responsible for the greenhouse gas emissions. Lime calcination and fuel burning in cement production are both CO_2 emission processes. About 900kg of CO_2 are emitted for every ton of cement produced, about 50% from the chemical processing and 40% from fuel burning(Carbon Dioxide Emissions 2006; Benhelal et al. 2013).

Because of these problems induced by the cement industry, researchers have been searching over the years for cement replacements. At present, three cement substitutes are most commonly used: fly ash, ground granulated blast-furnace slag (abbreviated ggbs) and condensed silica fume (csf). There are several features of these cement substitutes. First, they are industrial waste or by-products, so there is almost no raw material cost. Second, these materials have high silicate content and can thus participate in reaction to form silicate-based network structures, which is the key to OPC's functionality.(Palomo and Palacios 2003; Palomo and de la Fuente 2003)

3.1.2 Alkali-activated fly ash

Fly ash consists of residues generated in coal combustion, usually removed from the flue gases using electrostatic precipitators. Since most power plants use coal-like fuel all over the world, the sources of fly ash are sufficient. Replacement of cement by fly ash not only reduces the problem of the cement industry, but also helps recycle fly ash.

However, in order to function as a binder fly ash must be subjected to a chemical process known as activation, nearly always performed by mixing fly ash with an alkaline solution and curing at high temperature(Puertas et al. 2000; Bakharev 2005). Mixed with water and allowed to dry, the final product has hardness comparable to that of OPC, making its use as a cement replacement possible(Duxson, Fernandez-Jimenez, et al. 2007; Palomo, Grutzeck, and Blanco 1999). Compared with cement, fly ash has a much lower calcium oxide content and much higher alumina content, so the reaction and final product are different from cement's(Palomo, Alonso, and Femandez-Jimenez 2004). The main reaction product in alkali activated fly ashes is a three-dimensional alkaline aluminosilicate hydrate network, commonly referred as the M-A-S-H gel (where M is the alkali cation - Na or K). The reaction starts from the dissolution of silicate and aluminate on the surface of fly ash particles, which is rapid at high pH(Blum and Lasaga 1988; Walther 1996). Concentration of silicate and aluminate rapidly increase, thereby inducing the formation of gels(Swaddle, Salerno, and Tregloan 1994; Swaddle 2001). With further reorganization and polymerization, the final reaction product will form a 3D aluminosilicate network. Thermal cure is required for this reaction to acquire adequate properties as a binder.

With soluble silicate present, silicate glass slurries could also be formed by removing water. But the product would be dissolved again by water(Duxson, Fernandez-Jimenez, et al. 2007). A geopolymer, as aluminosilicate newwork formers are known, with irreversible hardness can be formed only when the silicate and aluminate are in contact, during final curing into a structure. Thus, soluble aluminum is a kind of trigger for inducing hardness in the final product.

In the network, both the Si^{4+} and Al^{3+} cation are tetrahedrally coordinated and linked by oxygen. The alkali cation plays a charge balancing role for AlO_4^- group. The alkali cation is thus an essential structure-forming element and influences the Si/Al ratio of the final reaction product. Also, a Na/Al ratio of approximately 1.0 is required for desirable mechanical and durability properties of these matrices(Duxson, Mallicoat, et al. 2007).

Alkalinity of the activator determines the extent of its dissolution into the binder. It has been reported that potassium-based activating solutions, by virtue of their higher pH, aid in more dissolution and that K is preferentially incorporated into the binder structure(Duxson et al. 2005). The tendency of K^+ to favor larger silicate oligomer formation is stated to be influential, in the presence of activating solutions with higher silicate contents(McCormick, Bell, and Radke 1989). However other studies have reported better efficiency of sodium based activators both in liberating Si and Al species into solution and in the rates of crystallization(Rios, Williams, and Roberts 2009; van Jaarsveld and van Deventer 1999; Xu and van Deventer 2003).

Extra soluble silica in the activator also affects the process of activation(Palomo, Alonso, and Femandez-Jimenez 2004; Lee and van Deventer 2002). With extra soluble silica, the alkalinity of the activator will be lowered, therefore the rate of dissolution will be decreased. However, the presence of more soluble silica could favor the formation of a silica-rich gel. So fly ash activated by alkali silicate solution must also be examined.

3.1.3 NMR Study of Zeolites

Zeolites are a widely-used group of aluminosilicate minerals that have microporous structures. These minerals lose water rapidly under thermal treating, without lattice collapse, which looks like “boiling”. So this group of minerals is named as zeolites. They include molecular sieves, among other common materials. Activated fly ash is also considered as a “zeolite precursor”, so the structures of zeolites help in understanding those of activated fly ash(MCCORMICK and BELL 1989).

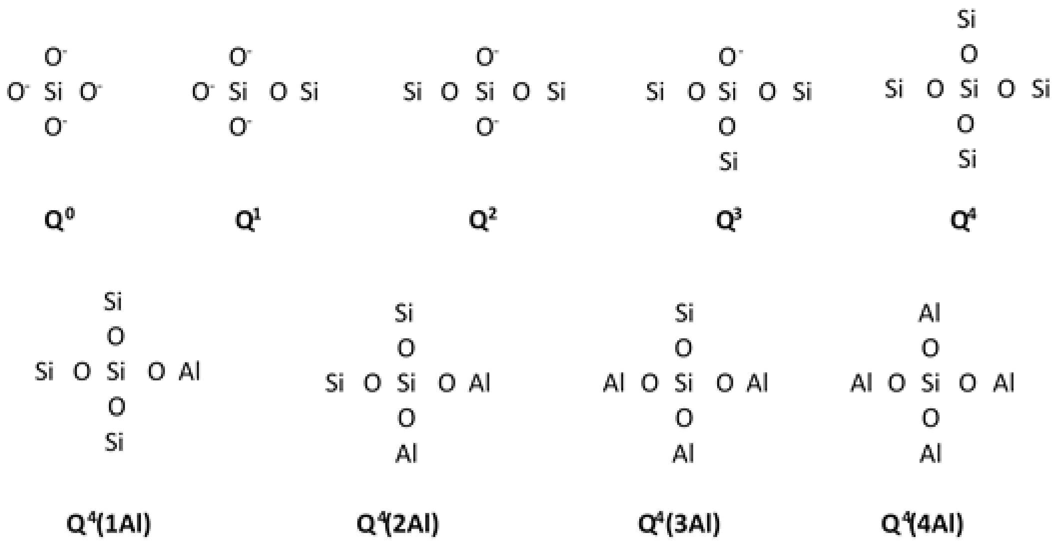

Figure 3.1: Sketch of structure with different denotation of Si(Engelhardt and Michel 1987)

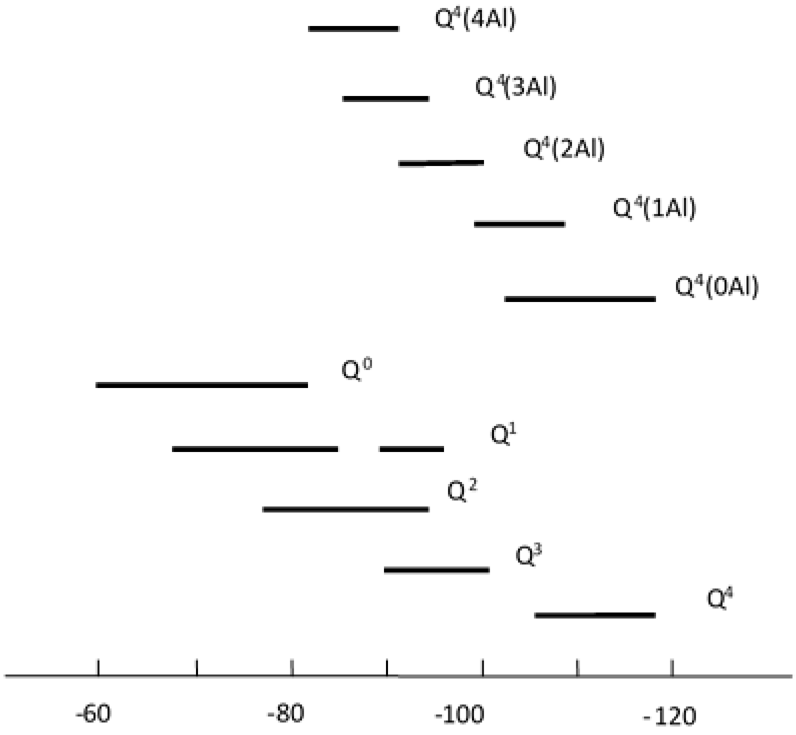

Figure 3.2: ^{29}Si chemical shift range of different species reference to TMS(Mackenzie and Smith 2002)

With the development of solid-state NMR, an extremely useful tool for investigating the structure and interactions of solid materials became available. ^{29}Si and ^{27}Al soli-state NMR are invaluable methods for the study of aluminosilicate, in particular zeolites(Engelhardt and Michel 1987). The chemical shifts, line intensities and line widths of NMR spectra reveal much about the structure of these materials.

In a zeolite, the Si atoms are usually 4 coordinated through oxygen atoms and denoted as Q^n. Here Q represents a silicon atom singly bonded to four oxygen atoms and the superscript n represent the number of other Q units bonded via the unpaired oxygen electrons (Figure 3.1)(Engelhardt et al. 1974). In aluminosilicate minerals, the Si atom in these structures can be replaced by an Al atom, thereby forming a tetrahedral AlO_4 unit in the SiO_4-bonded network. In this case, the notation Q^n(mAl) is used, where m represent the number of Al atoms in nearest-neighbor bonded Q units replacing Si ($m \leq n$). In cementitious materials, materials with high content of Ca^{2+} ion, like Portland cement and slag, tend to form a chain structure, so the Si atoms are mostly Q^1 (end of chain) and Q^2 (middle of chain)(Skibsted and Hall 2008), although small amounts of Q^3 and Q^4 (cross-linked) can also be observed by NMR in slag(Myers et al. 2013). However materials with low content of Ca^{2+} ion, like fly ash and metakaolin, tend to form 3D aluminosilicate gels, in which Si atoms are mainly in Q^4 groups, with a few AlO_4 neighbors(Fernandez-Jimenez, Palomo, and Criado 2005).

The chemical shifts of ^{29}Si observed in an NMR spectrum are usually located in the range -60ppm to -120ppm, relative to tetramethylsilane (TMS) (Figure 3.2). Q^0, in isolated SiO_4^{4-}

ions, usually has the highest ^{29}Si chemical shift, and the shift decreases by about 10ppm with each Si-O-Si bond formed in a structure. Also, with each Si that is replaced by Al, the chemical shift of ^{29}Si increases by about 5ppm(Balmer et al. 1997). For NMR spectral interpretation these shift change patterns are understood as results of electron density changes in the vicinity of the observed ^{29}Si nucleus itself, arising from chemical bonding. In addition, the integrals of different NMR lines (or intensities if line widths are identical) are proportional to the total amounts of Si atoms at their corresponding sites. In aluminosilicate, the Si/Al ratio can also be calculated from the identified Si species and their intensities using the equation(Engelhardt and Michel 1987):

$$Si/Al = \frac{\sum_{m} I(Q^4(mAl))}{0.25\sum_{n} mI(Q^4(mAl))} \tag{3.1}$$

Here $I(Q^4(mAl))$ is the NMR signal intensity of Q^4(mAl).

Line widths of ^{29}Si in spectra are frequently affected by ^{1}H, ^{27}Al or other neighboring nuclei, and thus do not always turn out to be identical, but they can also provide information about structural disorder.

As for ^{27}Al NMR of the Al atoms, they could be in 4, 5 or 6 O-coordinated sites in zeolites. The chemical shifts of Al are in the range of 50 to 80ppm for 4-coordinate, 30 to 40ppm for 5-coordinate and -10 to 20ppm for 6-coordinate(LIPPMAA, SAMOSON, and MAGI 1986; Muller et al. 1981). According to Loewenstein’s rule(Loewenstein 1954), there is no Al-O-Al bonding in aluminosilicate network. So the possibility of Al-O-Al bonding is usually neglected, although a few exceptions are exist. In another word, each tetrahedral

Al atom must bond to four other four Si atoms, reducing the chemical shift range of 4-coordinate Al from 55 to 68ppm(Stade, Muller, and Scheler 1984). Because of the quadrupolar interaction of ^{27}Al, quantitative analysis of its line intensity cannot be done in most amorphous materials(Dejong, Schramm, and Parziale 1983).

Usually zeolite NMR spectra have well defined peaks and the species are easier to determine because of structures' long range crystalline order. However, cementitious materials have more complicated spectral components and lack long range order, so poorly defined peaks occur. In these cases ^{29}Si NMR spectra of zeolites of similar composition can be used reference to identify the components of a cementitious material(Lippmaa et al. 1980; Neuhoff, Stebbins, and Bird 2003; Madani et al. 1990; Kato and Nishido 2003).

Table 3.1: ^{29}Si chemical shifts of several types of zeolites.

Zeolite	Formula	^{29}Si chemical shift(ppm)				
		Q^4(4Al)	Q^4(3Al)	Q^4(2Al)	Q^4(1Al)	Q^4(0Al)
Na chabazite	$NaAlSi_2O_6 \cdot 3H_2O$	-88.6	-93.2	-98.5	-104.2	-109.7
NaP zeolite	$Na_2Al_3Si_5O_{16} \cdot 6H_2O$	-88	-92	-97	-102	-107
Na phillipsite	$Na_{0.9}Ca_{0.5}K_{0.6}Si_{5.2}Al_{2.8}O_{16} \cdot 6H_2O$	-87.5	-92.0	-98.0	-103.5	-108.0
Orthoclase	$KAlSi_3O_8$	-86.7	-92.6	-96.8	-100.2	-104.6

3.2 Experimental Section

3.2.1 Sample Preparation

A Class F Fly ash conforming to ASTM C 618(2012) was used as the starting material. The chemical composition of fly ash is shown in Table 3.1. The specific surface area of the fly ash was measured at 218m^2/kg using Blaine's air permeability apparatus. The median particle size, measured using laser particle size analysis was 19.9mm.

Table 3.2: Chemical composition and physical properties of fly ash

SiO_2	Al_2O_3	Fe_2O_3	CaO	MgO	SO_3	Na_2O	K_2O	LOI	SSA
58.4%	23.8%	4.19%	1.11%	0.44%	1.43%	1.02%	1.02%	0.5%	218m^2/kg

Fly ash was activated using alkali hydroxide solutions of two different concentrations (4M and 8M NaOH and KOH) and alkali silicates (both K and Na silicates) having a SiO_2-to-Na_2O or SiO_2-to-K_2O ratio (M_s) of 2.0. The alkali hydroxide solutions were prepared by dissolving NaOH or KOH beads (99.9% purity) in water. The Na and K silicate solutions had as-obtained M_s values (mole-based) of 3.32 and 3.29 respectively and a solids content of about 36%. NaOH or KOH solutions were added to bring the M_s values to 2.0 and maintain the M_2O-to total powder (fly ash) content (n) of the pastes at 0.05. The solution-to-powder ratio used for all the mixtures in this study was 0.40. For rheological studies of NaOH and KOH activated pastes alone, the solution-to-powder ratio used was 0.35. This change was necessitated by the requirement to obtain consistent pastes that could be placed and confined within the parallel plates of the rheometer used. Mortars containing 50% by volume of paste (activator + binder) were prepared for the compressive strength tests. All the paste and mortar specimens were cured in ambient conditions at 23±1^{o}C for 24h and then heat cured in sealed conditions at 80^{o}C for a further 60h. One set of mortar specimens was cured in a waterbath maintained at 80^{o}C. Compressive strength tests were conducted on both sets of specimens. Porosity and NMR test were only conducted on the set of specimens in sealed conditions.

3.2.2 Compressive strength

The compressive strengths of the mortar mixtures were determined in accordance with ASTM C 109(Ben Haha et al. 2011). The tests were conducted after the specimens were removed from the oven or waterbath after the thermal curing duration of 60h. The specimens kept in the waterbath were surface dried before testing. Both sets of specimens were allowed to return to ambient temperatures before they were tested.

3.2.3 Pore Structure

Mercury intrusion porosimetry (MIP) was used to detect the pore structure of activated fly ash. In this test, the sample was merged in mercury and pressure was applied on the container. The mercury can be intruded into pore with small sizes under high pressure. From Washburn equation, the pore size can be calculated from the applied pressure(Washburn 1921).

$$D = -4\gamma \cos\theta / P \tag{3.2}$$

Where D is the diameter of pore size; γ is the surface tension of mercury; θ is the contact angle of mercury and P is the pressure applied.

The contact angle and surface tension used were 130^o and 0.485N/m. The maximum pressure was 414 MPa corresponding to a minimum pore diameter of 0.003μm.

3.2.4 NMR Spectroscopy

^{29}Si, ^{27}Al, ^{1}H and ^{23}Na Magic Angle Spinning (MAS) NMR spectroscopy were performed using a Varian CMX300 solid-state NMR spectrometer. For ^{29}Si NMR, the resonance frequency was 59.7MHz. The time between accumulations was 5s, and tetramethylsilane

(TMS) was used as the external standard for ^{29}Si. The resonance frequency for ^{27}Al was 78.3 MHz. The ^{27}Al chemical shift values were referenced to 1% $Al(NO_3)_3(aq)$. The times between accumulations are the same for ^{27}Al (1s). For ^{1}H NMR, the frequency was 300.4MHz and 1s the pulse delay time. TMS is also used as the reference for ^{1}H NMR. All the spectrum were obtained with MAS spinning rate set at 10kHz.

A $\pi/2$ r.f. pulse was used for spectra of ^{29}Si and ^{1}H. A $\pi/6$-duration r.f. pulse length (for aqueous metal ion (Al^{3+}) in octahedral coordination in solutions) was used for ^{27}Al. The ^{27}Al nucleus has a substantial electric quadrupole moment, and it determine the NMR spectra in solids whose local environment for the metal ion has symmetry lower than cubic. All samples in this study are basically amorphous, and therefore have low symmetry for an Al atom (despite its highly local four-fold oxygen coordination, at the center of an Al-O ion).

3.3 Results and Discussion

3.3.1 Compressive strength

Figure 3.3 shows the compressive strength of the activated fly ash samples. For all the cases, the compressive strength of the specimens cured in a water bath is lower than that of specimens cured under sealed conditions in a convection oven. The specimens were cured at ambient conditions (23^{o}C) for 24h before the water bath. However, the fly ash can't be reacted enough under ambient conditions, so the specimens were exposed to the water bath at 80^{o}C, allowing water to penetrate into the material's microstructure even while the structure was being formed, resulting in an increased porosity and lower strength.

With sealed curing there is no extra water, resulting in lower porosity and higher strength. While soluble silica expedites the precipitation of the sample's gel, the reaction progresses further before heat curing. So the strengths of samples using an alkali silicate activator with two heat curing are close to those formed.

The compressive strengths of the Na-activated mortars are found to be higher than those of the K-activated mortars irrespective of the activator type, concentration, or the curing regime. This is quite the opposite of the trends reported in several previous paper(van Jaarsveld and van Deventer 1999; Lizcano et al. 2012) and to the fact that K based activators result in better workability with less viscosity, which likely increases the ease of ionic movement during the structure formation phase. Potassium has been found to promote a greater degree of reaction and thus increased reaction product formation in metakaolin based systems.

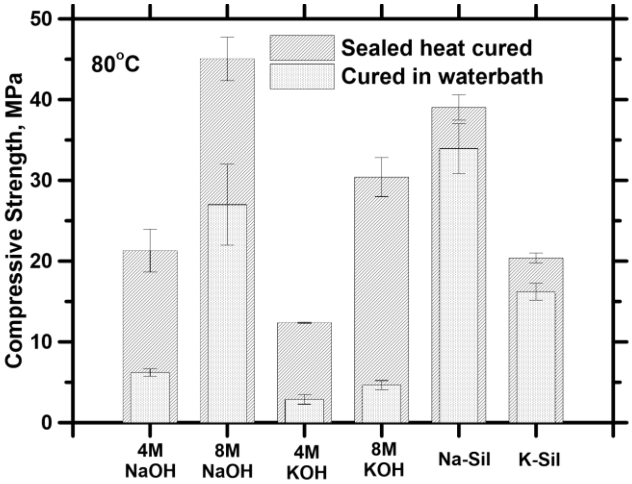

Figure 3.3: Compressive strength of activated mortars after sealed curing or moist curing for 60h on a waterbath. Curing temperature were 80^{o}C for both cases

The higher concentration of hydroxide activator is apparently beneficial to the strength of final product. Higher concentration of hydroxide leads to rapid dissolution of silicate and alumina even at ambient temperature, therefore faster formation of the gel. Thus 8MNaOH activated fly ash cured in the water bath has a relatively high strength. Also, more alkali cation will affect the Si/Al ratio in the product, and therefore the sample's mechanical properties.

3.3.2 Pore Structure

Figure 3.4 shows the total pore volume and the differential pore volume plotted as a function of pore sizes for the activated fly ash using six different activators with sealed curing. Comparing K-activation with Na-activation, the cumulative volumes of mercury intruded are very similar. Increasing the concentration of activator (from 4M to 8M), causes both the cumulative volumes and critical pore sizes (indicated by the peak in the differential pore volume-pore size relationship) to decrease, for both K-activator and Na-activator. With a higher degree of alkalinity, more Si and Al could be dissolved and more aluminosilicate gel formatted. That leads to a more packed structure, which is the possible reason for less cumulative volume resulting in a higher level of alkalinity.

Activated fly ash using alkali silicate has higher cumulative volumes than that using alkali hydroxide. The critical pore size of activated fly ash using alkali silicate is much smaller than that using alkali hydroxide. The extra soluble silicate in the activator accelerate the formation of the gel, so the structure tends to form smaller size pores. However, the alkalinity of alkali silicate solutions is lower, so fly ash particles are less dense, resulting

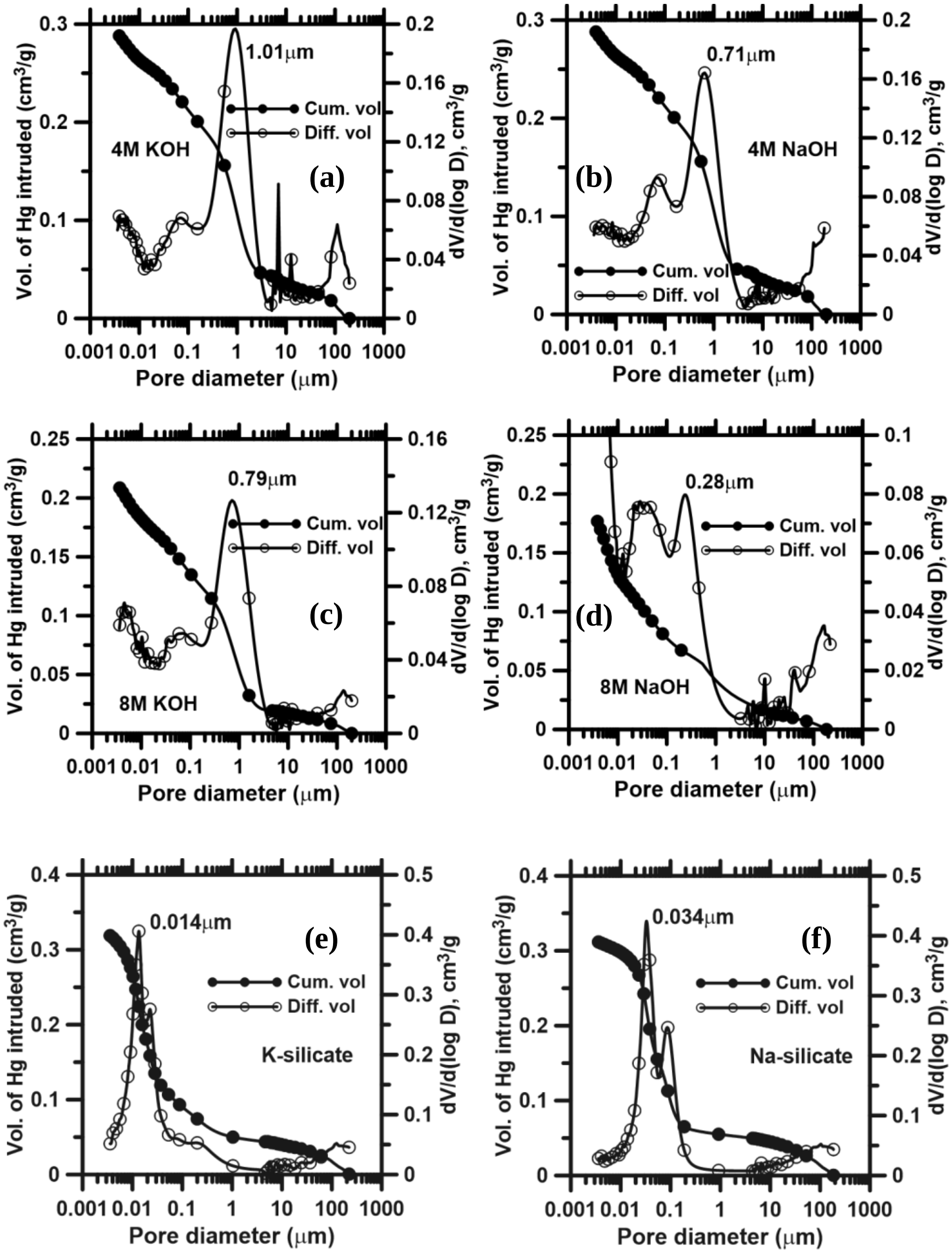

Figure 3.4: Pore size – cumulative/differential volume curves for: (a) 4M KOH; (b) 4M NaOH; (c) 8M KOH; (d) 8M NaOH; (e) K-silicate and (f) Na-silicate activated fly ash pastes

in more accumulation volume of pores.

Based on the IUPAC definition(ROUQUEROL et al. 1994), mesopores have sizes in the range of 2-50nm and macropores have size larger than 50nm. Pores with size larger than 200nm are present in low reactivity fly ash(Sindhunata et al. 2006), so the pores can be classified into three size groups: 0.0036-0.05μm, 0.05-0.2μm and >0.2μm (0.0036μm is the MIP detection limit). The 0.05-0.2μm sized macropores are formed at an early stage of reaction, and as products get formed these pores would be filled up and mesopores (0.0036-0.05μm) are formed, which represent the pores in clusters of aluminosilicate network. The pores larger than 0.2μm can be attributed to the spaces between the reaction products, which detrimentally influences the strength of activated fly ash (Figure 3.5(b)).

Figure 3.5(a) shows the portion of pores in three size ranges. The activated fly ash using 4M KOH or NaOH have a high portion of pores with size larger than 0.2μm, which is responsible for the low compressive strength. The high portion of mesopores in Na and K

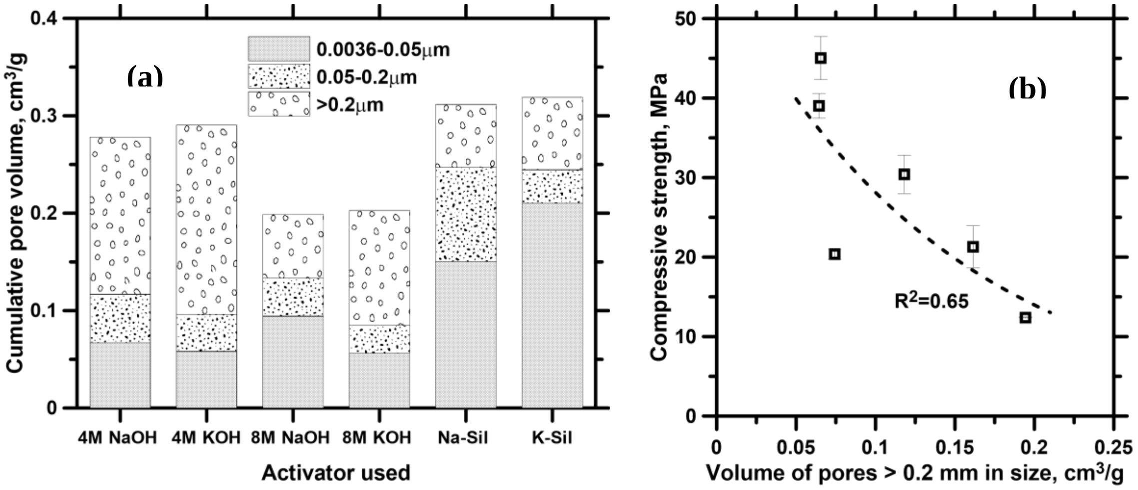

Figure 3.5: (a) Distribution of pore volume into different size ranges in activated fly ash pastes; and (b) Relationship between compressive strength and the volume of

silicate specimens means more aluminosilicate gel was formed, which is a benefit resulting from soluble silicate in the activator. However, the high porosity reduces the strength relative to 8M NaOH specimens.

3.3.3 ^{29}Si MAS NMR Spectra

Figure 3.6 shows the ^{29}Si NMR spectrum of the initial fly ash. A Lorentz line shape was used for deconvolution into multiple peaks of well-known silicate compounds, each peak being assigned the same line width, following the working first approximation for ^{29}Si line decomposition in the cements literature. The spectrum is poorly defined because of the amorphous structure in the initial fly ash. The peak at around 90ppm can be attributed to crystalline mullite, a strongly bound, non-reactive silica-alumina compound frequently found in fly ash(Gomes and Francois 2000), while the peaks lower than -109ppm belong

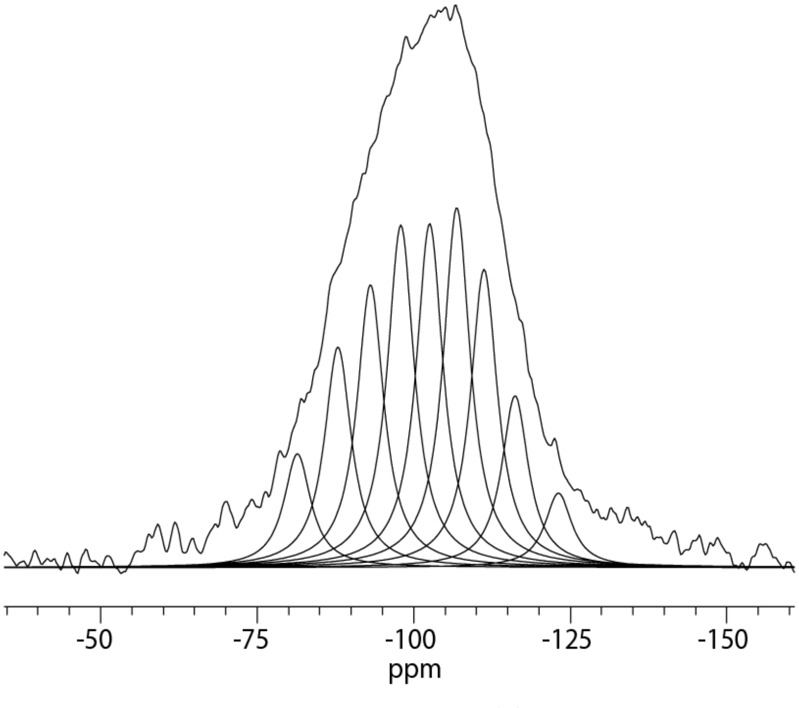

Figure 3.6: 29Si MAS NMR spectrum of fly ash and its deconvolution

to the silica species in the fly ash that react with alkali to form the aluminosilicate network. Figure 3.7 shows the ^{29}Si MAS NMR spectra of activated fly ash using six different activators. Fly ash activated using NaOH (Figure. 7(a) and (b)) shows some well-defined peaks, which arise from different aluminosilicate Si species. The highest peak is located at -98ppm, which is characterized as Q^4(2Al). When the NaOH concentration of the activator increase from 4M to 8M, the amount of Al-rich gel (Q^4(4Al)+Q^4(3Al)) changes very little from its initial value (~36%), but the amount of Si-rich gel (Q^4(2Al)+Q^4(1Al)) increase substantially (from 36% to 40%). Higher alkalinity releases more Si and Al from fly ash, therefore forming more gel. The higher content of aluminosilicate gel in 8M NaOH is consistent with the higher compressive strength of the 8M NaOH specimen.

The NMR spectrum of the Na silicate-activated fly ash (Figure 3.7(c)) is broad with poorly defined peaks, reflecting the higher degree of structural disorder in the gel. Comparing Na silicate specimens with those formed using NaOH, one sees that they have similar chemical shifts of Si species in the aluminosilicate gel, which means the products have similar structures. However, in the Na silicate specimen, there are more component below -109ppm, which are silica polymorphs. There is extra silicate in the activator and thus relatively less aluminate in the resulting binder, which is consistent with more silica polymorphs being formed instead of aluminosilicate. The Na silicate specimens have the highest degree of disorder and lowest portions of aluminosilicate gel in the final product, among Na activator specimens. The Na silicates also have lower alkalinity, so less silicate and aluminate can be dissolved. Thus there is more unactivated fly ash left, which is

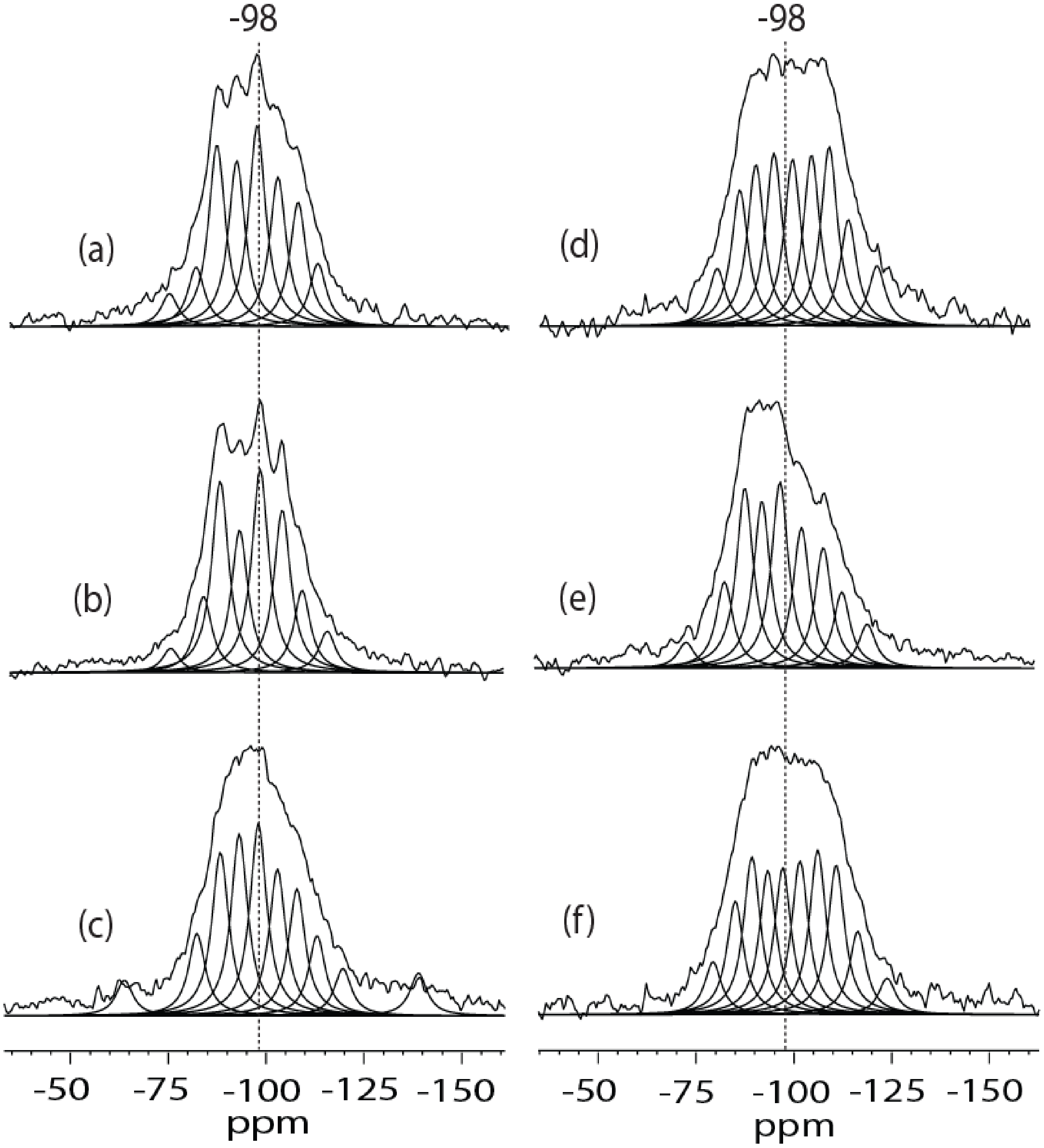

Figure 3.7: ^{29}Si MAS NMR spectra of fly ash activated using: (a) 4M NaOH; (b) 8M NaOH; (c) Na silicate; (d) 4M KOH; (e) 8M KOH; (f) K silicate.

Table 3.3: Deconvolution of activated fly ash

Sample						Aluminosilicate gel				Silica polymorphs			Si/Al
			Q^1, Q^2		Q^4(4Al)	Q^4(3Al)	Q^4(2Al)	Q^4(1Al)	Q^4(0Al)				
4MNaOH	δ(ppm)		-75.3	-82.1	-87.5	-92.5	-97.7	-103	-108.2	-113.2			1.85
	Integral%		3.4	6.1	18.6	17.0	20.6	15.3	12.7	6.5			
8MNaOH	δ(ppm)		-75.6	-84	-88.2	-93.2	-98.4	-104.1	-109.1	-115.5			1.78
	Integral%		2.6	8.3	20.7	15.4	22.0	17.6	8.9	4.5			
4MKOH	δ(ppm)		-80.5	-86	-90.1	-94.7	-99.4	-104.3	-108.8	-113.7	-121.2		2.03
	Integral%		5.6	11.6	13.4	14.3	13.7	14.0	14.6	8.4	4.4		
8MKOH	δ(ppm)		-72.1	-81.9	-87.2	-91.5	-96.1	-101.6	-107.2	-111.9	-118.2		1.82
	Integral%		2.8	8.6	17.7	16.4	18.1	13.6	11.5	7.2	4.1		
Na-Sil	δ(ppm)	-63.53		-82	-88	-92.8	-97.7	-102.6	-107.6	-112.7	-119.3	-138.6	1.87
	Integral%	3.2		7.5	14.9	16.6	17.5	13.3	11.5	7.3	4.3	3.9	
K-Sil	δ(ppm)		-78.7	-84.6	-88.9	-92.9	-96.8	-101.2	-105.8	-110.4	-115.9	-123.3	2.02
	Integral%		4.8	9.7	13.4	12.1	12.4	12.8	13.6	12.2	6.5	2.6	

consistent with the high degree of disorder. However, with the extra soluble silicate in activator, the formation of aluminosilicate would be accelerated as long as aluminate was dissolved, which is in agreement with the relative high strength observed for these samples. Also, though considering that the portion of aluminosilicate gel is calculated from the total amount of Si, the extra Si atoms from the activator makes the proportion of aluminosilicate gel appear smaller.

Comparing Na activator with K activator specimens, the chemical shifts of the components show small changes, which indicate that differences in final product result from differences in the alkali cation type. The change of chemical shift is small, being only about 2ppm, which is consistent with changes induced by the presence of alkali cations in zeolites. Besides, the spectra of K activators have poorly defined peaks, implying a higher degree of disorder in the sample. K atoms have larger size than the Na atom, therefore lower migration ability of K, so the K activator specimen cannot rearrange their structural positions efficiently during reactions to lower energy states. Compared with Na activator specimens, K activated specimens have lower content of aluminosilicate gel (both Al rich

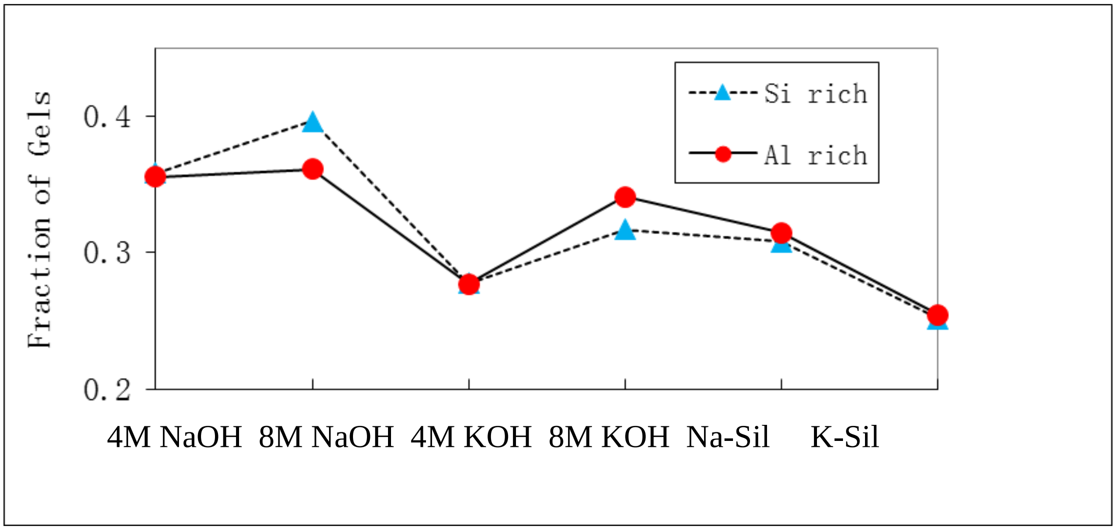

Figure 3.8: Fraction of Si rich gel and Al rich gel as a function of activator type

gel and Si rich gel), which means that less reaction product is are formed with the K activator. These factors can help explain the low strength of K activated fly ash.

When the concentration of KOH increase from 4M to 8M, the spectrum becomes narrow and both Al rich gel and Si rich gel increase. The increase of Al rich gel is more than that of Si rich gel, which means the 4M KOH activated fly ash is still in an early stage of reaction. Compared with the concentration increases seen for NaOH activator, the increase of Al rich gel is less than that of the Si rich gel, which corresponds to a later stage of reaction. The K silicate specimens have the broadest lines in the six spectra, because of the high degree of disorder induced by both K and the unactivated fly ash.

3.3.4 ^{1}H MAS NMR spectra

Condensation of the M-A-S-H gel releases water molecules, which migrate into the hydration spheres of the cation. The hydration sphere of Na^+ contains 5.7-5.8 water molecules whereas that of K^+ contains 6.9-7.0 molecules. So, in the K activator specimens, more waters are constrained in the small pores in the gel, which hinders further

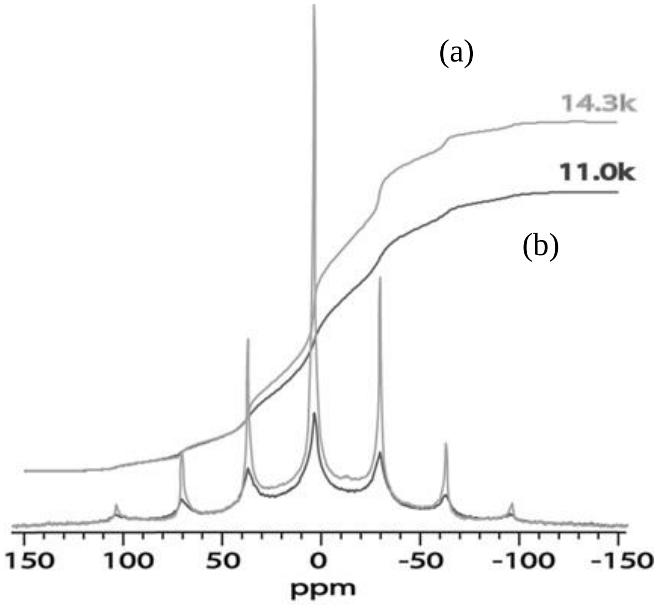

Figure 3.9: ^{1}H NMR spectra of activated fly ash using (a) 8M KOH; (b) 8M NaOH

polymerization. ^{1}H NMR spectra of 8M NaOH and KOH shown in Figure 3.9, both of which have a central peak around 4.8ppm, correspond to hydrogen in H_2O. The total spectrum integrals, which are proportional to the number of protons in the sample and normalized by the sample mass are also shown in Figure 3.9. The KOH activated specimen has approximately 30% more water than the NaOH activated specimen, which confirms that K tends to constrain more water, thereby affecting the polymerization process.

3.3.5 ^{27}Al MAS NMR Spectra

The ^{27}Al NMR spectra are shown in Figure 3.10. For the initial fly ash, the spectrum is composed of two broad lines at about 50ppm and 0ppm, which correspond to four and six coordinate Al with a high degree of disorder. Five coordinate Al may also exist in the initial fly ash, with its line obscured by the broad 50ppm line, so it is hard to distinguish. In activated fly ash, the common feature of ^{27}Al NMR spectra is that they have a relatively narrow line at 57ppm and a broad line at around 0ppm. The 57ppm line is four coordinate Al in activated fly ash and is narrower than that of the initial fly ash, representing the formation of a structure with lower degree of disorder, thus supporting the views of the dissolution and formation process in the activation of fly ash. The 0ppm line is six coordinate Al, from the undissolved fly ash. We can surmise approximately from the 0ppm line intensities that the specimens formed using silicate activators have more 0ppm residue, thus undissolved fly ash, than those formed using hydroxide activators. This phenomenon validates our surmise that alkali hydroxide activators have stronger dissolution ability in fly ash, because of high level of alkalinity. Also, the narrowest 57ppm line of the specimens in Figure 3.10, belonging to the 8M NaOH activated specimen, should represent the most highly ordered structure, which is consistent with our results from ^{29}Si NMR spectra.

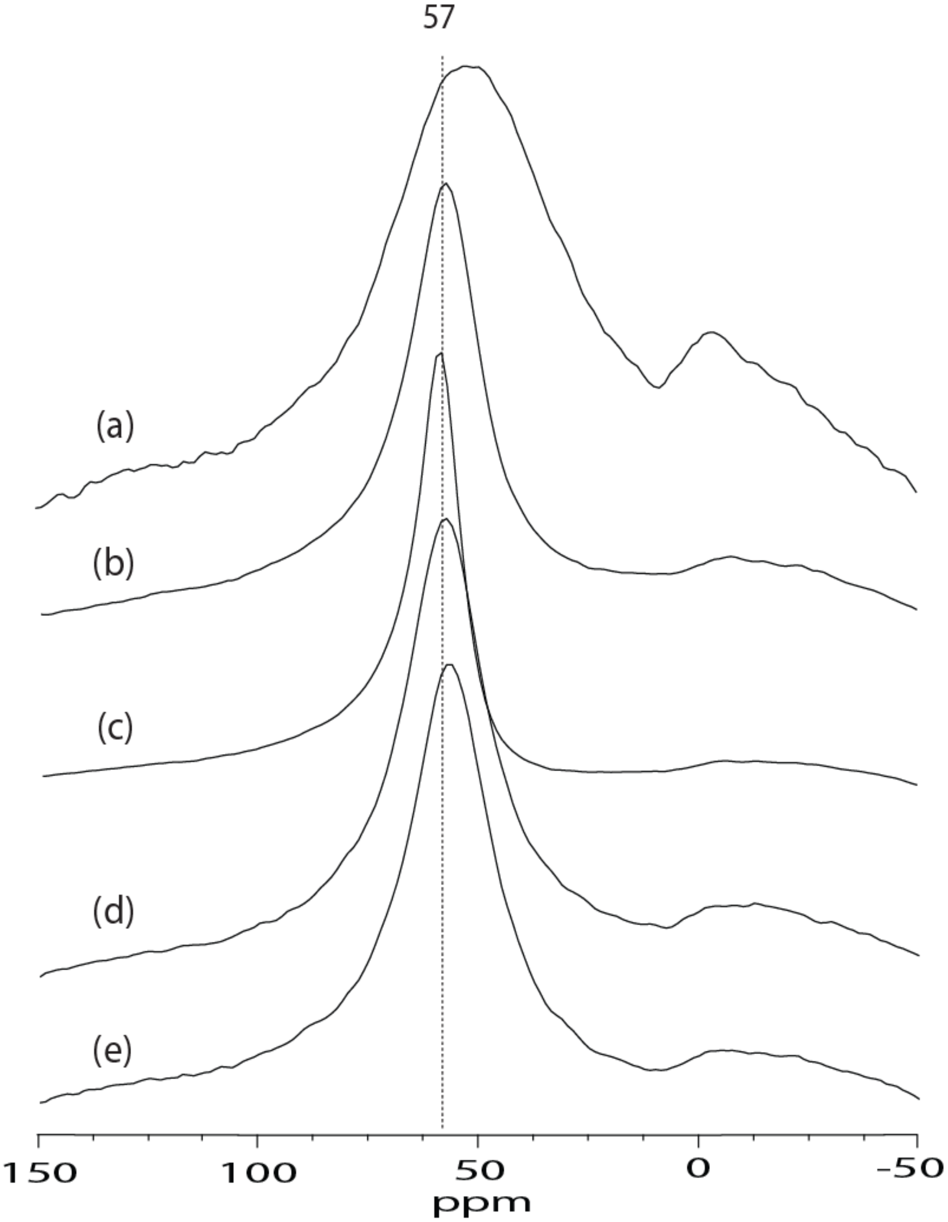

Figure 3.10: ^{27}Al MAS NMR spectra of (a) the initial fly ash; (b) fly ash activated using 8M KOH; (c) fly ash activated using 8M NaOH; (d) fly ash activated using Na-Silicate; (e) fly ash activated using K-silicate

3.4 Conclusion

Fly ash based geopolymers were synthesized using two different concentrations (4M and 8M) of NaOH and KOH, and Na and K silicates of M_s=2.0 as activators, and subjected to thermal curing. MIP and NMR were used to characterize the pore- and molecular-structure of the reaction products.

In the alkali hydroxide system, the 8M NaOH activated fly ash demonstrated the highest compressive strength, which can be attributed to highest content of aluminosilicate gel and lowest total pore volume. The highest content of aluminosilicate gel is validated by MIP (largest volume of pore with size in range of 0.0036 μm-0.05 μm) and NMR (highest amount of Q^4(mAl) gel). The K-based systems have pore volumes similar to Na-based systems, but different pore size distributions, having more volume with size>0.2μm and less volume with size in range of 0.0036 μm-0.05 μm. Also, the ^{29}Si NMR spectra of the K-based systems show a high degree of disorder. Both results explain the comparatively inferior properties of K-based system. More water molecules are constrained in the pores of the K-based systems because of more water in K^+ hydration sphere. These excess waters, as evidenced by the ^{1}H NMR spectra, interfere with the polymerization process, providing another reason for the reduced reaction product formation and compressive strength.

In the alkali silicate system, less fly ash is dissolved than in alkali hydroxide system, because of lower alkalinity, which is validated by ^{27}Al NMR spectra. The more unreacted fly ash leads to a higher degree of disorder in the final product, which can be observed in ^{29}Si NMR spectra. The soluble silicate in the activator accelerates the reaction, therefore more pore volume with sizes in the range of 0.0036 μm-0.05 μm was observed. So activated fly ash using alkali (Na/K) silicate has strength between that of 4M and 8M alkali (Na/K) silicate but a higher degree of disorder.

References

ASTM. 2012. ASTM C 618-12a, Standard specification for coal fly ash and raw or calcined natural pozzolan for use in concrete. West Conshohocken, PA.

Bakharev, T. 2005. Geopolymeric materials prepared using Class F fly ash and elevated temperature curing. *Cement and Concrete Research* 35 (6):1224-1232.

Balmer, M. L., B. C. Bunker, L. Q. Wang, C. H. F. Peden, and Y. L. Su. 1997. Solid-state Si-29 MAS NMR study of titanosilicates. *Journal of Physical Chemistry B* 101 (45):9170-9179.

Ben Haha, M, G Le Saout, F Winnefeld, and B Lothenbach. 2011. Influence of activator type on hydration kinetics, hydrate assemblage and microstructural development of alkali activated blast-furnace slags. *Cement and Concrete Research* 41 (3):301-310.

Benhelal, E., G. Zahedi, E. Shamsaei, and A. Bahadori. 2013. Global strategies and potentials to curb CO2 emissions in cement industry. *Journal of Cleaner Production* 51:142-161.

Blum, A., and A. Lasaga. 1988. ROLE OF SURFACE SPECIATION IN THE LOW-TEMPERATURE DISSOLUTION OF MINERALS. *Nature* 331 (6155):431-433.

Carbon Dioxide Emissions 2006. In *Emissions of Greenhouse Gases Report in the US*: US Department of Energy.

Dejong, Bhws, C. M. Schramm, and V. E. Parziale. 1983. POLYMERIZATION OF SILICATE AND ALUMINATE TETRAHEDRA IN GLASSES, MELTS, AND AQUEOUS-SOLUTIONS .4. ALUMINUM COORDINATION IN GLASSES AND AQUEOUS-SOLUTIONS AND COMMENTS ON THE ALUMINUM AVOIDANCE PRINCIPLE. *Geochimica Et Cosmochimica Acta* 47 (7):1223-1236.

Duxson, P, A Fernandez-Jimenez, JL Provis, GC Lukey, A Palomo, and JSJ van Deventer. 2007. Geopolymer technology: the current state of the art. *Journal of Materials Science* 42 (9):2917-2933.

Duxson, P, GC Lukey, F Separovic, and JSJ van Deventer. 2005. Effect of alkali cations on aluminum incorporation in geopolymeric gels. *Industrial & Engineering Chemistry Research* 44 (4):832-839.

Duxson, P, SW Mallicoat, GC Lukey, WM Kriven, and JSJ van Deventer. 2007. The effect of alkali and Si/Al ratio on the development of mechanical properties of metakaolin-based geopolymers. *Colloids and Surfaces a-Physicochemical and*

Engineering Aspects 292 (1):8-20.

Engelhar.G, H. Jancke, D. Hoebbel, and W. Wieker. 1974. STRUCTURAL STUDIES ON SILICATE ANIONS IN AQUEOUS-SOLUTION USING SI-29 NMR-SPECTROSCOPY. *Zeitschrift Fur Chemie* 14 (3):109-110.

Engelhardt, G., and D. Michel. 1987. *High-Resolution Solid-State NMR of Slicates and Zeolites*. Norwich: John Wiley & Sons.

Fernandez-Jimenez, A, A Palomo, and M Criado. 2005. Microstructure development of alkali-activated fly ash cement: a descriptive model. *Cement and Concrete Research* 35 (6):1204-1209.

Gomes, S., and M. Francois. 2000. Characterization of mullite in silicoaluminous fly ash by XRD, TEM, and Si-29 MAS NMR. *Cement and Concrete Research* 30 (2):175-181.

Hargreaves, David. 2013. The Global Cement Report 10th Edition.

Kato, M., and H. Nishido. 2003. Simulation of Si-29 MAS NMR spectra and modeling of aluminum ordering in the zeolites with PHI type framework. *Microporous and Mesoporous Materials* 61 (1-3):261-271.

Lee, WKW, and JSJ van Deventer. 2002. Structural reorganisation of class F fly ash in alkaline silicate solutions. *Colloids and Surfaces a-Physicochemical and Engineering Aspects* 211 (1):49-66.

LIPPMAA, E, A SAMOSON, and M MAGI. 1986. HIGH-RESOLUTION AL-27 NMR OF ALUMINOSILICATES. *Journal of the American Chemical Society* 108 (8):1730-1735.

Lippmaa, E., M. Magi, A. Samoson, G. Engelhardt, and A. R. Grimmer. 1980. STRUCTURAL STUDIES OF SILICATES BY SOLID-STATE HIGH-RESOLUTION SI-29 NMR. *Journal of the American Chemical Society* 102 (15):4889-4893.

Lizcano, M, HS Kim, S Basu, and M Radovic. 2012. Mechanical properties of sodium and potassium activated metakaolin-based geopolymers. *Journal of Materials Science* 47 (6):2607-2616.

Loewenstein, W. 1954. THE DISTRIBUTION OF ALUMINUM IN THE TETRAHEDRA OF SILICATES AND ALUMINATES. *American Mineralogist* 39 (1-2):92-96.

Mackenzie, Kenneth J.D., and Mark E. Smith. 2002. *Multinuclear Solid-State NMR of*

Inorganic Materials. Edited by R. W. Cahn, *Pefgamon Materials Series*. Oxford: Pergamon.

Madani, A., A. Aznar, J. Sanz, and J. M. Serratosa. 1990. SI-29 AND AL-27 NMR-STUDY OF ZEOLITE FORMATION FROM ALKALI-LEACHED KAOLINITES - INFLUENCE OF THERMAL PREACTIVATION. *Journal of Physical Chemistry* 94 (2):760-765.

McCormick, A. V., A. T. Bell, and C. J. Radke. 1989. EVIDENCE FROM ALKALI-METAL NMR-SPECTROSCOPY FOR ION-PAIRING IN ALKALINE SILICATE SOLUTIONS. *Journal of Physical Chemistry* 93 (5):1733-1737.

MCCORMICK, AV, and AT BELL. 1989. THE SOLUTION CHEMISTRY OF ZEOLITE PRECURSORS. *Catalysis Reviews-Science and Engineering* 31 (1-2):97-127.

Muller, D., W. Gessner, H. J. Behrens, and G. Scheler. 1981. DETERMINATION OF THE ALUMINUM COORDINATION IN ALUMINUM-OXYGEN COMPOUNDS BY SOLID-STATE HIGH-RESOLUTION AL-27 NMR. *Chemical Physics Letters* 79 (1):59-62.

Myers, R. J., S. A. Bernal, R. San Nicolas, and J. L. Provis. 2013. Generalized Structural Description of Calcium-Sodium Aluminosilicate Hydrate Gels: The Cross-Linked Substituted Tobermorite Model. *Langmuir* 29 (17):5294-5306.

Neuhoff, P. S., J. F. Stebbins, and D. K. Bird. 2003. Si-Al disorder and solid solutions in analcime, chabazite, and wairakite. *American Mineralogist* 88 (2-3):410-423.

Palomo, A, S Alonso, and A Femandez-Jimenez. 2004. Alkaline activation of fly ashes: NMR study of the reaction products. *Journal of the American Ceramic Society* 87 (6):1141-1145.

Palomo, A, MW Grutzeck, and MT Blanco. 1999. Alkali-activated fly ashes - A cement for the future. *Cement and Concrete Research* 29 (8):1323-1329.

Palomo, A., and J. I. L. de la Fuente. 2003. Alkali-activated cementitous materials: Alternative matrices for the immobilisation of hazardous wastes - Part I. Stabilisation of boron. *Cement and Concrete Research* 33 (2):281-288.

Palomo, A., and M. Palacios. 2003. Alkali-activated cementitious materials: Alternative matrices for the immobilisation of hazardous wastes - Part II. Stabilisation of chromium and lead. *Cement and Concrete Research* 33 (2):289-295.

Price, L, and D. P. Worrell. 1999. Energy use and carbon dioxide emissions in energy-intensive industries in key developing countries. In *Proceeding of the 1999 Earth Technologies Forum*. Washington, DC.

Puertas, F, S Martinez-Ramirez, S Alonso, and T Vazquez. 2000. Alkali-activated fly ash/slag cement - Strength behaviour and hydration products. *Cement and Concrete Research* 30 (10):1625-1632.

Rios, CA, CD Williams, and CL Roberts. 2009. A comparative study of two methods for the synthesis of fly ash-based sodium and potassium type zeolites. *Fuel* 88 (8):1403-1416.

ROUQUEROL, J, D AVNIR, CW FAIRBRIDGE, DH EVERETT, JH HAYNES, N PERNICONE, JDF RAMSAY, KSW SING, and KK UNGER. 1994. RECOMMENDATIONS FOR THE CHARACTERIZATION OF POROUS SOLIDS. *Pure and Applied Chemistry* 66 (8):1739-1758.

Sindhunata, JSJ van Deventer, GC Lukey, and H Xu. 2006. Effect of curing temperature and silicate concentration on fly-ash-based geopolymerization. *Industrial & Engineering Chemistry Research* 45 (10):3559-3568.

Skibsted, J., and C. Hall. 2008. Characterization of cement minerals, cements and their reaction products at the atomic and nano scale. *Cement and Concrete Research* 38 (2):205-225.

Stade, H., D. Muller, and G. Scheler. 1984. ON THE STRUCTURE OF ILL-CRYSTALLIZED CALCIUM HYDROGEN SILICATES .5. STUDIES ON THE COORDINATION OF AL IN C-S-H(DI,POLY) BY AL-27-NMR SPECTROSCOPY. *Zeitschrift Fur Anorganische Und Allgemeine Chemie* 510 (3):16-24.

Swaddle, T. W. 2001. Silicate complexes of aluminum(III) in aqueous systems. *Coordination Chemistry Reviews* 219:665-686.

Swaddle, T. W., J. Salerno, and P. A. Tregloan. 1994. AQUEOUS ALUMINATES, SILICATES, AND ALUMINOSILICATES. *Chemical Society Reviews* 23 (5):319-325.

Taylor, H. F. W. 1990. Cement Chemistry. London: Academic Press.

van Jaarsveld, JGS, and JSJ van Deventer. 1999. Effect of the alkali metal activator on the properties of fly ash-based geopolymers. *Industrial & Engineering Chemistry Research* 38 (10):3932-3941.

Walther, J. V. 1996. Relation between rates of aluminosilicate mineral dissolution, pH, temperature, and surface charge. *American Journal of Science* 296 (7):693-728.

Washburn, E. W. 1921. The dynamics of capillary flow. *Physical Review* 17 (3):273-283.

Xu, H., and J. S. J. van Deventer. 2003. The effect of alkali metals on the formation of geopolymeric gels from alkali-feldspars. *Colloids and Surfaces a-Physicochemical and Engineering Aspects* 216 (1-3):27-44.

CHAPTER 4

SUMMARY&FUTURE WORK

One kind of new material Gd(DTPA)-intercalated LDH nanoparticles in water suspension has been successfully synthesized. This new material can have higher relaxivity than Gd(DTPA) in solution, which is a commercial contrast agent in wide use. The relaxivity of Gd(DTPA)-intercalated LDH depends on the crystallinity of the NPs, their particle size, intercalation percentage etc. A series of experiments were conducted to find samples with as high relaxivity as possible and to investigate the mechanism of relaxivity in the NPs. The results show that the material's relaxivity is not sensitive to particle size when the particles have a large diameters (500nm-800nm), because the NP's rotational correlation time contribution is too long to affect the total NMR correlation time for proton spin relaxation. But samples with lower crystallinity and lower intercalation percentage have higher relaxivity, because this situation is favorable to water exchange. Thus, the enhancement of relaxivity is partially attributed to long rotational correlation times of NPs but restricted by the long exchange correlation times of water molecules.

Particles with smaller size (200nm-500nm) will be examined. In that range, rotational correlation time may have distinct effects on relaxivity and therefore help towards understanding the relaxivity mechanism of LDH NPs, also in developing materials with higher relaxivity. In addition, relaxivity could be enhanced by intercalation of other Gd chelates with faster inner water exchange, like Gd(EGTA).

In the work on cementitious materials, the properties of alkali activated fly ash were studied, including pore structure and NMR spectra. The results show that higher alkalinity of the same type of activator leads to higher dissolution of the starting fly ash material and to more aluminosilicate gel formation, therefore higher strength of the final product. The Na activator has higher efficiency than the K activator. With extra soluble silicate added in the activator (Na/K silicate) less fly ash was dissolved but the soluble silicate could accelerate the formation of aluminosilicate gel, leading to relatively high strength (for example the sample using 4M alkali hydroxide) of the final product.

More NMR studies will be conducted on alkali activated fly ash, slag and the mixtures of these two starting materials, to investigate the process of alkali activated reaction and the compositions of final products, therefore helping optimizing the development of alkali activated cementitious materials to replace ordinary Portland cement.

REFERENCES

Abragam, A. 1961. *Principles of Nuclear Magnetism*. Oxford: Clarendon Press.

Aime, S., M. Botta, S. G. Crich, G. B. Giovenzana, R. Pagliarin, M. Piccinini, M. Sisti, and E. Terreno. 1997. Towards MRI contrast agents of improved efficacy. NMR relaxometric investigations of the binding interaction to HSA of a novel heptadentate macrocyclic triphosphonate Gd(III)-complex. *Journal of Biological Inorganic Chemistry* 2 (4):470-479.

Aime, S., P. Ascenzi, E. Comoglio, M. Fasano, and S. Paoletti. 1995. MOLECULAR RECOGNITION OF R-STATES AND T-STATES OF HUMAN ADULT HEMOGLOBIN BY A PARAMAGNETIC GD(III) COMPLEX BY MEANS OF THE MEASUREMENT OF SOLVENT WATER PROTON RELAXATION RATE. *Journal of the American Chemical Society* 117 (36):9365-9366.

Andrew, E. R. 1981. MAGIC ANGLE SPINNING IN SOLID-STATE NMR-SPECTROSCOPY. *Philosophical Transactions of the Royal Society a-Mathematical Physical and Engineering Sciences* 299 (1452):505-520.

Andrew, ER. 1971. The narrowing of NMR spectra of solids by high-speed specimen rotation and the resolution of chemical shift and spin multiplet structures for solids. *Progress in Nuclear Magnetic Resonance Spectroscopy* 8 (1):1-39.

ASTM. 2012. ASTM C 618-12a, *Standard specification for coal fly ash and raw or calcined natural pozzolan for use in concret*. West Conshohocken, PA.

Bakharev, T. 2005. Geopolymeric materials prepared using Class F fly ash and elevated temperature curing. *Cement and Concrete Research* 35 (6):1224-1232.

Balmer, M. L., B. C. Bunker, L. Q. Wang, C. H. F. Peden, and Y. L. Su. 1997. Solid-state Si-29 MAS NMR study of titanosilicates. *Journal of Physical Chemistry B* 101 (45):9170-9179.

Ben Haha, M, G Le Saout, F Winnefeld, and B Lothenbach. 2011. Influence of activator type on hydration kinetics, hydrate assemblage and microstructural development of alkali activated blast-furnace slags. *Cement and Concrete Research* 41 (3):301-310.

Benhelal, E., G. Zahedi, E. Shamsaei, and A. Bahadori. 2013. Global strategies and potentials to curb CO2 emissions in cement industry. *Journal of Cleaner Production* 51:142-161.

BLOCH, F, WW HANSEN, and M PACKARD. 1946. THE NUCLEAR INDUCTION EXPERIMENT. *Physical Review* 70 (7-8):474-485.

BLOCH, F. 1946. NUCLEAR INDUCTION. *Physical Review* 70 (7-8):460-474.

Bloch, F. 1956. DYNAMICAL THEORY OF NUCLEAR INDUCTION .2. *Physical Review* 102 (1):104-135.

Bloembergen, N., and L. O. Morgan. 1961. PROTON RELAXATION TIMES IN PARAMAGNETIC SOLUTIONS EFFECTS OF ELECTRON SPIN RELAXATION. *Journal of Chemical Physics* 34 (3):842-&.

Blum, A., and A. Lasaga. 1988. ROLE OF SURFACE SPECIATION IN THE LOW-TEMPERATURE DISSOLUTION OF MINERALS. *Nature* 331 (6155):431-433.

Botta, M. 2000. Second coordination sphere water molecules and relaxivity of gadolinium(III) complexes: Implications for MRI contrast agents. *European Journal of Inorganic Chemistry* (3):399-407.

Bottrill, Melanie, Lilian Kwok Nicholas, and Nicholas J. Long. 2006. Lanthanides in magnetic resonance imaging. *Chemical Society Reviews* 35 (6):557-571.

Brateman, P. S., Z. P. Xu, and F. Yarberry. 2004. *Handbook of Layered Materials*. Edited by S. M. Auerbach, K. A. Carrado and P. K. Dutta. New York: Marcel Dekker Inc.

Bydder, G. M., R. E. Steiner, D. J. Thomas, J. Marshall, D. J. Gilderdale, and I. R. Young. 1983. NUCLEAR MAGNETIC-RESONANCE IMAGING OF THE POSTERIOR-FOSSA - 50 CASES. *Clinical Radiology* 34 (2):173-188.

Caravan, P. 2006. Strategies for increasing the sensitivity of gadolinium based MRI contrast agents. *Chemical Society Reviews* 35 (6):512-523.

Caravan, P., J. J. Ellison, T. J. McMurry, and R. B. Lauffer. 1999. Gadolinium(III) chelates as MRI contrast agents: Structure, dynamics, and applications. *Chemical Reviews* 99 (9):2293-2352.

Caravan, P., M. T. Greenfield, X. D. Li, and A. D. Sherry. 2001. The Gd3+ complex of a fatty acid analogue of DOTP binds to multiple albumin sites with variable water relaxivities. *Inorganic Chemistry* 40 (26):6580-6587.

Carbon Dioxide Emissions 2006. *In Emissions of Greenhouse Gases Report in the US*: US Department of Energy.

Cavani, F., F. Trifiro, and A. Vaccari. 1991. HYDROTALCITE-TYPE ANIONIC CLAYS: PREPARATION, PROPERTIES AND APPLICATIONS. *Catalysis Today* 11 (2):173-301.

Carr, D. H., J. Brown, G. M. Bydder, H. J. Weinmann, U. Speck, D. J. Thomas, and I. R. Young. 1984. INTRAVENOUS CHELATED GADOLINIUM AS A CONTRAST AGENT IN NMR IMAGING OF CEREBRAL-TUMORS. *Lancet* 1 (8375):484-486

Damadian, R. 1971. TUMOR DETECTION BY NUCLEAR MAGNETIC RESONANCE. *Science* 171 (3976):1151-&.

Dejong, Bhws, C. M. Schramm, and V. E. Parziale. 1983. POLYMERIZATION OF SILICATE AND ALUMINATE TETRAHEDRA IN GLASSES, MELTS, AND AQUEOUS-SOLUTIONS .4. ALUMINUM COORDINATION IN GLASSES AND AQUEOUS-SOLUTIONS AND COMMENTS ON THE ALUMINUM AVOIDANCE PRINCIPLE. *Geochimica Et Cosmochimica Acta* 47 (7):1223-1236.

Duxson, P, A Fernandez-Jimenez, JL Provis, GC Lukey, A Palomo, and JSJ van Deventer. 2007. Geopolymer technology: the current state of the art. *Journal of Materials Science* 42 (9):2917-2933.

Dupuis, J., J. P. Battut, Z. Fawal, H. Hajjimohamad, A. Deroy, and J. P. Besse. 1990. NUCLEAR-MAGNETIC-RESONANCE ANALYSIS OF PROTONS IN THE HYDROTALCITE TYPE COMPOUND ZN2/3AL1/3(OH)2CL1/3.N(H2O). *Solid State Ionics* 42 (3-4):251-255.

Duxson, P, GC Lukey, F Separovic, and JSJ van Deventer. 2005. Effect of alkali cations on aluminum incorporation in geopolymeric gels. Industrial & Engineering *Chemistry Research* 44 (4):832-839.

Duxson, P, SW Mallicoat, GC Lukey, WM Kriven, and JSJ van Deventer. 2007. The effect of alkali and Si/Al ratio on the development of mechanical properties of metakaolin-based geopolymers. *Colloids and Surfaces a-Physicochemical and Engineering Aspects* 292 (1):8-20.

Engelhar.G, H. Jancke, D. Hoebbel, and W. Wieker. 1974. STRUCTURAL STUDIES ON SILICATE ANIONS IN AQUEOUS-SOLUTION USING SI-29 NMR-SPECTROSCOPY. *Zeitschrift Fur Chemie* 14 (3):109-110.

Engelhardt, G., and D. Michel. 1987. *High-Resolution Solid-State NMR of Slicates and Zeolites*. Norwich: John Wiley & Sons.

Ersoy, H., and F. J. Rybicki. 2007. Biochemical safety profiles of gadolinium-based extracellular contrast agents and nephrogenic systemic fibrosis. *Journal of Magnetic Resonance Imaging* 26 (5):1190-1197.

Farrar, Thomas. 1990. Density Matrices in NMR Spectroscopy: Part I. *Concepts in Magnetic Resonance* 2 (1):1-12.

Farra, Thomas. 1990. Density Matrices in NMR Spectroscopy: Part II. *Concepts in Magnetic Resonance* 2 (2):55-61.

Fernandez-Jimenez, A, A Palomo, and M Criado. 2005. Microstructure development of alkali-activated fly ash cement: a descriptive model. *Cement and Concrete Research* 35 (6):1204-1209.

FREED, JH. 1978. DYNAMIC EFFECTS OF PAIR CORRELATION-FUNCTIONS ON SPIN RELAXATION BY TRANSLATIONAL DIFFUSION IN LIQUIDS .2. FINITE JUMPS AND INDEPENDENT T1 PROCESSES. *Journal of Chemical Physics* 68 (9):4034-4037.

Goldman, Maurice. 1990. *Quantum Description of High-Resolution NMR in Liquids*. Oxford: Oxford University Press.

Gomes, S., and M. Francois. 2000. Characterization of mullite in silicoaluminous fly ash by XRD, TEM, and Si-29 MAS NMR. *Cement and Concrete Research* 30 (2):175-181.

Gore, J. C. 1985. PHYSICAL FACTORS IN THE DESIGN OF CONTRAST AGENTS FOR MRI. *Ieee Engineering in Medicine and Biology Magazine* 4 (3):39-42.

Hahn, E. L. 1950. SPIN ECHOES. *Physical Review* 77 (5):746-746.

Hargreaves, David. 2013. *The Global Cement Report 10th Edition*.

Hartmann, S. R., and E. L. Hahn. 1962. NUCLEAR DOUBLE RESONANCE IN ROTATING FRAME. *Physical Review* 128 (5):2042-&.

Hinshaw, W. S., P. A. Bottomley, and G. N. Holland. 1977. RADIOGRAPHIC THIN-SECTION IMAGE OF HUMAN WRIST BY NUCLEAR MAGNETIC-RESONANCE. *Nature* 270 (5639):722-723.

HWANG, LP, and JH FREED. 1975. DYNAMIC EFFECTS OF PAIR CORRELATION-FUNCTIONS ON SPIN RELAXATION BY TRANSLATIONAL DIFFUSION IN LIQUIDS. *Journal of Chemical Physics* 63 (9):4017-4025.

Kato, M., and H. Nishido. 2003. Simulation of Si-29 MAS NMR spectra and modeling of aluminum ordering in the zeolites with PHI type framework. *Microporous and Mesoporous Materials* 61 (1-3):261-271.

Kwak, S. Y., Y. J. Jeong, J. S. Park, and J. H. Choy. 2002. Bio-LDH nanohybrid for gene therapy. *Solid State Ionics* 151 (1-4):229-234.

Lauffer, R. B. 1987. PARAMAGNETIC METAL-COMPLEXES AS WATER PROTON RELAXATION AGENTS FOR NMR IMAGING - THEORY AND DESIGN. *Chemical Reviews* 87 (5):901-927.

Lauterbur, P. C. 1973. IMAGE FORMATION BY INDUCED LOCAL INTERACTIONS - EXAMPLES EMPLOYING NUCLEAR MAGNETIC-RESONANCE. *Nature* 242 (5394):190-191.

Lauterbur, P. C. 1973. IMAGE FORMATION BY INDUCED LOCAL INTERACTIONS - EXAMPLES EMPLOYING NUCLEAR MAGNETIC-RESONANCE. *Nature* 242 (5394):190-191.

Lauterbur, P. C. 1974. MAGNETIC-RESONANCE ZEUGMATOGRAPHY. *Pure and Applied Chemistry* 40 (1-2):149-157.

Lee, J. H., Y. M. Huh, Y. Jun, J. Seo, J. Jang, H. T. Song, S. Kim, E. J. Cho, H. G. Yoon, J. S. Suh, and J. Cheon. 2007. Artificially engineered magnetic nanoparticles for ultra-sensitive molecular imaging. *Nature Medicine* 13 (1):95-99.

Lee, WKW, and JSJ van Deventer. 2002. Structural reorganisation of class F fly ash in alkaline silicate solutions. *Colloids and Surfaces a-Physicochemical and Engineering Aspects* 211 (1):49-66.

Li, A., L. L. Qin, W. R. Wang, R. R. Zhu, Y. C. Yu, H. Liu, and S. L. Wang. 2011. The use of layered double hydroxides as DNA vaccine delivery vector for enhancement of anti-melanoma immune response. *Biomaterials* 32 (2):469-477.

Liang, Zhi-Pei, and Paul C. Lauterbur. 2000. *Principles of Magnetic Resonance Imaging*. New York: IEEE Press.

LIPPMAA, E, A SAMOSON, and M MAGI. 1986. HIGH-RESOLUTION AL-27 NMR OF ALUMINOSILICATES. *Journal of the American Chemical Society* 108 (8):1730-1735.

Lippmaa, E., M. Magi, A. Samoson, G. Engelhardt, and A. R. Grimmer. 1980. STRUCTURAL STUDIES OF SILICATES BY SOLID-STATE HIGH-RESOLUTION SI-29 NMR. *Journal of the American Chemical Society* 102 (15):4889-4893.

Lizcano, M, HS Kim, S Basu, and M Radovic. 2012. Mechanical properties of sodium and potassium activated metakaolin-based geopolymers. *Journal of Materials Science* 47 (6):2607-2616.

Loewenstein, W. 1954. THE DISTRIBUTION OF ALUMINUM IN THE TETRAHEDRA OF SILICATES AND ALUMINATES. *American Mineralogist* 39 (1-2):92-96.

Lyerla, J. R., H. M. McIntyre, and D. A. Torchia. 1974. C-13 NUCLEAR MAGNETIC-RESONANCE STUDY OF ALKANE MOTION. *Macromolecules* 7 (1):11-14.

Maciel, G. E. 1984. HIGH-RESOLUTION NUCLEAR MAGNETIC-RESONANCE OF SOLIDS. *Science* 226 (4672):282-288.

Mackenzie, Kenneth J.D., and Mark E. Smith. 2002. *Multinuclear Solid-State NMR of Inorganic Materials*. Edited by R. W. Cahn, Pefgamon Materials Series. Oxford: Pergamon.

Madani, A., A. Aznar, J. Sanz, and J. M. Serratosa. 1990. SI-29 AND AL-27 NMR-STUDY OF ZEOLITE FORMATION FROM ALKALI-LEACHED KAOLINITES - INFLUENCE OF THERMAL PREACTIVATION. *Journal of Physical Chemistry* 94 (2):760-765.

Mansfield, P. 1977. MULTI-PLANAR IMAGE-FORMATION USING NMR SPIN ECHOES. *Journal of Physics C-Solid State Physics* 10 (3):L55-L58.

Mansfield, P., and I. L. Pykett. 1978. BIOLOGICAL AND MEDICAL IMAGING BY NMR. *Journal of Magnetic Resonance* 29 (2):355-373.

Maricq, M. M., and J. S. Waugh. 1979. NMR IN ROTATING SOLIDS. *Journal of Chemical Physics* 70 (7):3300-3316.

McCormick, A. V., A. T. Bell, and C. J. Radke. 1989. EVIDENCE FROM ALKALI-METAL NMR-SPECTROSCOPY FOR ION-PAIRING IN ALKALINE SILICATE SOLUTIONS. *Journal of Physical Chemistry* 93 (5):1733-1737.

MCCORMICK, AV, and AT BELL. 1989. THE SOLUTION CHEMISTRY OF ZEOLITE PRECURSORS. *Catalysis Reviews-Science and Engineering* 31 (1-2):97-127.

Micskei, K., L. Helm, E. Brucher, and A. E. Merbach. 1993. O-17 NMR-STUDY OF WATER EXCHANGE ON GD(DTPA)(H2O) 2- AND GD(DOTA)(H2O) - RELATED TO NMR IMAGING. *Inorganic Chemistry* 32 (18):3844-3850.

Morgan, Christopher J., and William R. Hendee. 1984. *Introduction to Magnetic Resonance Imaging*. Missouri: Multi-Media Publishing Inc.

Muller, D., W. Gessner, H. J. Behrens, and G. Scheler. 1981. DETERMINATION OF THE ALUMINUM COORDINATION IN ALUMINUM-OXYGEN COMPOUNDS BY SOLID-STATE HIGH-RESOLUTION AL-27 NMR. *Chemical Physics Letters* 79 (1):59-62.

Myers, R. J., S. A. Bernal, R. San Nicolas, and J. L. Provis. 2013. Generalized Structural Description of Calcium-Sodium Aluminosilicate Hydrate Gels: The Cross-Linked Substituted Tobermorite Model. *Langmuir* 29 (17):5294-5306.

Nakamura, H., N. Ito, F. Kotake, Y. Mizokami, and T. Matsuoka. 2000. Tumor-detecting capacity and clinical usefulness of SPIO-MRI in patients with hepatocellular carcinoma. *Journal of Gastroenterology* 35 (11):849-855.

Neuhoff, P. S., J. F. Stebbins, and D. K. Bird. 2003. Si-Al disorder and solid solutions in analcime, chabazite, and wairakite. *American Mineralogist* 88 (2-3):410-423.

Oh, Jae-Min, Timothy T. Biswick, and Jin-Ho Choy. 2009. Layered nanomaterials for green materials. *Journal of Materials Chemistry* 19 (17):2553-2563.

Oksendal, A. N., and P. A. Hals. 1993. BIODISTRIBUTION AND TOXICITY OF MR IMAGING CONTRAST-MEDIA. *Journal of Magnetic Resonance Imaging* 3 (1):157-165.

Oldfield, E., and R. J. Kirkpatrick. 1985. HIGH-RESOLUTION NUCLEAR MAGNETIC-RESONANCE OF INORGANIC SOLIDS. *Science* 227 (4694):1537-1544.

Pake, G. E. 1950. FUNDAMENTALS OF NUCLEAR MAGNETIC RESONANCE ABSORPTION .1. *American Journal of Physics* 18 (7):438-452.

Pake, G. E. 1950. FUNDAMENTALS OF NUCLEAR MAGNETIC RESONANCE ABSORPTION .2. *American Journal of Physics* 18 (8):473-486.

Palomo, A, MW Grutzeck, and MT Blanco. 1999. Alkali-activated fly ashes - A cement for the future. *Cement and Concrete Research* 29 (8):1323-1329.

Palomo, A, S Alonso, and A Femandez-Jimenez. 2004. Alkaline activation of fly ashes: NMR study of the reaction products. *Journal of the American Ceramic Society* 87 (6):1141-1145.

Palomo, A., and J. I. L. de la Fuente. 2003. Alkali-activated cementitous materials: Alternative matrices for the immobilisation of hazardous wastes - Part I. Stabilisation of boron. *Cement and Concrete Research* 33 (2):281-288.

Palomo, A., and M. Palacios. 2003. Alkali-activated cementitious materials: Alternative matrices for the immobilisation of hazardous wastes - Part II. Stabilisation of chromium and lead. *Cement and Concrete Research* 33 (2):289-295.

Pines, A., M. G. Gibby, and J. S. Waugh. 1973. PROTON-ENHANCED NMR OF DILUTE SPINS IN SOLIDS. *Journal of Chemical Physics* 59 (2):569-590.

Powell, D. H., O. M. NiDhubhghaill, D. Pubanz, L. Helm, Y. S. Lebedev, W. Schlaepfer, and A. E. Merbach. 1996. Structural and dynamic parameters obtained from O-17 NMR, EPR, and NMRD studies of monomeric and dimeric Gd3+ complexes of interest in magnetic resonance imaging: An integrated and theoretically self consistent approach. *Journal of the American Chemical Society* 118 (39):9333-9346.

Price, L, and D. P. Worrell. 1999. Energy use and carbon dioxide emissions in energy-intensive industries in key developing countries. *In Proceeding of the 1999 Earth Technologies Forum*. Washington, DC.

Puertas, F, S Martinez-Ramirez, S Alonso, and T Vazquez. 2000. Alkali-activated fly ash/slag cement - Strength behaviour and hydration products. *Cement and Concrete Research* 30 (10):1625-1632.

PURCELL, EM, HC TORREY, and RV POUND. 1946. RESONANCE ABSORPTION BY NUCLEAR MAGNETIC MOMENTS IN A SOLID. *Physical Review* 69 (1-2):37-38.

Qin, L. L., M. Xue, W. R. Wang, R. R. Zhu, S. L. Wang, J. Sun, R. Zhang, and X. Y. Sun. 2010. The in vitro and in vivo anti-tumor effect of layered double hydroxides nanoparticles as delivery for podophyllotoxin. *International Journal of Pharmaceutics* 388 (1-2):223-230.

Rabi, II, JR Zacharias, S Millman, and P Kusch. 1938. A new method of measuring nuclear magnetic moment. *Physical Review* 53 (4):318-318.

Redfield, A. G. 1957. ON THE THEORY OF RELAXATION PROCESSES. Ibm *Journal of Research and Development* 1 (1):19-31.

Rios, CA, CD Williams, and CL Roberts. 2009. A comparative study of two methods for the synthesis of fly ash-based sodium and potassium type zeolites. *Fuel* 88 (8):1403-1416.

Rives, V., and M. A. Ulibarri. 1999. Layered double hydroxides (LDH) intercalated with metal coordination compounds and oxometalates. *Coordination Chemistry Reviews* 181:61-120.

ROUQUEROL, J, D AVNIR, CW FAIRBRIDGE, DH EVERETT, JH HAYNES, N PERNICONE, JDF RAMSAY, KSW SING, and KK UNGER. 1994. RECOMMENDATIONS FOR THE CHARACTERIZATION OF POROUS SOLIDS. *Pure and Applied Chemistry* 66 (8):1739-1758.

Sijbers, J., P. Scheunders, N. Bonnet, D. VanDyck, and E. Raman. 1996. Quantification and improvement of the signal-to-noise ratio in a magnetic resonance image acquisition procedure. *Magnetic Resonance Imaging* 14 (10):1157-1163.

Silion, M., D. Hritcu, I. M. Jaba, B. Tamba, D. Ionescu, O. C. Mungiu, and I. M. Popa. 2010. In vitro and in vivo behavior of ketoprofen intercalated into layered double hydroxides. *Journal of Materials Science-Materials in Medicine* 21 (11):3009-3018.

Sindhunata, JSJ van Deventer, GC Lukey, and H Xu. 2006. Effect of curing temperature and silicate concentration on fly-ash-based geopolymerization. *Industrial & Engineering Chemistry Research* 45 (10):3559-3568.

Skibsted, J., and C. Hall. 2008. Characterization of cement minerals, cements and their reaction products at the atomic and nano scale. *Cement and Concrete Research* 38 (2):205-225.

Slichter, C. P. 1989. *Principles of Magnetic Resonance*. 3rd Ed ed. Berlin: Springer-Verlag.

Solomon, I. 1955. RELAXATION PROCESSES IN A SYSTEM OF 2 SPINS. *Physical Review* 99 (2):559-565.

Stade, H., D. Muller, and G. Scheler. 1984. ON THE STRUCTURE OF ILL-CRYSTALLIZED CALCIUM HYDROGEN SILICATES .5. STUDIES ON THE COORDINATION OF AL IN C-S-H(DI,POLY) BY AL-27-NMR SPECTROSCOPY. *Zeitschrift Fur Anorganische Und Allgemeine Chemie* 510 (3):16-24.

Stejskal, E. O., and J. D. Memory. 1994. *High Resolution NMR in the Solid State*. Oxford: Oxford University Press.

Swaddle, T. W. 2001. Silicate complexes of aluminum(III) in aqueous systems. *Coordination Chemistry Reviews* 219:665-686.

Swaddle, T. W., J. Salerno, and P. A. Tregloan. 1994. AQUEOUS ALUMINATES, SILICATES, AND ALUMINOSILICATES. *Chemical Society Reviews* 23 (5):319-325.

Swift, T. J., and R. E. Connick. 1962. NMR-RELAXATION MECHANISMS OF 017 IN AQUEOUS SOLUTIONS OF PARAMAGNETIC CATIONS AND LIFETIME OF WATER MOLECULES IN FIRST COORDINATION SPHERE. *Journal of Chemical Physics* 37 (2):307-&.

Taylor, H. F. W. 1990. *Cement Chemistry*. London: Academic Press.

TC, Farrar. 1987. *An introduction to pulse NMR spectroscopy*. Madison: The Farragut Press.

van Jaarsveld, JGS, and JSJ van Deventer. 1999. Effect of the alkali metal activator on the properties of fly ash-based geopolymers. *Industrial & Engineering Chemistry Research* 38 (10):3932-3941.

Walther, J. V. 1996. Relation between rates of aluminosilicate mineral dissolution, pH, temperature, and surface charge. *American Journal of Science* 296 (7):693-728.

Wangsness, R. K., and F. Bloch. 1953. THE DYNAMICAL THEORY OF NUCLEAR INDUCTION. *Physical Review* 89 (4):728-739.

Washburn, E. W. 1921. The dynamics of capillary flow. *Physical Review* 17 (3):273-283.

Xu, H., and J. S. J. van Deventer. 2003. The effect of alkali metals on the formation of geopolymeric gels from alkali-feldspars. *Colloids and Surfaces a-Physicochemical and Engineering Aspects* 216 (1-3):27-44.